

# POLITECNICO DI TORINO

Master of Science in Energy and Nuclear Engineering  
Poly<sup>2</sup>Nuc Programme



MSc Thesis

## Numerical Investigation of Vapor Shielding in Linear Plasma Devices

**Supervisors:**

Prof. F. Subba  
Prof. M. Passoni  
Ph.D. G. F. Nallo  
Ing. E. Tonello

**Candidate:**

Enrico Emanuelli

Academic Year 2020/2021



## Abstract

Nuclear fusion technologies are one of the most investigated lines of research to try to tackle the problem of finding a reliable, sustainable and environmental-friendly energy source. Notwithstanding all the efforts that have been put into it, there are still several issues that hinder its development: one of them is the interaction between the plasma and the plasma-facing components, because of the high energy and particle flux that the target surfaces are requested to bear. The currently adopted divertor technologies are still far from being able to withstand the fluxes that a future plant could supply and it is thus needed a design revolution. A breakthrough in this respect could consist in the use of divertors coated by liquid metals (LMs) instead of the bare solid ones: they exhibit a self-healing nature and they are able to produce a vapour cloud in front of the target, which is able to dissipate a relevant fraction of the energy before it can reach the surface. Experiments performed exploiting linear plasma devices (LPDs) showed that the physical parameters of the vapour cloud have an oscillating dynamical behaviour, which is induced by a detachment-like phenomenon of the plasma and by the difference of timescales between thermal equilibria of the LM and the atomic physics. This thesis aims at finding a suitable zero-dimensional model to study the interaction between the plasma and the liquid metal in LPDs. The use of such a simplified model can be justified by the fact that it can be fast-running (since it focuses on the time dependence of the relevant phenomena) and that it is able to include terms that would be otherwise neglected in much more complex codes, possibly allowing additional interpretations of the phenomena at play. Taking as a starting point a 0D model that referred only to the main plasma species and to the whole volume of a LPD, it was advanced in order to include the LM populations. The studies performed with such a model showed that employing input parameters resembling more physical situations (in which the average LM density over the whole device is small if compared to the main plasma), the model is appropriate but it is not able to show a significant plasma-LM interaction. It is instead possible to do so by increasing the LM concentration, in order to simulate the vapour cloud situation in which the main plasma and LM densities are comparable: in this case an important synergy between the two species has been noticed, but it was not possible to study the phenomena in a self-consistent way. To solve both these issues it will be needed in the future to develop a 0D model whose domain is readjusted to the volume of the vapor cloud in front of the divertor: the set of equations that could give birth to such a model are discussed at the end of this work.



# Acknowledgements

As a suitable conclusion of this thesis work I would like to express my gratitude to my supervisors Prof. Fabio Subba and Prof. Matteo Passoni: not only you made this collaboration possible, but you contributed to the growth of my passion for the topic of PMI and plasma physics in general.

A big thank you also to Ph.D student Elena Tonello, who readily made available the code she developed at Politecnico di Milano in order for me to be able to work on it. Thanks again for your availability when I had some perplexities: they lasted just for the time necessary for me to realize that I should have asked you.

Last but definitely not least, my utmost appreciations go to Ph.D Giuseppe Francesco Nallo: your passion and your kindness have been clear to me since the first time I attended one of your lectures when you started being a teaching assistant in “Termofluidodinamica”. You always try your best to help students and you did the same for me as well, which is something that I do not take for granted. Thank you for being a source of inspiration not only as a researcher, but also as a kind and empathic human being.

# Table of Contents

<b>Acronyms</b>	VII
<b>1 Introduction</b>	1
1.1 A global challenge . . . . .	1
1.1.1 The dependence on fossil fuels . . . . .	1
1.1.2 Nuclear power plants . . . . .	3
1.1.3 The role of nuclear fusion . . . . .	5
1.2 Nuclear reactions for energy production . . . . .	6
1.2.1 Nuclear energy fundamentals . . . . .	6
1.2.2 The most desirable fusion reactions . . . . .	7
1.3 The plasma state and its connection with nuclear fusion . . . . .	9
1.3.1 What is a plasma? . . . . .	9
1.3.2 The Debye length . . . . .	10
1.3.3 Laboratory production . . . . .	11
1.3.4 Plasmas in nature . . . . .	12
1.3.5 Connection with nuclear fusion . . . . .	13
1.4 How to attain fusion on Earth . . . . .	13
1.4.1 The Lawson criterion . . . . .	13
1.4.2 Two possibilities to produce nuclear fusion energy . . . . .	16
1.4.3 Tritium production and energy extraction . . . . .	16
1.5 Magnetic confinement fusion . . . . .	17
1.5.1 Basic principles of magnetic confinement . . . . .	17
1.5.2 Leading MCF approaches . . . . .	19
1.5.3 Tokamak progress and future objectives . . . . .	20
<b>2 Plasma-surface interaction and divertor technology</b>	23
2.1 Physics of plasma-surface interaction . . . . .	23
2.1.1 The Debye Sheath . . . . .	24
2.1.2 Physical sputtering . . . . .	27
2.1.3 Thermal and chemical sputtering . . . . .	30
2.1.4 Retention, recycling and re-deposition . . . . .	32

2.1.5	Atomic processes	34
2.2	The plasma-material interaction challenge	37
2.2.1	The power exhaust challenge	38
2.2.2	Engineering solutions	39
2.3	The divertor technology	40
2.3.1	Divertor physics	40
2.3.2	Cross-field diffusion in the SOL	42
2.3.3	Future divertor solutions	43
2.3.4	Importance of linear plasma devices	44
2.4	Liquid metal divertors	45
2.4.1	Solid vs LM divertors	46
2.4.2	Vapour shielding	47
2.4.3	Main LM possibilities	52
2.4.4	Main LMD concepts	55
2.4.5	LM perspectives	58
<b>3</b>	<b>Development of a 0D model including the LM</b>	<b>61</b>
3.1	Thesis' motivations and goals	61
3.1.1	The importance of models	61
3.1.2	Aim of the thesis	63
3.2	Available model description	64
3.2.1	General context	64
3.2.2	Principles of the point plasma model for LPDs	65
3.2.3	Summary of the results of the model	68
3.3	Model advancement	69
3.3.1	Choice of the LM	69
3.3.2	Addition of the LM populations	70
3.3.3	Initial conditions and model switches	72
3.3.4	Limitations and expectations	73
<b>4</b>	<b>Overview of the results</b>	<b>75</b>
4.1	Benchmark against original model	76
4.2	Lithium "switching on"	77
4.2.1	Transient evaluation	77
4.2.2	Electron heat losses mechanisms	79
4.2.3	Sensitivity analysis	80
4.3	Increase of Li source	83
4.3.1	Motivations	83
4.3.2	Choice of the input parameters	83
4.3.3	Transient study	84
4.3.4	Re-evaluation of the electron heat losses	87

<b>5</b>	<b>Future development of the model</b>	89
5.1	Domain modification . . . . .	89
5.2	Adjustments of flux terms . . . . .	91
5.2.1	Changes on the number of sources and sinks . . . . .	91
5.2.2	Parallel transport . . . . .	92
5.2.3	Cross-field diffusion . . . . .	93
5.2.4	Source terms . . . . .	93
5.2.5	Electron energy balance equation . . . . .	94
5.3	Additional equations . . . . .	96
5.3.1	Energy equations . . . . .	96
5.3.2	Target surface temperature equation . . . . .	98
5.4	Main issues and potentialities . . . . .	98
<b>6</b>	<b>Conclusions and perspectives</b>	101
	<b>List of Figures</b>	103
	<b>List of Tables</b>	107
	<b>Bibliography</b>	109

# Acronyms

**CPS** Capillary Porous Structure

**CX** Charge eXchange

**ELM** Edge-Localised Mode

**FW** First Wall

**ICF** Inertial Confinement Fusion

**LCFS** Last Closed magnetic Flux Surface

**LMD** Liquid Metal Divertor

**LPD** Linear Plasma Device

**MCF** Magnetic Confinement Fusion

**ODE** Ordinary Differential Equation

**PFC** Plasma-Facing Component

**PKA** Primary Knocked-on Atom

**PMI** Plasma-Material Interaction

**SOL** Scrape-Off Layer

**TBM** Tritium Blanket Modules

**TBR** Tritium Breeding Ratio

# Chapter 1

## Introduction

This introductory chapter presents the global and physical framework in which nuclear fusion research is under development. In *Section 1.1* the climate change and the motivations for pursuing energy produced by nuclear fusion power plants are introduced. To have a more thorough understanding, nuclear fusion reactions and the plasma state are briefly explained in *Sections 1.2* and *1.3*, respectively. Once a general basis is obtained, there are different strategies which can be exploited to attain the goal of producing energy by nuclear fusion: they are briefly discussed in *Section 1.4*, before focusing more on the magnetic confinement (§*1.5*), which is the subject of the present thesis.

### 1.1 A global challenge

#### 1.1.1 The dependence on fossil fuels

The availability of energy has always been and still is one of the most important aspects in the development of our society. As many countries are starting just now their technological development and many others will follow, the human request for energy will certainly increase in the upcoming decades. At the same time, we are already witnessing the first steps of a global climate crisis due to a large extent to the main energy supply we are exploiting: fossil fuels. They are carbon-based energy sources, including coal, oil and natural gas and, as they exploit chemical reactions (combustion) to produce power, they lead to the production of carbon dioxide, arguably the greenhouse gas with the biggest impact because of its massive emissions in the atmosphere. As *Figure 1.1* depicts, fossil fuels provided more than 85% of the total primary energy supply and the percentage has not changed much up to 2019, being still above the 80%. Apart from the percentage, the total amount of energy supplied has almost tripled, implying a considerable increase of the fossil

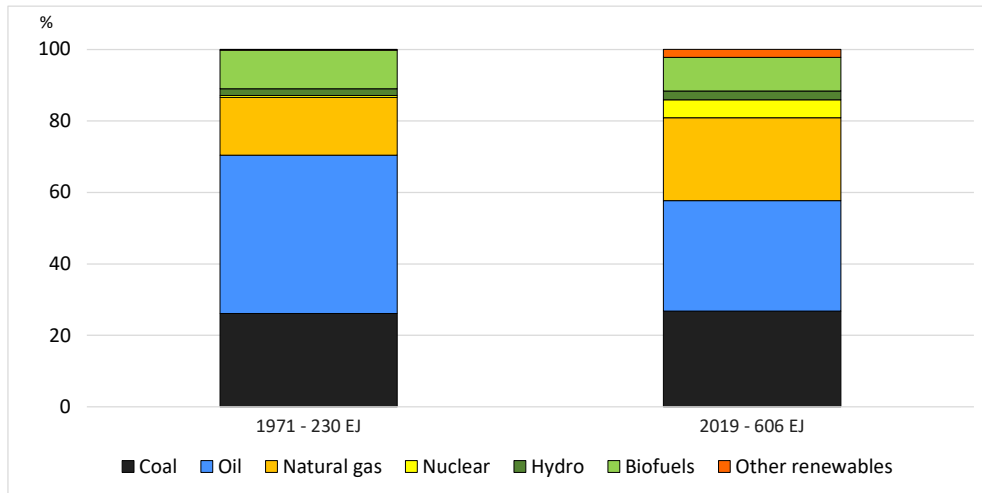


**Figure 1.1:** Total primary energy supply by fuel, 1971 and 2019 [1].

fuels utilization in that time-span.

The fact that energy demand keeps growing and that a significant portion of it is produced through fossil-fuels might result in a catastrophic global crisis that is likely to make parts of our world inhabitable by either drought or rising sea levels [2]. Accordingly, it is of paramount importance to try to mitigate as much as possible human impact on greenhouse gases production, including CO<sub>2</sub>.

To this, it must be added that fossil fuels are a limited resource and they are not distributed uniformly on Earth, causing conflicts for their control.

Because of these reasons, renewable energy production, such as hydroelectric, wind and solar, has risen over the last decades, as we can see from *Figure 1.1*. Though, these technologies present intrinsic problems:

- hydroelectric is bounded by the limited geographic availability, since they depend on the amount of water in any giving location, and they are significantly affected by droughts;
- solar and wind energy are dependent on geography as well, they suffer of severe intermittency and they have a small capacity factor if compared with fossil fuels or, especially, nuclear plants, since they depend on external elements to operate (sun and wind, respectively). The capacity factor is the ratio of the actual electricity generated divided by the maximum possible and therefore it is represented in percentages: *Figure 1.2* lists it for the main different technologies.

Even if the development of more advanced storage and transportation techniques

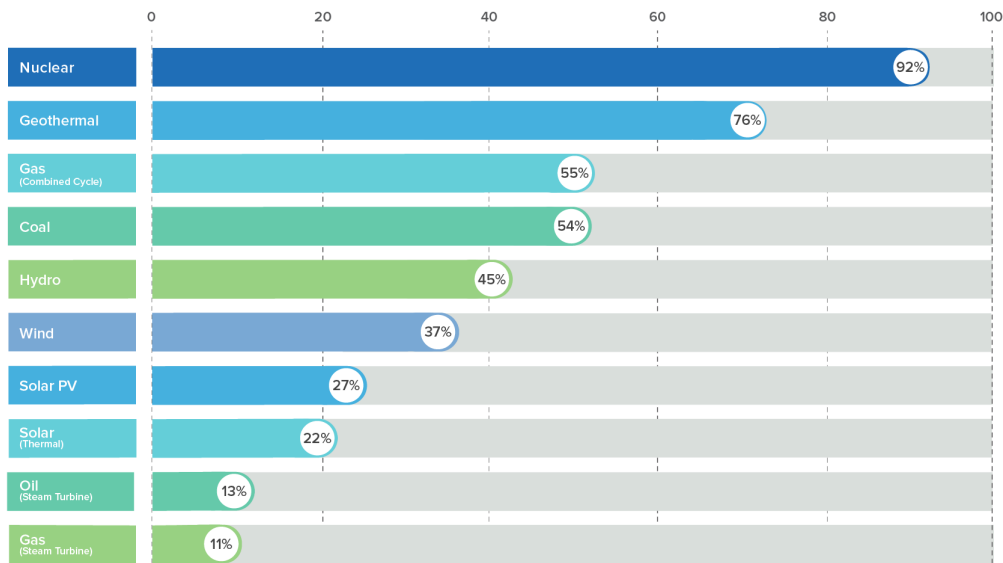


**Figure 1.2:** U.S. capacity factors by energy production technology in 2017 [3].

can alleviate the problem of intermittency, it is very unlikely that in the near future renewable energy sources will come close to cover the whole global energy demand.

### 1.1.2 Nuclear power plants

Since renewables cannot do everything by themselves and it is mandatory to reduce the usage of fossil fuels, an alternative base load energy source must be found and nuclear power plants can represent a suitable choice for more than one reason. They have one of the largest capacity factors among power plants (*Figure 1.2*), they do not suffer of intermittency and the fuel is widely available, considering also that not much of it is needed. Indeed, nuclear technologies for energy production are based on nuclear reactions (§1.2), which have a larger energy density with respect to other technologies by several orders of magnitude; moreover, they do not produce CO<sub>2</sub> during the operational phase. As it will be explained more thoroughly in *Section 1.2*, to produce energy starting from a nucleus the rationale is to make it react in order to move toward the most stable configuration, which is energetically favored. Since the most stable nuclides have a mass number  $A \approx 60$ , it is possible either to split a heavier atom or to fuse some lighter ones: the former is a nuclear fission reaction, while in the second case a nuclear fusion reaction will take place (the very same occurring inside stars, like the Sun).

Although, as mentioned above, there are two possibilities to retrieve energy from nuclear reactions, nowadays only nuclear fission power plants are operating. While

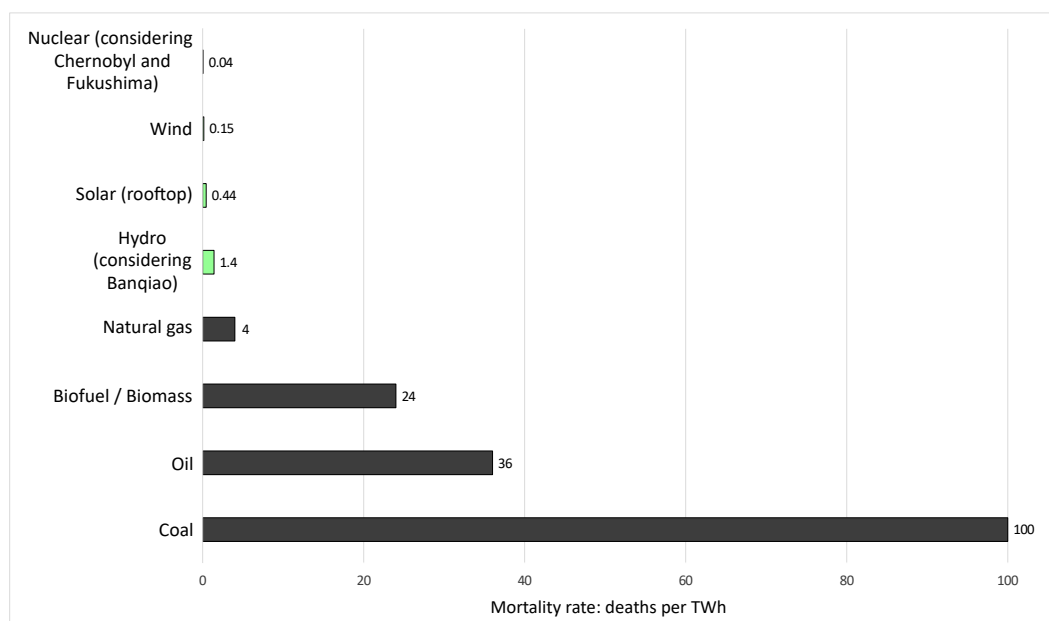


**Figure 1.3:** Mortality rate (deaths per TWh) for different technologies [4].

the intrinsic additional difficulties of making fusion reactions on Earth with respect to fission ones are discussed more in detail in the following (§1.2), it is worth to analyze why it can be nevertheless desirable to pursue nuclear fusion without settling for nuclear fission energy. Indeed, also the cons of every technology must be judged to be able to evaluate it as a whole and to compare it with the others, in order to make informed decisions. Even if a small amount of fuel is needed, the spent fuel disposal is an aspect that must be addressed. Today there is the technology to store it in safety, but it is anyway something that will remain radioactive above background levels for thousands of years. For these reasons, scientists came up with many encouraging ideas over the past decades: the new generation of fission reactors (Gen IV) will be able to produce less long-lived radioactive isotopes while at the same time burning fractions of the already produced spent fuel. Hopefully, this technology will bloom in the forthcoming future, but for the moment there is no definitive solution for this problem.

Nonetheless, the biggest drawback of nuclear fission is arguably its stigma, due to the military origin of the technology and to the two most serious civil nuclear accidents of all time: Chernobyl in 1986 and Fukushima in 2011. These events scared the whole world and people who lived them in first person still carry on their terrible memories, that in many instances are stronger than physics, critical judgment and scientific data. It goes without saying that public opinion is of fundamental importance for country policies, which determined an early phase-out

from nuclear in different countries, such as Germany, Belgium and Switzerland. Even if this was accompanied by huge investments on renewables, as explained before this is likely to be a huge loss from the long-term sustainability point of view. What is even more appalling is that, contrary to popular belief, scientific evidence demonstrates how nuclear fission technology has one of the lowest rate of deaths per unit energy produced, even considering the two above-mentioned accidents (*Figure 1.3*).

The large fossil fuels figures (depicted in black) are by large extent due to the air pollution: indeed during the combustion process they release not only CO<sub>2</sub>, but also a wide variety of other pollutants that are strongly linked with cancer and hearth diseases, among many others.

### 1.1.3 The role of nuclear fusion

Even if right now nuclear fission energy would be the best partner for renewables in many respects, it is paying (and it will likely do so in the near future as well) a very bad reputation, that drives both investors and politicians away from it. Mainly because of all these causes, the possibility of producing nuclear fusion energy on Earth is becoming more and more appealing. This technology could provide a reliable and large-scale energy production, being at the same time inherently safe and producing a small amount of greenhouse gases in the life cycle. This encourages a rapid development, in such a way to have it available for the energy mix as soon as possible. Specifically, the European Union goal is to have nuclear fusion electricity in the grid by the second half of the century [5]. To do this, there will be two necessary major steps: the first is ITER [6], the biggest nuclear fusion experiment so far, that has the objective of producing more fusion power than the electricity it is needed for the plant to work, providing feasibility of the nuclear fusion technology for energy production. The second stage will instead be the European DEMO, a demonstrative fusion power plant with the objective of sending fusion electricity to the grid [5]. By all means, many other “minor” steps are needed in the passage between ITER and EU-DEMO: they will consist in smaller experimental facilities focused on some of the most critical aspects (or even a single one) to build eventually a nuclear fusion power plant.

Apart from the European approach, there are countries and private companies worldwide that are pursuing different paths to attain nuclear fusion power, with the hope of making it available much earlier.

The main approaches to attain nuclear fusion will be discussed in following sections (§1.4-1.5), after a concise introduction to the physics that sustains such an innovative possibility to produce energy.

## 1.2 Nuclear reactions for energy production

### 1.2.1 Nuclear energy fundamentals

Nuclear fission and fusion reactions are specific kinds of nuclear reactions, which in general involve at least a nucleus and a particle (that can possibly be another nucleus). A single nucleus is formed by nucleons (protons and neutrons), whose total number defines its mass number  $A$  and that are kept together by the strong nuclear force, that overcomes electromagnetic repulsion between protons. By measuring the mass of nuclei, it is possible to discover that they are smaller than the sum of the masses of their constituents: this leads to the definition of the mass defect:

$$\Delta_m = ZM_p + (A - Z)M_n - M_{nucl} \quad (1.1)$$

where  $M_n, M_p$  are respectively the mass of a single neutron and proton,  $A$  is the above-mentioned mass number and  $Z$  is the atomic number (number of protons within a nucleus). Consequently, the very famous Einstein's formula  $E = mc^2$  can be exploited to work out the binding energy of a nucleus, that is the smallest supply of energy necessary to dismantle the nucleus into individual nucleons:

$$B = \Delta_m c^2 \quad (1.2)$$

where  $c$  is the speed of light in vacuum ( $c \approx 3 \cdot 10^8$  m/s). Since in a nuclear reaction the total number of nucleons must be conserved, if the products are more stable than the reactants (higher binding energy per unit nucleon), they will have a correspondingly higher mass defect per unit nucleon. Thus, again accordingly to Einstein's formula, the missing mass has been translated into kinetic energy available for the products, shared according to momentum balance. Because of this, it is very useful to plot the binding energy per unit nucleon as a function of the mass number (*Figure 1.4*), to understand how energy can be extracted from nuclei. Since the peak of the curve (the lowest rest mass per unit nucleon) is at  $A \approx 60$ , there are two different feasible strategies: either the heavy nuclei are split into nuclei closer to the peak, or light nuclei are fused together, again to move toward the most stable region. In the first instance the reactions will be of nuclear fission, while in the second case of nuclear fusion. Considering that the curve is much steeper in the light region, the fusion energy density is much higher than the fission one and this clearly reveals an additional interest in nuclear fusion reactions to produce energy. Though, it is evident how in the world we have a lot of nuclear fission reactors but not even a single fusion power plant. This is due to an intrinsic difference of the two processes: while to fission a heavy nucleus it is possible to exploit neutrons, which lack of electrical charge and, hence, do not experience Coulomb repulsion, to fuse two light nuclei they must have an energy that allows them to be sufficiently close ( $\approx 1$  fm), in order for the strong nuclear

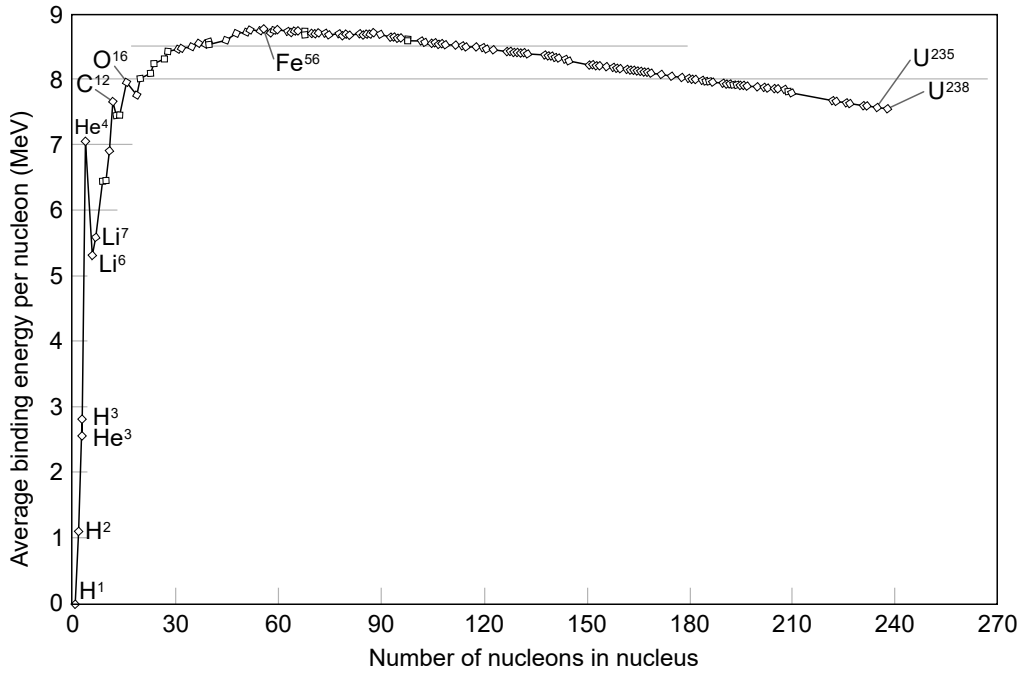


**Figure 1.4:** Average binding energy per unit nucleon versus the mass number.

force to become predominant with respect to the Coulomb repulsion. Qualitatively speaking, the repulsion strength depends also on the charge of the two nuclei and for this reason it is preferable to use low- $Z$  nuclei.

To put the supplementary difficulty of fusion reactions into quantitative terms it is useful to introduce the concept of cross-section  $\sigma$ , that is the probability that a certain reaction occurs (with dimensions of an area, often measured in barns,  $b = 10^{-28} \text{ m}^2$ ) and it is a function of the relative velocity between the reactants. By looking at the ordinate of the graphs in *Figure 1.5* it is evident how the likelihood of two processes are distinguished by orders of magnitude: the peak cross-section of the most probable fusion reactions (in that energy range) is  $\approx 5 \text{ b}$ , while the fission cross-sections of fissile nuclei rise up to thousands of barns for thermal neutrons.

### 1.2.2 The most desirable fusion reactions

The choice of the best fusion reactions to exploit for energy production on Earth must account for both the probability of it happening and the energy released per reaction. By looking at *Figure 1.4*, the relatively huge value of the average binding energy per unit nucleon of  ${}^4\text{He}$  (helium nucleus, identical to an alpha particle) stands out: this is strongly connected to the fact that reactions that have  ${}^4\text{He}$  among the product are likely to have a larger energy emission. The three most

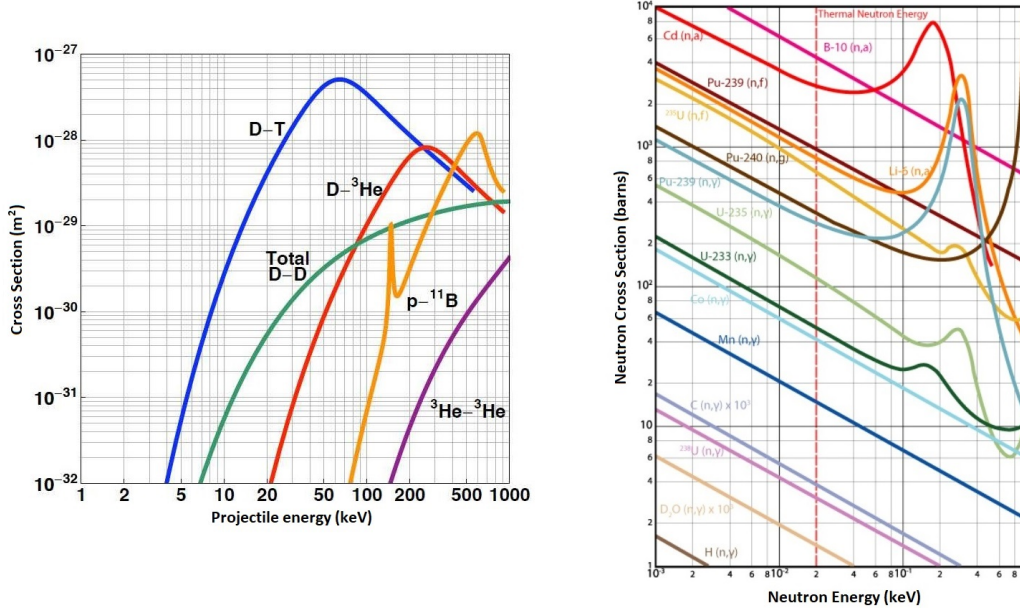
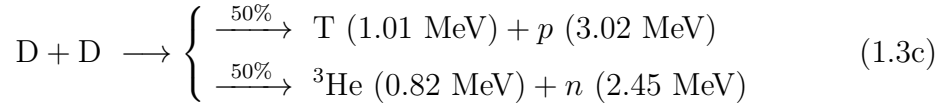
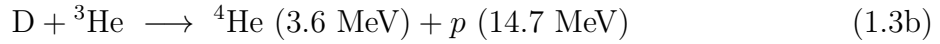
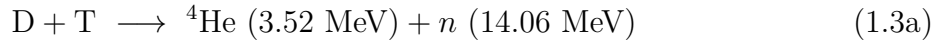


**Figure 1.5:** Cross-section of different kinds fusion reactions as a function of the energy of one of the two reactants (left). Cross section for various processes induced by neutrons as a function of neutron energy in the thermal spectrum (right).

probable fusion reactions according to *Figure 1.5* involve the use of deuterium (D) and Tritium (T), two isotopes of hydrogen, and their complete formulation reads:



Among these reactions, D-T has by far the largest cross section at energies below 100 keV and this will remain true also considering that in applications the particles at play are not just two, but an ensemble characterized by a certain velocity (and hence energy) distribution. At the same time, it is also among the ones releasing the biggest amount of energy. These two characteristics make D-T reactions the most suitable ones to be exploited for power generation by fusion, at least at the first stage.

The main drawback is that tritium is radioactive, with a half-life of about 12.3 years and hence it must be produced artificially. While there will be the possibility to generate it on site exploiting the first fusion reactions (§1.5), tritium availability for the start phase of the fusion reactors remains an open question [7]. Moreover,

the fact of having a radioactive fuel (plus the activation of reactor materials caused by the neutrons produced through the reaction) makes a fusion power plant a full-fledged nuclear one, with all the limitations from the regulatory and safety points of view that it may imply.

Deuterium, instead, is a stable nucleus and it accounts for  $\sim 0.016\%$  of the hydrogen in the oceans: this allows to extract the “heavy” water ( $D_2O$ ) through isotope separation and to exploit electrolysis to obtain solely deuterium.

D- $^3\text{He}$  reaction could be attractive as well, since it releases the largest energy among these reactions, there is no radioactive fuel and no neutron production (that easily activates and damages reactor materials). Apart from the much lower likelihood of happening, the other shortcoming is the availability of  $^3\text{He}$ , which is rare on Earth and difficult to produce.

D-D reaction, instead, is fascinating because of the fact that it involves deuterium nuclei only. Though, apart from the much smaller cross section with respect to D-T reactions, they also have the smallest energy released among the three.

To understand which are the possibilities to translate this theoretical knowledge in truly existing systems able to produce energy (§1.5), a very short, though profoundly necessary, excursus on plasma state must be made.

## 1.3 The plasma state and its connection with nuclear fusion

### 1.3.1 What is a plasma?

Plasma can be considered one of the four fundamental states of aggregation of matter (together with solid, liquid and gas) and it is the most abundant form of ordinary matter (excluding, then, dark matter and dark energy) in the universe. What differentiates the plasma state is that it is significantly influenced by electromagnetic interactions: indeed its peculiar constituents are electrically charged populations, namely ions and electrons (plus possibly neutral species, depending on the degree of ionization). Plasmas are generally quasi-neutral, meaning that they are globally neutral considering sufficiently large spatial scales (§1.3.2).

It is possible to characterize plasmas utilizing two parameters: the plasma density  $n$  and the temperature  $T$ . As it is very common in plasma physics, the temperature is measured in energy units: this conversion is made possible thanks to the Boltzmann constant:  $k_B T \rightarrow T$ . Just for a quick reference, one must keep in mind that 1 keV corresponds to  $\simeq 12$  million K. This is the convention that will be adopted throughout this work as well.

### 1.3.2 The Debye length

As said before, plasmas are significantly affected by electromagnetic field and so it can be of interest to study the polarization property of the system in an electrostatic sense: an external charge  $q$  from outside is put inside the plasma and its effects on the other charged particles are evaluated at equilibrium. To do this, it is possible to solve Poisson equation, that, assuming for simplicity singly charged ions, reads:

$$\varepsilon_0 \nabla^2 \phi = -\rho_{\text{tot}} = -[e(n_i - n_e) + q\delta(\mathbf{x})] \quad (1.4)$$

where  $e$  is the elementary charge (the absolute value of the electric charge of a single electron),  $\phi$  the electrostatic potential,  $\rho_{\text{tot}}$  the total charge density (hence including the external charge  $q$ ),  $n_e$  and  $n_i$  are, respectively, the electron and ion charge density and  $\delta$  is the Dirac delta function.

To solve this differential equation, some assumptions are done:

- the plasma is infinitely extended and at infinity the particle density is equal to  $n_0$  the unperturbed one;
- equilibrium conditions: to describe the distribution of ions and electrons particle densities in the presence of a potential profile, Boltzmann relation can be used:  $n = n_0 e^{-U/T}$ ;
- the spherical symmetry is exploited:  $q$  is taken as the origin and only the radial coordinate matters (the distance with respect to  $q$ );
- the equation is linearized: the corresponding physical assumption is that the potential energy ( $|U| = |e\phi|$ ) is much smaller than the thermal energy ( $T$ ) for both ions and electrons. This means that  $e^{-U/T} \approx 1 - U/T$ .

In this way, the Poisson-Boltzmann linearized equation will be yielded:

$$\varepsilon_0 \nabla^2 \phi = \varepsilon_0 \frac{1}{r} \frac{d^2}{dr^2} (r\phi) = n_0 e^2 \left( \frac{T_e + T_i}{T_e T_i} \right) \phi - q\delta(\mathbf{x}) \quad (1.5)$$

Dividing by  $\varepsilon_0$ , the coefficient of  $\phi$  on the right-hand side must have the dimensions as the square of the inverse of a length, since it must be coherent with the Laplace operator. Hence, it is possible to define a length that will have a fundamental role in plasma physics:

$$\lambda_D = \sqrt{\frac{\varepsilon_0 T_e T_i}{n_0 e^2 (T_e + T_i)}} \quad (1.6)$$

By solving *Equation (1.5)* adopting the definition (1.6), the electrostatic potential is:

$$\phi(\mathbf{x}) = \frac{q}{|\mathbf{x}|} \exp\left(-\frac{|\mathbf{x}|}{\lambda_D}\right) \quad (1.7)$$

which has the form of a Yukawa potential. While in vacuum a charge  $q$  would produce a Coulomb potential (i.e. going as  $q/r$ ), within a plasma it is screened through an exponential that goes quickly to zero as the distance from the charge increases. Within distances smaller than the Debye length, charged particles will interact more or less as it is expected in vacuum, while at larger distances the screening is increasingly dominant. This does not mean that there will not be interactions at lengths larger than  $\lambda_D$ , but that they will be related with the overall behaviour of the system, mediated by the long-range electromagnetic field; the short-range one will instead affect what happens within the Debye length.

This shielding phenomenon occurs thanks to the rearrangement of plasma particles, that move in such a way to shield the charge  $q$ : it is a result of a collective interaction among many bodies (indeed inside the expression for  $\lambda_D$  there is  $n_0 e^2$ ). If the considered charge  $q$  is positive, the electron density close to it will increase to try to balance it (and vice versa for a negative charge, that will attract the ions). Even if up to now  $q$  has been considered an external charge, if it was just a charged particle from the plasma it would not behave differently: a plasma particle can be thought as either the center of the screening or as one of the bodies that produce it for another particle.

### 1.3.3 Laboratory production

A possible mechanism to change state of aggregation of matter is to raise the temperature up to a sufficient level in which the bonds that keep matter together are significantly affected (for simplicity pressure is considered constant). Apart from the well-known transitions between solid, liquid and gas, it is conceivable to apply the same also for plasmas. Indeed, by simply raising the temperature of a gas up to a certain level, the collisions among neutrals can be so energetic to produce themselves ionizations, that will accordingly be called thermal ionizations. Since the binding energy of electrons in a light molecule are on the order of tens of eV, exploiting the above-mentioned relationship between energy and temperature this means that thermal ionization is achieved at  $T \sim 10^5$  K.

An alternative way to generate plasmas in laboratory is to employ electric discharges in a gas that is initially neutral and in equilibrium. Indeed, by applying a sufficiently strong electric field, electrons can be stripped from their atoms and they are accelerated: when they reach a sufficiently high energy, they can produce additional ionization colliding with other neutral atoms of the gas. The simplest instances in which one can observe this, is in neon tubes and fluorescent lamps.

Even if these two methods have been employed in the past to study and better comprehend the plasma state, they are not at all suitable for the purpose of energy production and other solutions are needed.

### 1.3.4 Plasmas in nature

In nature there exist plasmas that span huge ranges of these two parameters: *Figure 1.6* reports some examples that can be found in the universe (one must pay attention to the fact that it is a logarithmic plot for both temperature and density).

A very familiar example of plasma is the Sun, together with the other main sequence stars. In particular, the core of the Sun has a temperature of  $\sim 10^7$  K, a pressure of  $\sim 10^5$  Mbar and a mass density of  $\sim 10^2$  g/cm<sup>3</sup>. The Sun is able to burn thanks to these extreme parameters found in its core, which are enough to make the probability of nuclear fusion reactions appreciable, constituting a thermonuclear plasma. Even if looking at how stars produce energy can be of inspiration to try to do something similar on the Earth, the conditions are absolutely not replicable. The reactions occurring in the Sun's core (hydrogen fusing into helium) have a too low probability to be reproduced in laboratory: they can occur in that environment

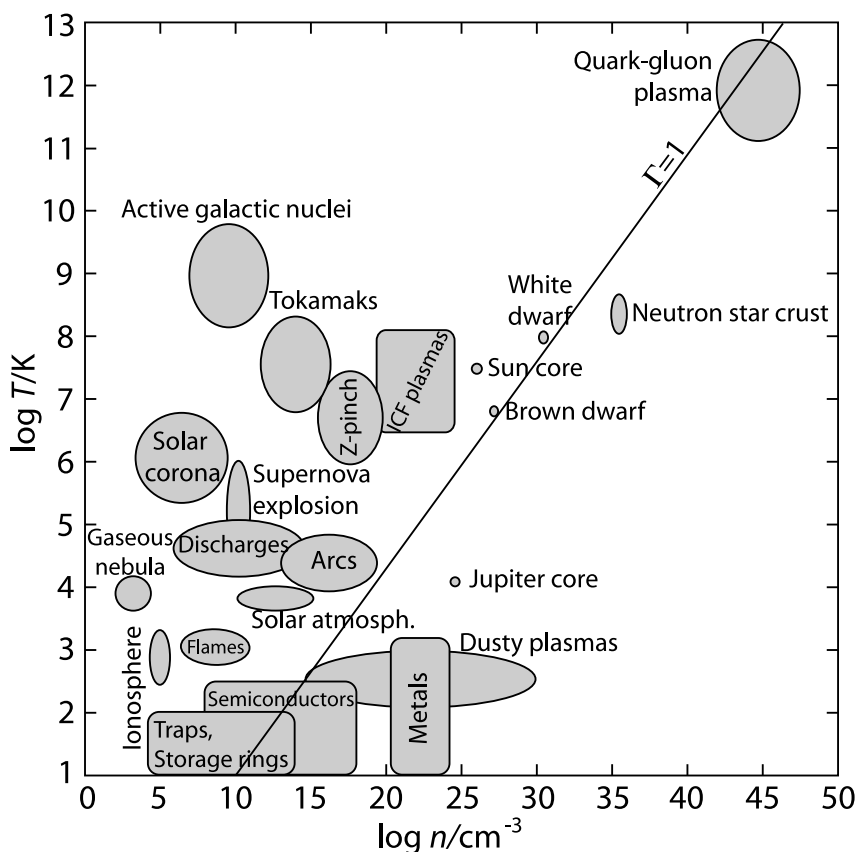


**Figure 1.6:** Different kinds of plasmas that can be found in the universe as a function of particle density  $n$  and temperature  $T$  [8].

thanks to the gravitational confinement, that implies a large particle density and which can maintain a stationary energy production. Moreover, in the Sun the energy is not released in an efficient way in terms of energy per unit mass: theoretical models of its interior indicate a maximum power density of  $\sim 276.5 \text{ W/m}^3$  at the center of the core [9]. Thus, different paths are needed to produce fusion energy in laboratory.

### 1.3.5 Connection with nuclear fusion

If the aim was just to make nuclear fusion reactions, one could think of a very simple setup: a particle accelerator could give energy to a beam of ions, say D ions, in order to hit a target of the other reactant. Albeit feasible, this is not suitable for energy production for two main reasons:

- to have fusion reactions, a big amount of energy must be spent in the first place, in order for the ion beam to be enough energetic to overcome the Coulomb barrier;
- most of the energy is lost in much more likely reactions other than fusion ones, such as ionization, excitation and so forth.

Apart from the limits for energy generation, this is nonetheless a satisfactory process for neutrons production.

Since the objective is to have eventually a contender against fossil fuels for energy production at a global level, there must be a positive net energy generation and it must be also sufficiently large, in order to be economically competitive. The system can require some energy to maintain the working parameters, but it is imperative that it releases more of it than what it needs.

Taking inspiration from the Sun and the other stars, an idea is to directly employ ionized matter, in such a way to remove the possibility of other processes. Sure enough, all the main different approaches to produce energy from nuclear fusion on Earth (§1.4) exploit the reactants in the plasma state.

## 1.4 How to attain fusion on Earth

### 1.4.1 The Lawson criterion

Summarizing what has been said in the previous sections (§1.2-1.3), the most feasible way to build a nuclear fusion power plant is to exploit D-T reactions and to do so having them in the plasma state. Not only, one must put attention also on the properties of such a plasma and the operational parameters, according

to an energy balance to be performed on the plasma. In these terms, figures of merit are the temperature  $T$ , the particle density  $n$  and the confinement time  $\tau_E$ , that is the characteristic time in which it is possible to keep the plasma with the above-mentioned parameters. These three parameters play a fundamental role in the renowned Lawson criterion [10], that reads:

$$p\tau_E = 2n\tau_ET \geq \frac{24T^2}{E\langle\sigma v\rangle - 4c_B Z_{\text{eff}}^2 \sqrt{T}} \quad (1.8)$$

where  $p = 2nT$  is the plasma pressure,  $\langle\sigma v\rangle$  is the reaction rate (if multiplied times the density of each species it gives back the number of reactions per unit volume and per unit time) for D-T reaction, averaged over a Maxwellian distribution for both species,  $c_B$  is a numerical constant and  $Z_{\text{eff}}$  is the effective atomic number of the plasma (equal to 1 for a pure D-T mixture).  $E$  must be instead addressed with more attention, since it is the energy input for the plasma itself. A single D-T reaction produces an alpha particle and a neutron: while the former is electrically charged and can then interact effectively with the rest of the plasma, the latter is neutral and it is very likely to leave the plasma without depositing its energy at all. Thus, the  $E$  in this equation is actually  $E_\alpha$ , the fusion energy possessed by the alpha particle (3.52 MeV) that will be distributed among the particles of the plasma. The remaining part of the fusion energy (14.06 MeV), owned by the neutron, is exactly the energy to be collected from the power plant point of view: this kinetic energy will be converted before in thermal one and eventually in electric energy.

The inequality (1.8) describes the conditions to have a self-sustained situation: part of the produced energy (the alphas particle fraction) is exploited to keep the system in the required condition to keep burning fuel. Thus, that energy source (from the plasma point of view) has to balance the energy loss terms, which are assumed in [10] to be just radiation losses due to processes like Bremsstrahlung radiations and heat fluxes that diffuse with a characteristic time  $\tau_E$ . This expression indicates the requirements to reach, at least, the before-mentioned equilibrium condition, that is also called *ignition condition*. The goal for future power plants is to fulfil this condition for as long as possible, since in that case the neutron energy will be exploited to produce electric energy.

Since the right-hand side of the expression (1.8), once chosen the reaction and computed  $Z_{\text{eff}}$ , is just a function of the temperature, it is possible to compute its minimum and evaluate the values of the other two figures of merit to satisfy the relation. It is possible to do so through the product  $n\tau_ET$  (of which  $T$  is known if it is selected to minimize the right-hand side), also known as triple product.

From *Figure 1.7* it is possible to appreciate the right-hand side of inequality (1.8) for D-T reactions as a function of the temperature: it is the upper-most reddish curve and it displays a minimum at  $\sim 15$  keV, that are  $\sim 170$  million K. Ignition

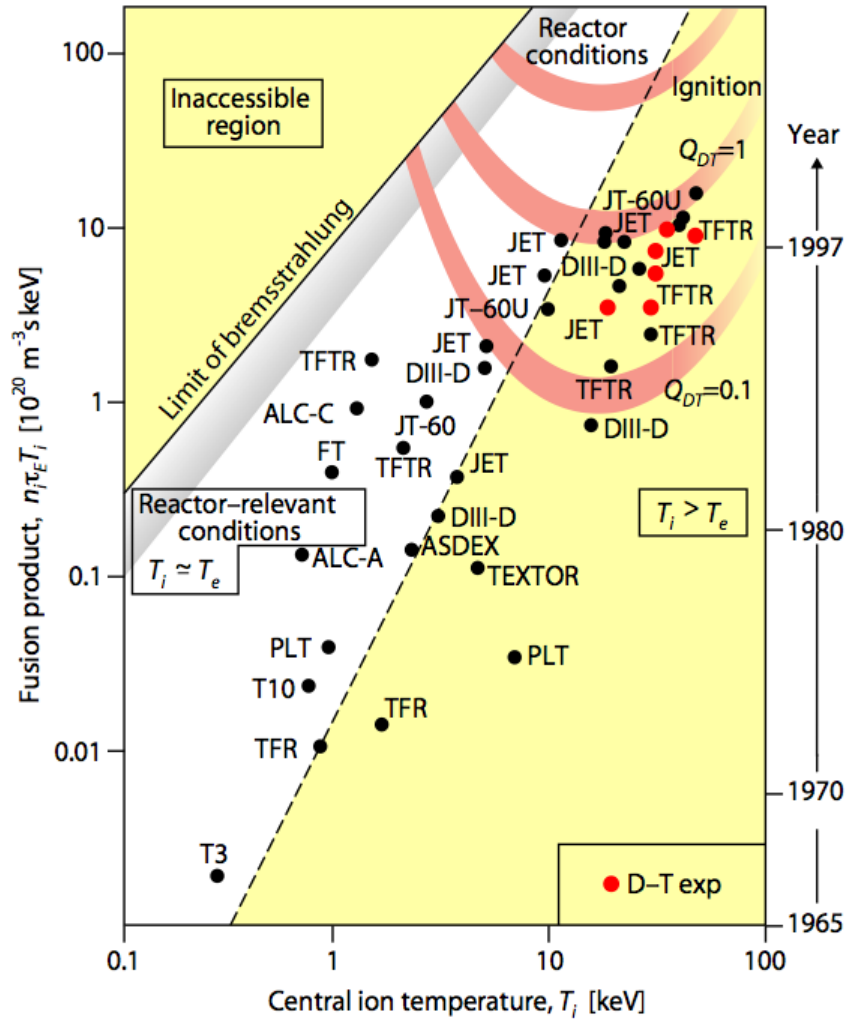


**Figure 1.7:** Triple products of fusion experiments up to now in comparison to curves needed to reach, from top to bottom, ignition conditions,  $Q=1$  or  $Q=0.1$  (in red) [11].

is an ideal condition since the only source term of the energy balance equation for the plasma is the energy coming from alpha particle. Though, since it is not easy at all to attain (indeed, again from *Figure 1.7*, all current and past experiments are way below the upper curve), for the moment an external supplier of energy is needed, in such a way to have an additional source to the energy balance. It is worth at this point to define another parameter in order to quantify how close one is with respect to ignition: the “fusion gain”  $Q$  is the fusion power divided by external power provided to the system. Even if not enough to produce electric

power,  $Q$  needs at least to be greater than 1: if it is so, the system works as an energy amplifier, with the limit of  $Q$  going to infinity when ignition is reached. In *Figure 1.7* the middle curve refers to a unitary  $Q$ , while in the lower curve it is equal to 0.1, showing that experiments up to know are still quite far from the ideal case.

### 1.4.2 Two possibilities to produce nuclear fusion energy

For the reasons explained in *Section 1.2*, the most promising reaction is D-T; once chosen the temperature that minimizes the triple product ( $\sim 15$  keV), the multiplication of confinement time and particle density evaluated at ignition condition reads:

$$(n\tau_E)_{\text{ign}, T_{\text{min}}} \simeq 2 \cdot 10^{20} \text{ m}^{-3}\text{s} \quad (1.9)$$

Thanks to this relation, the plasma that one can have in mind for energy production starts being better specified. To achieve such a value for the product  $n\tau_E$ , two possible pathways can be followed:

- magnetic confinement fusion (MCF): the plasma is relatively diluted ( $n \sim 10^{20} \div 10^{21} \text{ m}^{-3}$ ) but confined for a larger time (macroscopic  $\tau_E$ , on the order of the second) exploiting suitable magnetic field configurations;
- inertial confinement fusion (ICF): a plasma with the needed properties is built and then it is let free to break apart:  $\tau_E$  is connected to the characteristic inertial time that this process takes. Estimates according to the wanted properties lead to  $\tau_E \sim 10^{-9}$  s, corresponding to a much higher density ( $n \sim 10^{29} \div 10^{30} \text{ m}^{-3}$ ).

MCF is probably the most investigated and notorious option between the two and it constitutes the framework of this thesis work as well.

### 1.4.3 Tritium production and energy extraction

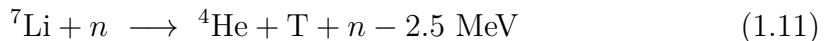
The extraction of the energy from the neutrons produced by D-T reaction is strongly connected with the possibility of producing tritium directly on-site. For instance, the neutron-induced fission of a  ${}^6\text{Li}$  nucleus lead to the generation of an alpha particle and a tritium nucleus:



Not only this reaction has the big advantage of being exothermic, releasing further energy to the system, but it has an extremely high cross section when neutrons have low energies (close to thermal ones) as *Figure 1.5* shows (orange curve). Since

the products are charged particles, which are able to slow down very quickly in matter, this additional source of energy will be translated into heating of the matter. Lithium is very abundant in the Earth’s crust and in sea water at the point that the global deuterium and lithium resources can satisfy the world’s energy demand for millions of years, making fusion a virtually unlimited energy source [5]. There are two isotopes of lithium, both stable:  ${}^6\text{Li}$  has an abundance of 7.6%, while the majority of it is  ${}^7\text{Li}$  (92.4%).

Also this second isotope can undergo a fission reaction, but with a threshold on the neutron energy, that must be higher than 2.5 MeV:



These two reactions fit together almost perfectly for the purpose of a fusion power plant. Following *Reaction (1.3a)*, neutrons have a great amount of energy, equal to 14 MeV. Though, such high values are very helpful to induce  ${}^7\text{Li}$  fission, and this opens up the possibility of having a tritium breeding ratio (TBR, the ratio of tritium produced with respect to the burnt one)  $\geq 1$ , that will be essential at the beginning to allow successive power plants to start up [5]. Indeed, *Reaction (1.11)* is able to generate, apart from a tritium nucleus, an additional and less energetic neutron, that is more likely to react with  ${}^6\text{Li}$  that in turn can generate another T nucleus. If this is the chain of events, for a single tritium burnt following a nuclear fusion reaction inside the plasma, two of them are produced.

Since lithium is a light atom, it can also be exploited effectively as a moderator to slow down the fast neutrons that do not induce *Reaction (1.11)*: the more they are slowed down, the higher the probability of *Reaction (1.10)*. Moreover, while neutrons are slowing down they share their energy with matter in the form of heat, meaning that at this point it can be exploited to heat up a heat-carrier fluid part of a conventional thermodynamic cycle, that will produce electric energy through turbines, alternators and so on.

Hence, the most investigated idea up to now is to surround the thermonuclear plasma with lithium. For this reason, this part of the system is called (tritium breeding) blanket and it is crucial since it provides a way to produce both the fuel and the electric energy.

## 1.5 Magnetic confinement fusion

### 1.5.1 Basic principles of magnetic confinement

To understand why it is possible to exploit the magnetic field to confine charged particles, it is easier to refer to single charged particles. Each charged particle is

subjected to Lorentz force, that in SI units reads:

$$\mathbf{F} = q(\mathbf{E} + \mathbf{v} \times \mathbf{B}) \quad (1.12)$$

where  $\mathbf{F}$  is the force felt by the particle with charge  $q$  and velocity  $\mathbf{v}$  and  $\mathbf{E}$  and  $\mathbf{B}$  are respectively the electric and the magnetic fields. In the simplest case, considering no electric field and a uniform  $\mathbf{B}$ , the particle will perform a gyration motion in the plane perpendicular to the direction of the magnetic field lines with the following frequency and radius:

$$\Omega = \frac{q|\mathbf{B}|}{m} \quad \rho_L = \frac{v_\perp}{\Omega} \quad (1.13)$$

$\Omega$  is called gyrofrequency, while  $\rho_L$  is the Larmor radius;  $m$  is the charged particle mass and  $v_\perp$  is the particle velocity on the plane orthogonal to  $\mathbf{B}$ . Though, since the confining force acts always perpendicularly to the magnetic field, the particle cannot be confined along it since the parallel velocity  $v_\parallel$  will be constant and equal to the initial conditions. Therefore, an intuitive solution could be to just close the field lines on themselves, creating a torus shape. Though, removing the simplifying hypothesis the so-called “drifts” make their appearance, strongly influencing the dynamics and not allowing the confinement with a purely toroidal magnetic field [13]. To be able to counteract this, the magnetic field needs a poloidal component, that is the angular component taking as a reference a polar system of coordinates with center in the axis of the torus. Summing the two components, the resulting field lines will be wrapping helicoidally around a torus surface. This geometry is displayed in *Figure 1.8*.

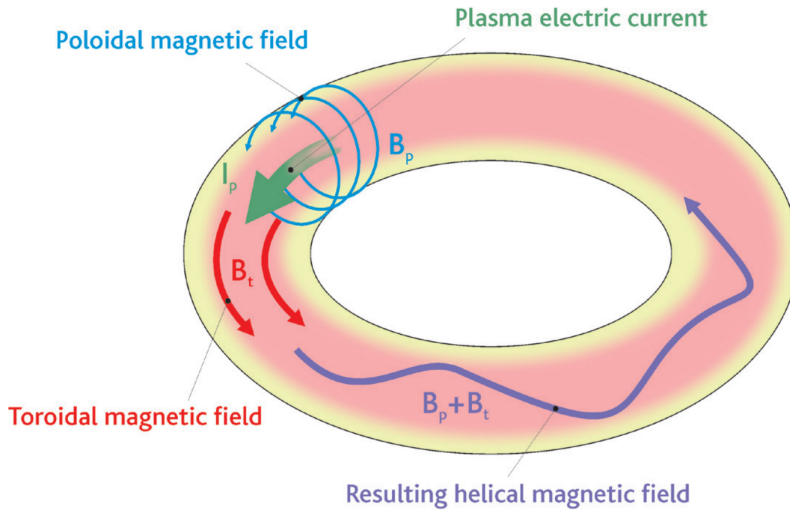


**Figure 1.8:** Magnetic confinement of a plasma in a tokamak [12].

## 1.5.2 Leading MCF approaches

To generate these two components of the magnetic field, two main concepts have been investigated so far:

- the tokamak. This idea was introduced by Tamm and Sakharov, two Russian physicists and the name is a Russian acronym for *toroidal machine with magnetic coils* [15][16][17]. The toroidal magnetic field is generated through the so-called toroidal magnetic field coils (the electric current goes in the poloidal direction), which approximate a torus-shaped solenoid. The poloidal component of the magnetic field, is instead generated by a toroidal electric current that flows inside the plasma itself. *Figure 1.8* clearly shows the tokamak geometry and puts in evidence the plasma current generating the needed poloidal component. This current is produced exploiting the transformer principle, considering the plasma as the secondary winding and exploiting as primary another set of coils, the central solenoid. This is one of the main drawbacks of this technology, since to have a toroidal plasma current always in the same direction a varying concatenated magnetic field flux is required but it can not do so indefinitely: the machine has to be pulsed if this is the only way to drive a significant plasma current. Additional coils generate a vertical magnetic field for equilibrium reasons (poloidal field coils). A schematic representation of the tokamak geometry highlighting the geometry of the coils and the components of the magnetic field lines is displayed in *Figure 1.9*.
- The stellarator, proposed by Spitzer, an American physicist [18]. In this case, external coils provide both toroidal and poloidal components of the magnetic field. The most important advantages are that current can be controlled from

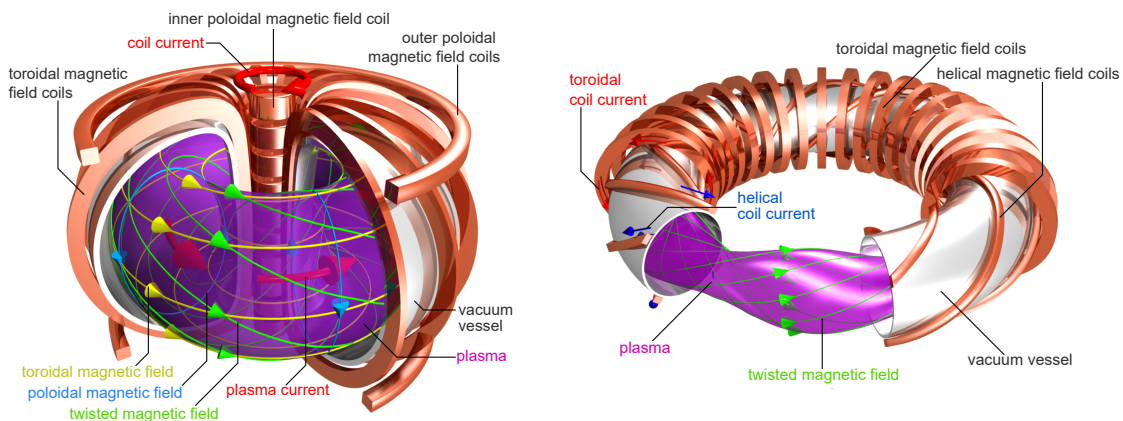


**Figure 1.9:** Schematic representation of the tokamak (left) and stellarator (right) devices, with a focus on their magnetic coils configurations [14].

the external and that it can work in a continuous way, but this comes at the price of a very complex coil structure and the loss of toroidal symmetry. *Figure 1.9* illustrates the stellarator concept next to a tokamak one, in order to appreciate the differences in terms of the shapes and typology of the coils used.

The work presented in this thesis is potentially applicable to both technologies, but hereafter the focus will be entirely on the tokamak concept, since it is in a more advanced development stage.

### 1.5.3 Tokamak progress and future objectives

A number of tokamaks has been built in the 70s and 80s of the 20<sup>th</sup> century; just to mention the most well-known ones, they include JET (Joint European Torus) in Culham, UK, ASDEX-Upgrade in Garching, Germany and JT-60 in Naka, Japan. In particular, JET is the biggest operating tokamak up to now and in 1997, employing a D-T plasma, it achieved a fusion power of 16 MW, that is still a record for a tokamak device [19].

As briefly introduced in *Section 1.1.3*, the largest and most advanced MCF experiment so far is ITER, under construction in Cadarache, France [6]. It constitutes an international effort since its members are China, the European Union, India, Japan, Korea, Russia and the United States: they will share the cost of project construction, operation and decommissioning, but also the experimental results and any intellectual property generated by the project [6]. ITER main goals are [5]:

- to produce, at peak performance, 500 MW of fusion power with only 50 MW from the external, implying a gain factor  $Q \simeq 10$ . This power will not be aimed at electricity production, since in ITER a real blanket will not be present (§1.4.3);
- to demonstrate magnetic confinement fusion at near power plant size;
- to test vital technologies to make further progress;
- to test the feasibility of tritium generation on-site, via TBMs (test blanket modules).

The first plasma operation is foreseen in 2025, employing He and D plasmas, while tritium will be utilized only from 2035.

After the objective of ITER will be hopefully fulfilled, it will be the time for the European demonstrative power plant EU-DEMO (simply called DEMO hereafter). Its pre-conceptual design started in 2014, but the procurement and construction

phase will not start before 2040, in order to exploit at best the results that ITER will deliver. DEMO will mark the very first step of fusion power into the European energy market, supplying electricity to the grid and, apart from this, the other major objectives are [5]:

- to breed its own tritium;
- to demonstrate materials suitable for handling the high neutron flux;
- to exhibit safety and environmental sustainability;
- to provide sufficient technology to allow a first commercial fusion power plant to be built;
- to supply the basis for an assessment of the economic viability of a fusion power plant.

Figure 1.10 displays an illustrative roadmap of the MCF fusion program in Europe, highlighting its milestones and the passage of information that must exist from ITER to DEMO.

Unquestionably, the success of ITER experiment will be fundamental for DEMO development, but it will not be sufficient alone. This is because ITER working conditions are not fully representative of DEMO and extrapolations could be very

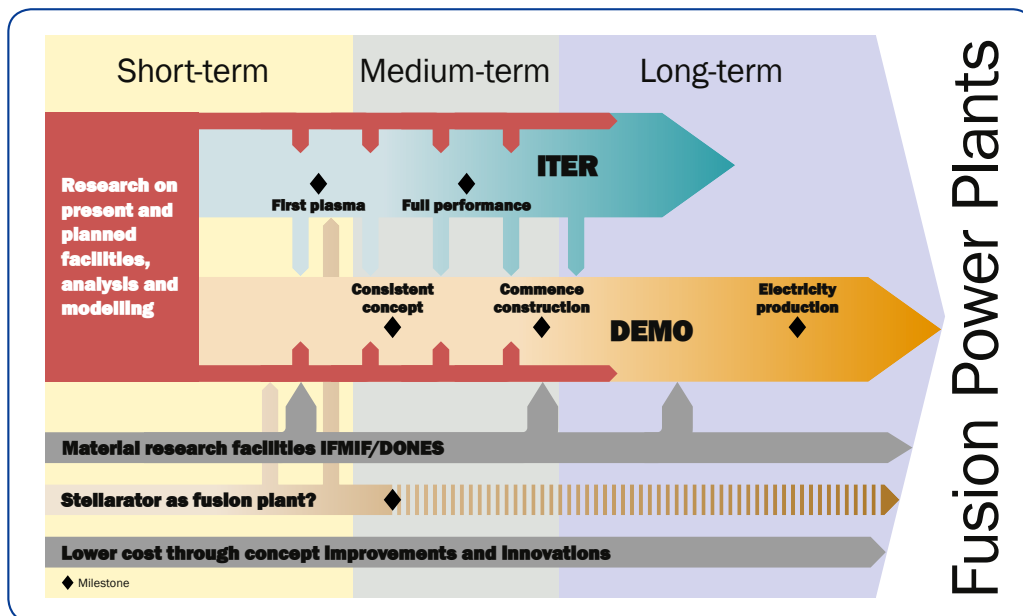


Figure 1.10: The European roadmap in a nutshell [5].

dangerous. In the European strategy, no large tokamaks are foreseen in between the two, rather there will be different facilities that will address specific problems that ITER cannot give an answer to [5]. These facilities will work in parallel with ITER and since they are focused on precise features, they can work on them at conditions that are relevant for DEMO and future power plants.

One very important example is the DTT (Divertor Test Tokamak), that will test possible solutions for the problem of highly energetic plasma interaction with matter. Since this specific aspect is the background of this thesis work, the whole next session is dedicated to this topic.

## Chapter 2

# Plasma-surface interaction and divertor technology

This chapter will deal with the problem of plasma-facing components (PFC) with an increasing level of detail. *Section 2.1* gives a physical introduction of the interactions between plasma and solid matter which will then be exploited to discuss this specific issue in tokamaks, mentioning different approaches to tackle it (§2.2). The approach that now is thought to be the most suitable is the divertor technology, described more extensively in the following section (§2.3). In turn, there exist different strategies that can be adopted as divertors: *Section 2.4* explains arguably the most promising one for future fusion power plants (divertors made of a liquid metal), analyzing specific physical phenomena of this divertor technology.

### 2.1 Physics of plasma-surface interaction

In all laboratory applications, plasma will for sure touch solid materials sooner or later. This is true also for magnetic confinement fusion: the confinement provided by the magnetic field lines is indeed not perfect and it is not even intended to be. The motivation lies in the D-T reaction (1.3a) itself: the produced  ${}^4\text{He}$  ions are fundamental at the beginning, since they are able to heat the plasma, but once they are thermalized with it, they are no longer useful (they do not contribute to the fusion process). On the contrary, these He “ashes” dilute the plasma, lowering the fusion reaction rate and therefore the power produced. Thus, it is needed that they are pumped away and this process is allowed by a flawed confinement. This implies that the plasma will necessarily interact with the plasma chamber or some portions of it. Because of this, it is worth to investigate more in detail what happens in these instances, starting from the physical point of view.

Plasma-material interaction (PMI) involves numerous physical phenomena, which

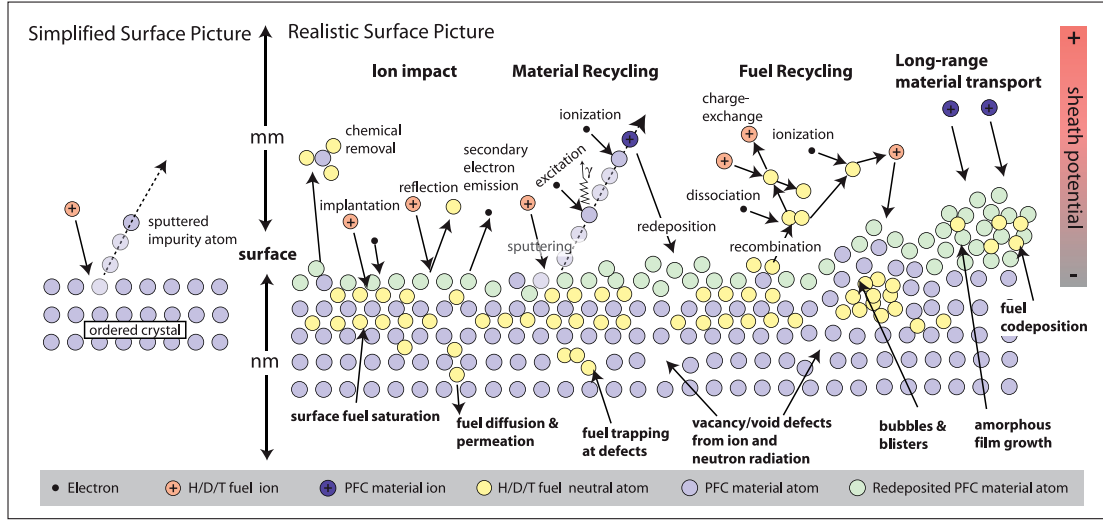


**Figure 2.1:** Schematic illustration of the complex, synergistic and inherently multiscale surface interactions occurring at the material surface in a realistic magnetic fusion plasma environment [20].

have impressive consequences on both the plasma and the surface it is interacting with. Not only PMI has a multi-scale nature, both in time and space, but it must be studied coupling the two interacting states. *Figure 2.1* summarizes all the most important kinds of interaction between a plasma and a solid surface and is a reference for this whole section. Following an introduction about the Debye sheath (§2.1.1), useful because of its crucial role in the physics of PMI, the most relevant phenomena will be explored with greater detail from *Section 2.1.2* on, keeping in mind their respective relevance for MCF.

### 2.1.1 The Debye Sheath

Considering the bulk of a plasma composed by singly charged ions only, the quasi-neutrality condition can be expressed with:  $n_e \approx n_i$ , where  $n_e$  is the electron density and  $n_i$  is the ion density. Inside the plasma, charged particles will move randomly in all directions (if no magnetic field is applied) with a characteristic velocity equal to the thermal one, that scales with  $\sqrt{T/m}$ , and corresponding to a flux  $nv_{\text{th}}$ .  $T_i$  and  $T_e$  can be assumed similar or, as very frequent in plasmas, the electron temperature is much higher than the ion one; instead, the mass of protons and neutrons is  $\approx 2000$  times the electron one and, thus, the electron flux will be much higher with respect to the ion one.

When the plasma is let by itself (i.e. sufficiently far from solid boundaries), the fluxes in the different directions balance themselves, since they are randomly

distributed. Though, in the plasma region very close to the solid interface, there exist only fluxes of plasma particles going toward the solid surface, but none coming from it. Thus, since solids can catch electrons and ions and recombine them, the wall will be charged negatively very quickly because of the much higher electron flux, while the nearest plasma region will have a positive net charge. Hence, while relatively far from the wall there are quasi-neutral conditions, sufficiently close to it an electric field will be established, developing an electrostatic sheath, called the Debye sheath. This electric field will act on electrons with a repelling force, while ions will be accelerated toward the wall. With the hypothesis of no appreciable electric field in the bulk of the plasma, the electric potential  $\phi$  can be considered null, meaning that the wall potential  $\phi_w$  is negative. The magnitude of the potential barrier is self-regulating to maintain ambipolarity, i.e. an equal flux of electrons and ions reaching the walls. The potential cannot be distributed over the entire plasma, due to the Debye shielding phenomenon (§1.3.2): the thickness of the Debye sheath will then be on the order of several  $\lambda_D$  [21]. Since the Debye length can be extremely small with respect to the collision mean-free path, it can be a good approximation to treat the Debye sheath as collision-less.

Making some assumptions it becomes relatively simple to describe Debye sheath in a quantitative way [21]: considering a 1D model, a collision-less sheath with a monotonically decreasing  $\phi$  and all ions entering inside it with the same velocity  $v_0$  (i.e.  $T_i \rightarrow 0$ ), it is possible to retrieve the Bohm sheath criterion, as done in [21]. It states:

$$M^2 \equiv \frac{v_0^2}{T_e/m_i} \geq 1 \quad (2.1)$$

that is to say that ions must enter the sheath region with a velocity greater or equal than the sound speed. Thus, the Debye sheath can now be defined as the region inside which the inequality (2.1) is respected. But since well inside the plasma the ion fluid velocity may be null, there must be a region in which neutrons are pre-accelerated by a decreasing potential and it is called the presheath region.

Even if the sheath can be very small compared with the size of a machine, it is not negligible at all since particles must go through it to hit the wall and it strongly affects the physics of the interaction due to the huge electric field present there. Notably, in edge-plasma models based on the fluid approximation the sheath entrance is often considered as a boundary where to impose suitable conditions, since the dimensions of the sheath do not allow a fluid description of the plasma inside it (§3.1).

Even if up to now no magnetic field has been considered, as mentioned in *Section 1.5*, one of the main methods to produce energy from nuclear fusion is the MCF approach and, in particular, the tokamak is the most developed concept. The

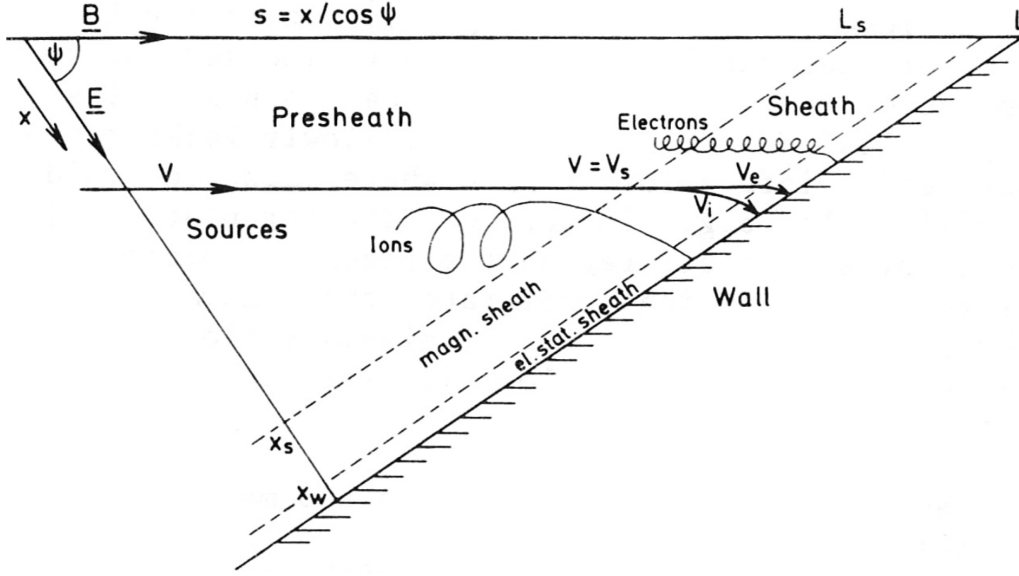


**Figure 2.2:** Simplified view of the presheath and sheath regions when the magnetic field is not perpendicular to the wall [23].

discussion just done would be applicable even if magnetic field lines were orthogonal with respect to the wall, but this is not the case for tokamaks, since the field lines are most of the time almost tangent to the walls [22]. As explained by Chodura [23], the electric field in the presheath region is small and so the motion of charged particles follows the magnetic field lines almost perfectly. If the wall is a sufficiently good conductor, the electric field is orthogonal to the surface and it will have a certain angle  $\psi$  with respect to  $\mathbf{B}$ , as depicted in *Figure 2.2*. The intensity of  $\mathbf{E}$  becomes instead dominant once particles enter the Debye sheath, bending the plasma trajectory toward the direction of the surface normal. A new region between the sheath and the presheath develops in this tokamak-like scenario and it is defined as the magnetic presheath. It is characterized by globally neutral flows and, with considerations similar to those that yielded inequality (2.1), it is possible to find an additional requirement:  $M_{\parallel} \geq 1$ , where  $M_{\parallel}$  is defined as  $M$  but considering, instead of  $v_0$ ,  $v_{0\parallel}$ , the ion velocity in the direction parallel to the magnetic field at the entrance of the magnetic presheath [23].

To describe more quantitatively what happens in the Debye sheath, it is possible to exploit the discussion in [22]. Since in steady-state the target cannot become indefinitely charged unless there is a potential generator, it is possible to assume ambipolarity, meaning that ions and electron fluxes at the wall must be equal. While the ion flux at the wall can be assumed to be equal to the one at the

sheath edge, this is not true for electrons since a considerable fraction of them is reflected back, complicating the calculations. It is nevertheless possible to obtain an estimate for the potential drop across the sheath, employing a Maxwell-Boltzmann distribution of the electrons close to the wall and considering charge neutrality at the sheath entrance:

$$e(\phi_{se} - \phi_w) \approx 3T_e \quad (2.2)$$

where  $\phi_{se}$  and  $\phi_w$  are respectively the electric potential at the sheath edge and at the wall,  $e$  is the elementary charge and  $T_e$  is the electron temperature. This linear relation between temperature and potential difference implies that, if the wall is a very good conductor (so its potential is almost constant) and there is a temperature profile in a direction parallel to the wall, there is an electric field developing inside the plasma along this parallel direction. Hence, if a magnetic field is present, one must account for the presence of an  $\mathbf{E} \times \mathbf{B}$  drift.

### 2.1.2 Physical sputtering

When a particle hits an atom of a solid, it will transfer part of its kinetic energy to it and, if this is greater than the displacement energy (the minimum energy that must be received to permanently displace an atom from its original lattice position), the atom will become a primary knocked-on atom (PKA). In turn, this PKA can collide with other atoms, creating secondary knocked-on atoms and so forth: this sequence of events is a collisional cascade and it is accompanied by a modification of the material structure, due to the formation of defects such as vacancies and interstitials. The amount and typology of damage depend on the kind of impinging particle, on its energy and on the chemical affinity with the solid material [24].

As explained in *Section 2.1.1*, one of the most important physical consequences of the presence of the sheath is that ions are accelerated before reaching the wall, gaining a significant amount of energy. This allows them to produce notable changes in the materials through the collisional cascade mechanism just described. In particular, it is very meaningful when, during the sequences of recoils caused by ion bombardment, some of them are directed backward and intersect the surface with enough energy to escape the solid (*Figure 2.3*): this process is called physical sputtering [24]. The charge of the incident particle is important inasmuch as an ion will be accelerated by the sheath, but once the ion reaches the surface, it is neutralized and the yield is the same for ions and atoms of the same energy impacting the surface. The ejected particles are primarily neutral atoms, atom clusters or molecules [22].

There exists a threshold energy  $E_{th}$  below which no physical sputtering occurs: for

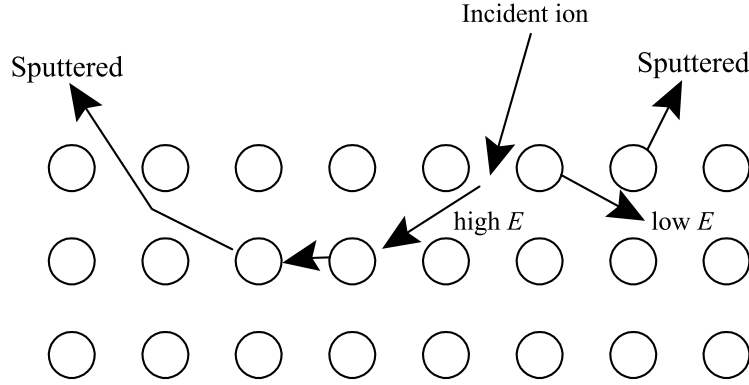


**Figure 2.3:** Schematic illustration of the re-direction momentum from an incident ion to the backward direction, resulting in sputtering [24].

incident light ions (as hydrogen atoms) it can be estimated with

$$E_{\text{th}} \simeq \frac{(M_1 + M_2)^4}{4M_1M_2(M_1 - M_2)^2} E_B \quad (2.3)$$

where  $M_1$  and  $M_2$  are the masses of the incident and target particles, respectively, and  $E_B$  is the measured value of the surface binding energy, which may be considered equal to the sublimation heat (that depends on the surface material) [22]. Sputtering processes are characterized by the sputtering yield  $Y = Y(E_0, \theta)$ , the number of atoms or molecules ejected per unit impacting particle, which is a function of the impact energy  $E_0$  and the impact angle  $\theta$ . While for nearly perfect crystal lattices  $Y$  can change by as much as one order of magnitude with the  $\theta$ , for roughed (practical) surfaces and for relatively small incident angles (up to  $\sim 50^\circ$ ) there is much less dependence on it [25]. To support this, it must be remembered that the sheath region adjacent to the wall surface tends to straighten the ions trajectories, making them approach normal incidence (§2.1.1). Thus, it can be nevertheless worthwhile to evaluate the sputtering yield at normal incidence only: in this respect, Bohdansky formula has a satisfactory agreement with experimental measures [26] and it reads:

$$Y(E_o, \theta = 0) = QS_n(\varepsilon) \left[ 1 - \left( \frac{E_{\text{th}}}{E_o} \right)^{\frac{2}{3}} \right] \left( 1 - \frac{E_{\text{th}}}{E_o} \right)^2 \quad (2.4)$$

where  $Q$  is the “yield factor” (depending on  $E_B$ , and  $M_2/M_1$ ,  $S_n$  is the nuclear stopping cross-section, depending on the reduced energy  $\varepsilon \equiv E_o/E_{TF}$  ( $E_{TF}$  is the Thomas-Fermi energy) [25] and  $E_{\text{th}}$  is the threshold energy introduced before with the approximate expression (2.3). It is possible to notice that, for energies  $E_o$  equal to the threshold one, the yield becomes null, as expected. *Figure 2.4* shows the

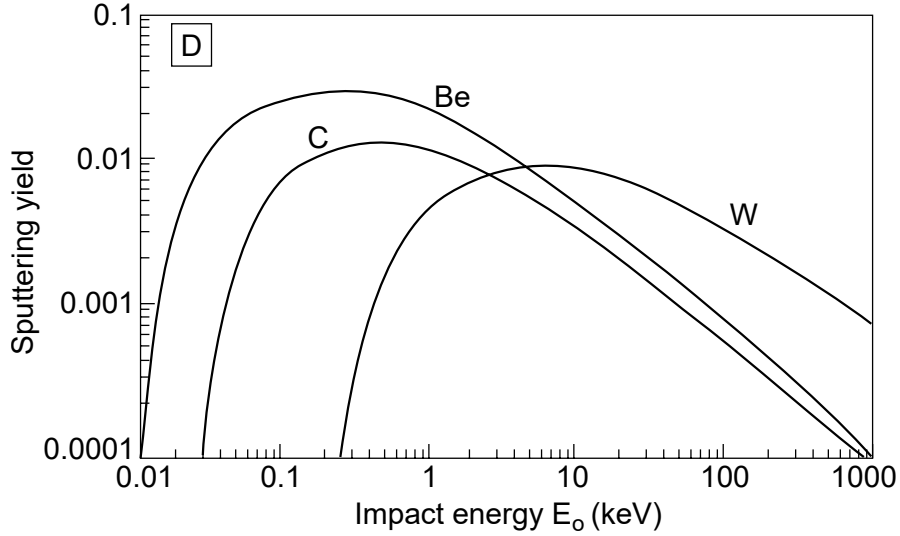


**Figure 2.4:** Normal incidence physical sputtering yields for deuterium ions impinging on Be, C and W surfaces, calculated with the TRIM.SP code [22].

results of  $Y$  calculations with normal incidence performed with the TRIM.SP code (the sputtering version of TRIM, that stands for TRansport of Ion in Matter, a Monte Carlo code) [27]. A couple of interesting things to note are the steepness with which the curve goes to zero for energies close to  $E_{\text{th}}$  and the fact that there is a peak of the curve. This last fact is due to the smaller amount of energy that very energetic ions deposit on the surface layers, since they are able to penetrate much deeper into the lattice. As can be perceived from the estimate of  $E_{\text{th}}$  (2.3) and its role in the evaluation of  $Y$  (2.4), the sputtering yield is strongly dependent on the combination of incident ions and surface materials. Specifically, the estimate for  $E_{\text{th}}$  (2.3) shows how it grows when  $M_2 \gg M_1$ , that is the case for a tungsten surface facing deuterium ions as it can be clearly seen from *Figure 2.4*. On general grounds, it is much more difficult to sputter heavier, high- $Z$  materials when using low- $Z$  ions like deuterium. Of course in (2.3) one must pay attention also to the surface binding energy  $E_B$ : for example, even if carbon is slightly heavier than beryllium (for what concerns the calculation of the coefficient in 2.3), its binding energy is more than twice ( $E_B(\text{Be}) = 3.38$  eV,  $E_B(\text{C}) = 7.4$  eV) and indeed in *Figure 2.4* one can appreciate the carbon higher  $E_{\text{th}}$ .

Atoms that have been sputtered into the plasma, can undergo ionization and come back to the surface following the magnetic field lines (§2.1.3). If energetic enough, they can give rise to self-sputtering and, since momentum transfer between like masses is very effective (the maximum energy fraction that can be transferred is 100%), this process can be particularly damaging [22].

If the surface material consists of an alloy, its element will not have the same physical sputtering yield, in general. The sputter probability per unit depth of the alloying atom  $A$   $p_A(x)$ , function of the depth  $x$  ( $x = 0$  corresponds to the surface), depends also on the kind and energy of the impinging ion and on the surface binding energy of  $A$  [24]. Not only, the sputtering yield for species  $A$  is also affected by its atomic concentration inside the wall  $C_A(x)$  and it can be computed with:

$$Y_A = \int_0^\infty C_A(x)p_A(x)dx \approx \bar{p}_a C_A^s \quad (2.5)$$

where  $\bar{p}_a$  is the average total probability of an atom  $A$  in the surface layer to be sputtered per incident ion and  $C_A^s$  is its average atomic concentration in the same region [24]. The approximation is possible because practically the sputtered atoms come from a shallow layer close to the surface and the contribution falls exponentially with depth, with a decay length on the order of two atomic layers. Thus, the surface layer to compute the averages in (2.5) is of maximum two atomic layers and it is nevertheless weighted toward the first one [24]. In this case it is possible to talk about preferential sputtering, referring to the fact that atoms with the higher  $Y_A$  will suffer a higher sputtering than the others. It is possible to have preferential sputtering even in the case in which the surface material is not an alloy. Indeed, when a significant portion of incident ions has been adsorbed within the wall, their concentration in the surface layer will become significant or even dominant in some instances. Hence, they will be sputtered more efficiently and this will translate into a reduction of the sputtering yield of the wall atoms [28].

### 2.1.3 Thermal and chemical sputtering

The physical sputtering just described is not the only kind of sputtering, which generally identifies all the processes involving atoms ejection from the outer surface layers.

The previously discussed physical sputtering could be well-modeled using classical-mechanics arguments and the binary collision approximation and it was assumed to be independent on small temperature variations. Though, when the wall temperature approaches the melting point, a strong increase in the sputtering yield has been observed for many materials (e.g. lithium [29], beryllium [30], tin [31], tungsten [32]). This kind of sputtering process, called thermal sputtering, is fundamental for plasma-facing surfaces that are in the liquid state and, as it will be clear from *Section 2.4*, it is significant for this thesis work. There are two models to study quantitatively its dependence on temperature: the thermal-spike model and the adatom-evaporation/sublimation mechanism.

Sigmund has been the first to develop the thermal-spike theory [33]. The energy

transferred to the wall material by an incoming ion excites a collective motion of atoms in a region of space, defined as thermal spike volume, where the temperature is increased by the thermal-spike temperature  $T_{\text{spike}}$ , which decays with a time constant  $\tau_{\text{spike}}$ . Because of the collective non-linear interactions of many atoms, this kind of phenomenon cannot be approximated utilizing binary-collisions, as it has been done for thermal sputtering. Initially this model was well established only in the high-energy, heavy-ion bombardment limit, but the model has been extended later on [29] to light and low-energy elements impinging lithium surfaces, since the deposited energy densities during the interactions were fairly similar to the above-mentioned case [28]. According to this, the thermal sputtering employing the thermal spike model is:

$$Y_{\text{spike}}(E_o, T^*) = \frac{\kappa \tau_{\text{spike}} n_2 S_n(E_o)}{\sqrt{\frac{9\pi}{2}} M_2 T^*} \exp\left(-\frac{U^*}{T^*}\right) \quad (2.6)$$

where  $T^* = T + T_{\text{spike}}$  (in energy units),  $U^*$  is the thermodynamic sublimation energy at the melting point,  $S_n$  is the elastic stopping power [34],  $n_2$  and  $M_2$  are the particle density and mass of the wall atoms and  $\kappa$  is a dimensionless number dependent on the incident energy and the mass ratio  $M_2/M_1$  ( $M_1$  is the mass of the impinging ion).  $T_{\text{spike}}$  and  $\tau_{\text{spike}}$  are left as fitting parameters in (2.6) and they are used to follow in the most suitable way the experimental points obtained with 50 eV deuterium incident on liquid lithium (*Figure 2.5*), as described in [28].

The alternative model for thermal sputtering considers the production and consequent evaporation of surface adatoms, which are excited atoms on the surface but without sufficient energy to actually be sputtered [28]. Since excited, adatoms are extremely mobile and therefore they either diffuse across the wall or they sublimate/evaporate. Both of these possibilities have a characteristic time constants, that can be modelled by an Arrhenius-type of behavior [35]. One can write a balance equation for the time rate of change of the areal density of surface adatoms, considering as a source  $\Gamma_i Y_{\text{ad}}$  (the ion flux times the adatom yield, i.e. the average number of adatoms created per incident ion) and from this obtain an expression for the effective thermal sputtering yield due to surface adatoms [28]:

$$Y_{\text{ad}}^s(T) = \frac{Y_{\text{ad}}}{1 + A \exp\left(\frac{E_{\text{eff}}}{T}\right)} \quad (2.7)$$

where  $E_{\text{eff}}$  is the difference between the adatom surface binding energy (smaller than  $U^*$ ) and the activation energy associated with the diffusion to a recombination site and  $A$  is a dimensionless constant.  $Y_{\text{ad}}$ ,  $A$  and  $E_{\text{eff}}$  are again considered fitting parameters against the above-mentioned experimental data and are plotted in *Figure 2.5*. Of course, since the two models are fitted to the same data, their behavior is very close up to the last datum experimental point in terms of Li

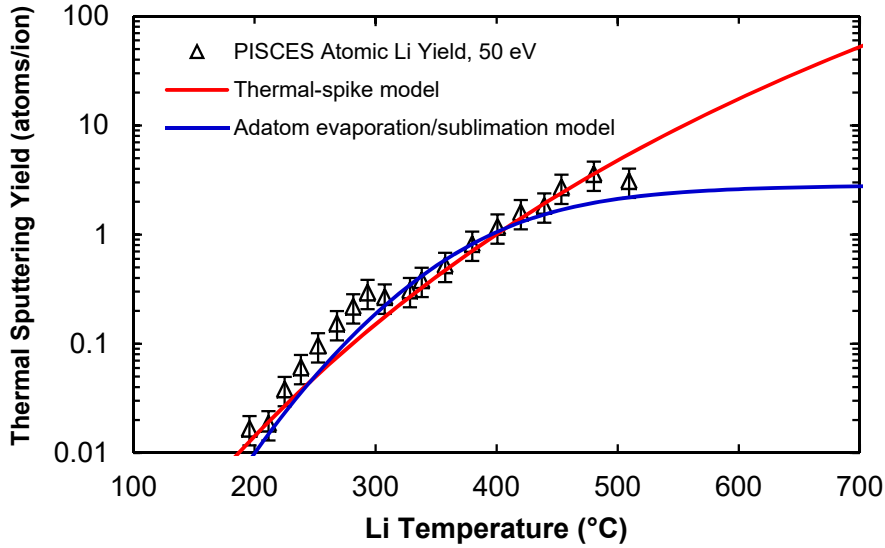


**Figure 2.5:** Measured thermal sputtering yields for 50 eV D→Li bombardment in PISCES-B device as a function of the lithium temperature (triangles) and the correspondingly fitted curves for the thermal-spike and adatom evaporation/sublimation models (red and blue curves, respectively) [28].

temperature. Nevertheless, it can be interesting to compare what happens in the two models after that, for  $T_{\text{Li}} > 500^\circ\text{C}$ : while the thermal-spike yield continues to rise dramatically (remembering that the ordinate is logarithmic), the other model predicts a plateau in the sputtering yield corresponding to the adatom evaporation rate getting limited by their rate of creation [28].

To conclude, one speaks of chemical sputtering when there is the formation of molecules on the wall due to chemical reactions between the incident particles and the surface atoms and these molecules have a binding energy low enough to desorb at the wall temperature [36]. This is of particular relevance talking about H plasmas and carbon surfaces due to hydrocarbons formation: including chemical sputtering in *Figure 2.4*, the curve for carbon would show no energy threshold, meaning that also thermal particles could lead to a significant sputtering. This mechanism is not very significant for this work, so it will not be discussed further.

#### 2.1.4 Retention, recycling and re-deposition

If the surface that is interacting with the plasma is not saturated (e.g. at the beginning of operations), it is capable of absorbing ions and electrons impinging against it. Light and small ions are able to migrate to the bulk of the solid

relatively easily and they can be trapped: this is what is called fuel retention and it is an extremely serious issue when considering a D-T plasma, since the tritium is radioactive (§1.2.2). DEMO, for example, will be designed taking into account a safety criterion which prescribes that the need of evacuation, even in the worst incident scenario, must be avoided [5] and this will strongly impact the tritium cycle of the plant and its storage on-site. For what concerns ITER, instead, the total in-vessel tritium must be limited to 700 g [37].

Since the wall is negatively charged, ions impacting on it are quickly neutralised, recombining with the electrons that, if ambipolarity conditions are verified, come to the wall with the same flux as the ions (§2.1.1). After a relatively short time, the wall gets saturated since there are no more sites able to host the incoming ions. What happens is that they will be emitted as neutral atoms (or as molecules, e.g.  $D_2$ ), to guarantee a null net particle flux at steady-state.

Once ejected from the wall, the particles are not confined anymore by the magnetic field, since neutral. Though, they need to face the incoming plasma flux and they have a significant probability of being firstly dissociated (if molecules) and then ionized again. If this is the case, the newly formed ions are once again confined and they will likely follow the plasma flux impinging on the surface, starting this plasma *recycling* process from the beginning.

Also the surface material undergoes a similar cycle: wall atoms can get thrown out from the wall surface due to physical phenomena like sputtering, as seen in Section 2.1.2 and 2.1.3 and they have to face the incoming plasma flux as well. If they get ionized, they will follow the magnetic field lines and they will likely head toward the wall; there, they are re-deposited on the surface. This process of material recycling, together with the above-mentioned plasma recycling, are well shown in Figure 2.1.

Another related phenomenon is the prompt re-deposition: in this case, the neutral atoms are ionized within several Debye lengths (§1.2.2) from their original locations and they immediately re-deposit on the surface since they cannot escape the sheath potential well [38]. Even if this may seem the same as the material recycling just mentioned, the difference time and spatial scales of the two phenomena play a very significant role and it can be fundamental to distinguish them.

Because of these phenomena, even though the plasma is almost fully ionized before approaching the wall, the neutral (re-)emitted particles ensure that the plasma boundary (the region bordering the wall) can contain a significant fraction of neutral particles, that will play a major role in PMI (§2.4.2).

### 2.1.5 Atomic processes

During both plasma recycling and wall particle emission, the particles can undergo various processes while they are detached from the wall. As already said, molecules can be dissociated into single atoms due to collisions with the incoming plasma particles, but hereafter the focus will be on atomic processes only and deuterium will be taken as a reference to illustrate them.

The most common processes that one can think of are the already-mentioned ionization and recombination processes. In the first case, neutral atoms suffer a loss of an electron due to the impact with an electron from the plasma:



Recombination is instead the dual case: ionized species recombine with an electron close to them:



Ionization and recombination can occur also for other atoms, such as the extracted wall ones or the vacuum impurities inside the machine. What changes is that they have, in general, many more ionized states with respect to deuterium, that has just one. For example tungsten has an atomic number  $Z = 74$ , meaning that it must undergo 74 net ionizations to reach its most charged state starting from neutral conditions.

*Figure 2.6* displays the ionization and recombination rates of hydrogen and helium as a function of electron temperature, for a fixed electron density. In the picture it is possible to distinguish two regions in the graph with different characteristics: for a low enough  $T_e$ , the recombination rate is much higher than the ionization one and the opposite holds for a high enough electron temperature. Thus, in the first case the neutral atom fraction will be much higher with respect to the second one.

Another very important process is charge-exchange (CX). Because of the Debye sheath (§2.1.1), plasma ions travel toward the wall with a high speed (and a consequent high energy) and there is the possibility that they find a neutral atom in their path, which may come either from a recombination or from sputtering/emission of atoms from the wall. Following their interaction, it can happen that they exchange their charge:



where the subscript “fast” have been used to highlight which atom was the one accelerated from the electric potential before the collision and “slow” refers to the neutral atom before the CX, having just thermal energy in general.

Even if the species before and after the interaction are exactly the same, there is a dramatic difference in the products. Indeed, now the very energetic fast atom

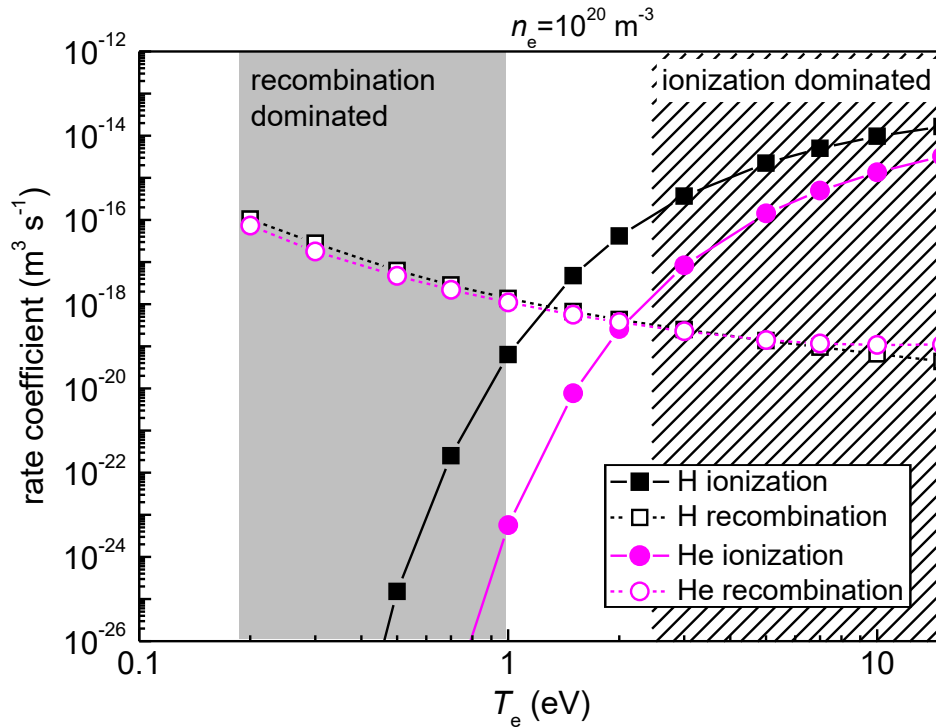


**Figure 2.6:** ADAS library [39] data of ionization and recombination rates of hydrogen and helium for an electron densities  $n_e = 10^{20} \text{ m}^{-3}$  [40].

is not ionized anymore, meaning that it will not follow the magnetic field lines nor feel the electric potential of the sheath. Instead, the once-neutral ion will head toward the wall, but with a much smaller energy with respect to what would have happened without charge-exchange. Thus, CX processes are a very effective momentum sink for the plasma and this has dramatic effects on the power that the wall will receive from the plasma. It goes without saying that this interaction does not happen only for deuterium, but it can happen also between wall atoms or among different species.

If an atom in the plasma is not completely ionized (meaning that not all its electrons have been stripped from the nucleus), it can emit line radiation. This is associated to the excitation and the subsequent very fast de-excitation of one of the remaining electrons of the atom due to the impact with an external electron: for this reason, the more electrons are present in an atom, the higher the probability that this can happen. For example, a tungsten atom that is neutral or singly ionized will emit more line radiation than one with just one electron remaining within its orbitals, because of the different number of electrons available. The net balance of this process is that at the expense of the plasma energy (one of its electrons gives energy

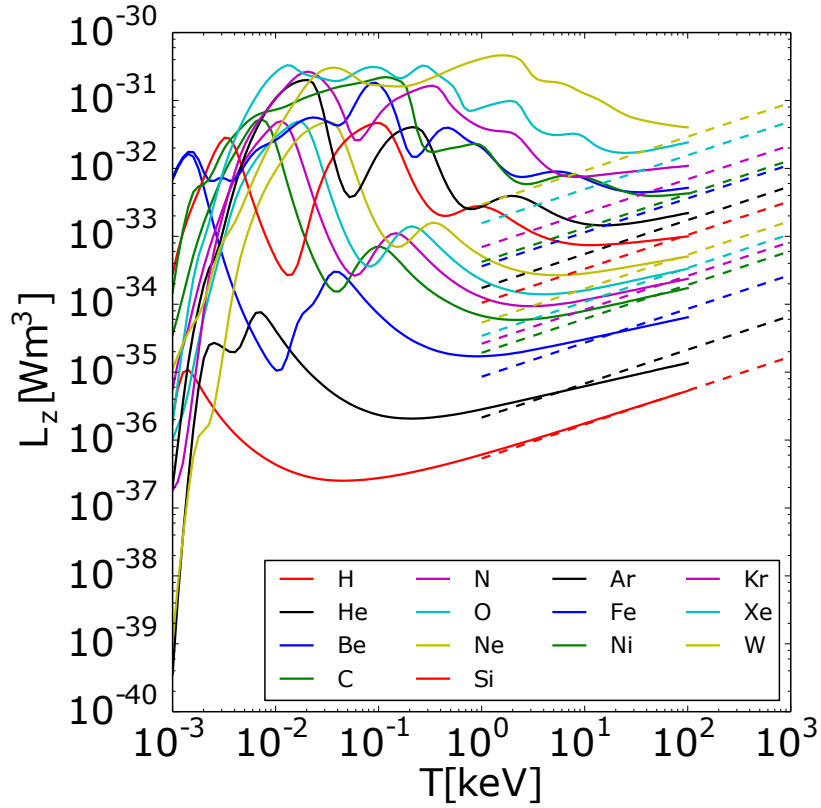


**Figure 2.7:** Loss function data from the ADAS data base (solid lines) [39]. Dashed lines show instead the Bremsstrahlung radiation. Legend ordering (from top to bottom and then from left to right) corresponds to increasing atomic charges  $Z$ . Colours have been used twice in order not to use too similar ones, improving legibility. Elements are recognizable in the graph considering the dashed lines, since the Bremsstrahlung radiation increases with  $Z$ . Thus, for example, the hydrogen is the first red curve starting from the bottom while the silicon is the second one [41].

to the electrons bound to the nucleus) a photon is emitted from the atom, carrying the energy difference between the excited and stable atomic electron states. Another kind of radiation is the Bremsstrahlung one, that is always present in a plasma because of free electrons that change trajectory due to the influence of an external ion nucleus. Bremsstrahlung can occur also for fully stripped ions and its magnitude is particularly significant for high temperatures and for high- $Z$  atoms. To account for the power lost by these radiation mechanisms it is possible, in the most simplified picture, to exploit a loss function  $L_z$ : to compute the radiation power loss one can just multiply  $L_z$  by both electron and atom densities.

*Figure 2.7* highlights that radiation becomes more and more effective as  $Z$  increases, especially at the temperature levels of the plasma core (based on Lawson criterion  $T \approx 10 \div 20$  keV). While the left region of the graph (up to  $\sim 1$  keV) is dominated by line radiation, with curves depending on the charge states distribution and interplay of different phenomena, the right region is dominated by Bremsstrahlung radiation. Indeed, the asymptotic dashed lines account for Bremsstrahlung only, since increasing the temperature all the electrons will be stripped sooner or later, deleting the possibility for line radiation. As the graph displays very clearly, Bremsstrahlung radiation increases with  $Z$  and it scales with the square root of the electron temperature. Moreover, it shows that very heavy atoms such as tungsten are still able to line radiate at plasma core temperatures, entailing an even higher radiation with respect to other elements.

## 2.2 The plasma-material interaction challenge

Having considered the most important physical aspects of PMI, it is now time to investigate their implication on tokamaks from an engineering point of view. As already said (§2.1), almost all plasma applications involve some kind of interaction between plasma and a solid and this process often has very significant effects on both. Indeed, keeping in mind that in MCF the objective is to magnetically confine a sufficiently energetic plasma in order to have an acceptable number of fusion reactions, if due to PMI there are sputtering processes of the solid wall atoms they may reach the plasma core and strongly affect the amount of reactions; on the other hand, the solid walls will consequently be eroded and this can reduce the lifetime of the components.

Theoretically, it is possible to perfectly align the magnetic field in such a way to make it tangential to the plasma vessel at every point. If this was the case, the plasma would reach the walls only by purely cross-field motion, that can be reduced by different orders of magnitude with respect to thermal motion, depending on the strength of the magnetic field (§1.5.1). Though, in practice it is impossible to achieve such a precision. In the direction parallel to the magnetic field lines, particles are not affected by it and they move with very high speeds, typically thermal ones. Hence, in the case of a misalignment, charged particles will reach the wall by parallel motion, meaning that they will be much more energetic and sputtering and erosion phenomena are enhanced. The particles present in the plasma chamber other than those related to fusion reactions are called impurities and they not only are useless to produce the wanted fusion reactions, but they also cause issues diluting the plasma and they are involved in the process of radiation emission: because of this it is of paramount importance to control their amount. Due to these aspects, it is fundamental to investigate PMI, understanding the

orders of magnitude of the key parameters at play (§2.2.1) and evaluating currently adopted (§2.2.2-2.3) and future solutions §2.4) to tackle this issue.

### 2.2.1 The power exhaust challenge

During the operation of a fusion power plant, the plasma should be heated by the alpha particles produced by D-T reactions, that are confined by the magnetic field lines and allow the plasma to be sufficiently hot to keep having fusion reactions (§1.4.1). Though, considering a simple 0D and steady-state energy balance of the chamber hosting the plasma, the power that is being generated in this way must be dissipated in some way. There are three channels available as energy sinks and they are radiation (emission of electromagnetic waves), conduction (microscopic flux of heat without necessarily a flux of mass) or advection (flux of energy related to a macroscopic transport of mass):

$$P_\alpha = P_{\text{rad}} + P_{\text{cond}} + P_{\text{adv}} \quad (2.11)$$

There are profound differences among these mechanisms and one of the most important is that radiation is almost isotropic, since it propagates with almost equal probability in all directions, while the other two channels are not. Conduction and advection are related to particle motion, which is bounded to the magnetic field lines: the heat flux will be much higher in the direction along  $\mathbf{B}$ . This implies that the wetted area for  $P_{\text{cond}}$  and  $P_{\text{adv}}$  will be much smaller than the one dedicated to radiation, implying a much larger heat flux on the surfaces in the case of an even sharing of power between isotropic and anisotropic sinks.

The radiation mechanisms are those already seen in *Section 2.1.5*: line radiation and Bremsstrahlung. While a 0D equation can be useful to have some orders of magnitude of the quantities at play, close attention must be paid evaluating whether radiation is beneficial or not. Indeed, from (2.11) one could say that the more power goes in the isotropic channel the better, since it is possible to face it with a larger area. Though, it is fundamental to understand where exactly the radiation is coming from: if it is occurring in a region where we would like to keep the plasma hot, like the core plasma, it is absolutely harmful since it is turning off the fusion reactions (even if it is positive from the power exhaust perspective). On the contrary, if the radiation is coming from the boundary of the plasma, that is significantly colder than the core one (and thus has already a comparatively small amount of fusion reactions) it is highly beneficial since the heat is being rerouted to a preferred heat sink mechanism, reducing the power that is going to the anisotropic channel.

For what concerns the magnitude of radiation emission, they strongly depend on the particles present in the plasma. Indeed, Bremsstrahlung and line radiation depend respectively on  $Z$  and on the number of electrons remaining on an atom

(which is again related in a more or less complex way to  $Z$ ) and they are orders of magnitude bigger for potential sputtered atoms from solid walls than for those of the main plasma (*Figure 2.7*).

### 2.2.2 Engineering solutions

The characteristics of the components that are facing directly the plasma inside the vacuum chamber (the so-called Plasma-Facing Components, PFCs) are essential to attain nuclear fusion, since they will strongly affect the plasma and could potentially lead to the impossibility of operating a tokamak. They suffer very high particle and energy loads, but they must maintain their operational functionality during their lifetime. In order to ameliorate the effects of PMI, a possible engineering strategy is to let the plasma impinge on solid walls only on a defined portion of space.

Historically, the first approach is to adopt a limiter, which simply consists of a protrusion of the PFC inside the plasma, sacrificing in order to protect the rest of the first wall (FW, the wall of the plasma chamber in direct contact with the plasma). The magnetic configuration as described in *Section 1.5.1* creates ergodic surfaces called magnetic surfaces, which are concentric torus always tangent to the magnetic field lines. As displayed in *Figure 2.8*, in the case of a bare FW or in a limiter configuration, it is possible to identify the only magnetic surface that is exactly tangent to the FW/limiter and it is called the last closed magnetic flux surface (LCFS) or separatrix, referring to the fact that the magnetic surfaces outside it cannot close without touching the wall. Thus, the separatrix separates two plasma regions very different in nature: the main plasma inside the LCFS and the scrape-off layer (SOL) outside it. The reason for this name lies in the fact that a charged particle following a magnetic field line in the SOL sooner or later will hit the wall, being “scraped-off” due to the solid surface. Because of this, the plasma properties in the SOL region are those that eventually impact the PMI. The limiter approach is arguably the most straightforward approach to tackle the PMI issues but it is evident how the impurity source (the solid surface) is extremely close to the plasma core and, in the light of what said in *Section 2.2.1*, the reason why this is an issue. Indeed, impurities can easily reach the region of the plasma that should be as “clean” as possible and they are able to turn off the fusion reactions because of radiation emission if their concentration is sufficiently high.

Once understood that this is due to the fact that the separatrix is defined by mechanical contact, it is reasonable to think of an alternative and a very successful one has been the divertor configuration, which determines the LCFS magnetically.

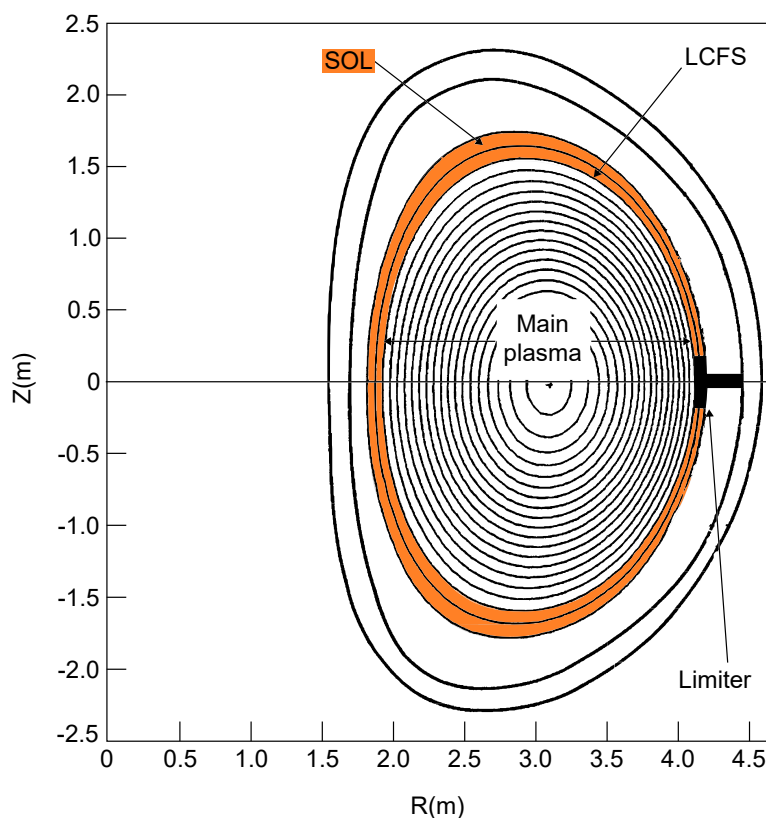


**Figure 2.8:** A JET-size plasma in the limiter configuration. The LCFS is defined by the leading edge of the limiter [22].

## 2.3 The divertor technology

### 2.3.1 Divertor physics

The main advantage of the divertor is, as opposed to the limiter, that it can take the interaction between the plasma and the wall as far as possible from the core region. Since in a tokamak there is a plasma current that flows toroidally in order to create a poloidal component of the magnetic field (§1.5.1), there is the possibility to add a poloidal field coil that works as a divertor coil. Indeed, by carrying the current in the same direction as the plasma one, there will be a point in between the plasma and the divertor coil where the two poloidal magnetic field created in this way exactly cancel out and it is called X-point. If there is only one point where the poloidal component of the magnetic field  $B_\theta = 0$ , it constitutes a single-null configuration which is the one depicted in *Figure 2.9*. The benefit is that the LCFS is now defined by the null-point and the magnetic field lines in the SOL are diverted away from the core plasma down to specific solid components called

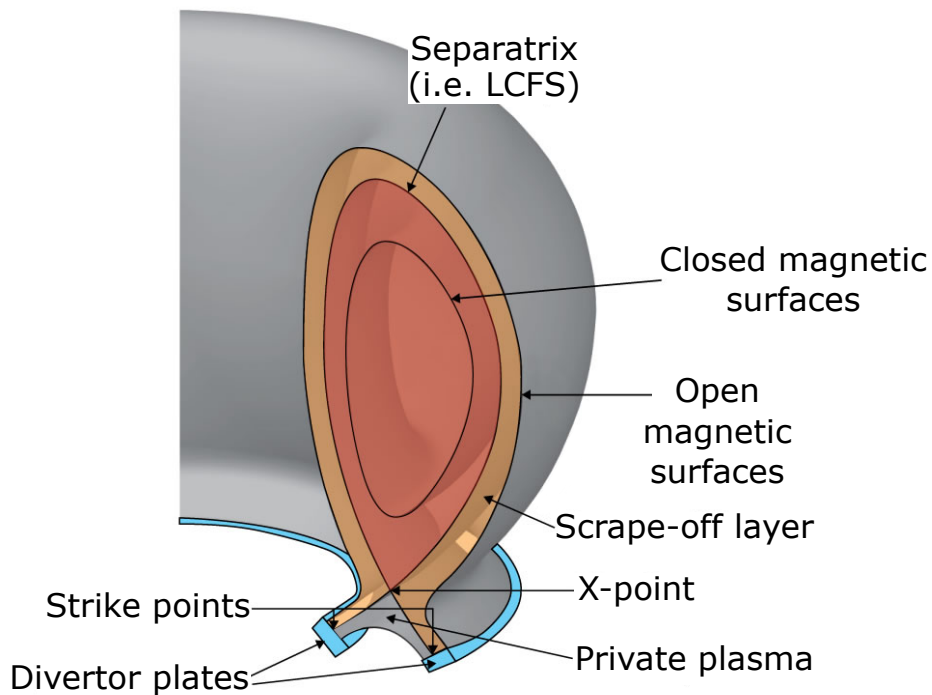


**Figure 2.9:** Sketch of the tokamak divertor configuration with a single X-point (which has been the most used one up to now). Field lines in the scrape-off layer (in orange) are directed downward to the divertor plates thanks to an external magnetic field [42].

divertor plates, that take care of the control of PMI. In this way, even if sputtering and erosion processes will occur nevertheless, resulting particles have to travel a much longer distance before reaching the core plasma with respect to the limiter approach. Moreover, wall atoms will encounter a plasma flowing at high speed toward the region where they have been ejected and this will make going upstream even more difficult.

Furthermore, since the particles are more easily confined in a region not close to the plasma core, impurity effects can end up being really desired. Indeed, on the condition that the impurity concentration is never high enough to be able to reach the core very easily, causing a significant amount of radiation there, the more the impurities in the divertor region the better. Indeed, despite impurity presence is not wanted in the plasma core, it is extremely helpful in the SOL plasma: they can re-route a fraction of power that would flow to the target through advection/convection mechanisms to the radiation channel, that is almost isotropic and thus limits the heat flux the divertor plates must endure.

Not only, but thanks to phenomena like CX (§2.1.5), the plasma loses a significant amount of momentum before reaching the solid walls. If through radiation the SOL electron temperature is reduced to  $T_e < 5$  eV before reaching the target plate, CX will become predominant and this allows the attainment of the plasma detachment, meaning that the divertor target will be almost isolated from the main plasma and the heat flux is strongly reduced [22]. This is extremely attractive and both ITER and DEMO are expected to operate in a partial detachment regime, meaning that the detachment will not occur along the whole target but at least the strike point (where the separatrix encounters the divertor plates, which is the most solicited and critical region) must be detached [5].

This rationale explains the success of the divertor and why it is considered the most promising solution to face the power exhaust issue [5]. Nevertheless, limiters are still important since they are needed during the time interval for plasma current to appear and to produce the X-point, providing protection.

### 2.3.2 Cross-field diffusion in the SOL

As said different times, charged particles follow the magnetic field lines with a circular motion perpendicular to them and being free along them. Nonetheless, this idealized situation is not true anymore when one considers many particles: because of collisions and difference of concentration there is a cross-field diffusion process, going toward the region with the lowest concentration, from the plasma core to the boundary. This means that particles can cross the separatrix and they will move from the core to the SOL and, once there, two processes are in competition: diffusion in the radial direction, typically very slow, and the very fast movement along the magnetic field lines. Because of this difference in speed, it can be expected that particles will head toward the solid surface much before they manage to diffuse across the magnetic field lines by a relatively significant length. If this is the case, then the SOL region inside the plasma chamber is not completely filled with plasma, but just a tiny portion very close to the separatrix still has a meaningful particles concentration. To evaluate this in more quantitative terms it is possible to estimate the density SOL thickness (characteristic density decay length starting from the separatrix and moving radially in a poloidal cross section) with simple arguments (e.g. straightening of the SOL) obtaining a density SOL thickness  $\lambda_n \sim 1 \div 10$  mm [22]. Of course this value is strongly dependent on the properties of the tokamak under consideration and one of the most important parameters is the connection length  $L$ , that is the distance, following magnetic field lines, between the two surfaces that delimits them in the SOL region. It is possible to define different kinds of  $\lambda$ , evaluating for example the temperature ( $\lambda_T$ ) and the heat flux ( $\lambda_q$ ) decay instead of the density one.

Apart from this simplified analytical estimate, it is also possible to exploit fundamental physical arguments [43] or empirical models based on experiments like the multi-machine database fit [44]. In such ways one can obtain a power law dependence of  $\lambda_q$  on different parameters (e.g. the toroidal magnetic field, the magnetic axis major radius and the plasma current). In particular, bigger and bigger machines will imply a decreasing characteristic length: making some extrapolations (that of course must be handled gingerly), predicted values for ITER are  $\lambda_q \sim 1$  mm, while for DEMO it will be for sure smaller than that.

This parameter is fundamental to estimate the area that will be invested by the plasma particles: even if, for example, the divertor plates are meters long in the poloidal direction, the wetted area will be extremely small in comparison, since its width will be on the order of the SOL thickness. With such a small wetted area to face the power coming from the SOL, dramatic consequences can be expected. The maximum steady-state power flux permitted at ITER divertor targets are  $\sim 10$  MW/m<sup>2</sup> while DEMO, since it will produce much more thermal power but it will not have a correspondingly higher wetted area (that is nevertheless increased even with a smaller  $\lambda_q$ , since the overall size of the reactor is bigger), will certainly have much more demanding (if unmitigated) heat fluxes, even approaching  $\sim 100$  MW/m<sup>2</sup> [45]. Just to put things in perspective, the aeroshell of Stardust, the robotic space probe launched by NASA in 1999, was the fastest man-made object ever to re-enter Earth's atmosphere at 12.4 km/s and its heat shield was made to withstand a nominal peak heat flux of  $\approx 12$  MW/m<sup>2</sup> [46].

### 2.3.3 Future divertor solutions

Since ITER is already exploiting state-of-the-art power dissipation technologies, alternative approaches must be adopted for the leap to DEMO or future power plants and the main ones can be summarized in the following:

- impurity seeding: impurities are injected on purpose on the region very close to the divertor, in such a way to dissipate part of the power in the form of radiation before it reaches the target. Of course, for this idea to work the impurities must be confined to the boundary of the plasma, where radiation effect is beneficial: to do this a huge focus must be put on the location and injection strategies;
- advanced divertor configurations: the main possibilities are with a higher order poloidal magnetic field null (i.e. more than one X-point) or with a very long outer divertor leg (Super-X divertor). Both of them entail an expansion of the magnetic flux and a broadening of the wetted area, meaning that it is possible to significantly reduce the heat flux, other conditions being equal. The problem

is that to achieve such configurations it is needed that the superconducting coils (which work as perfect conductors at very low temperatures) are much closer to the relatively hot plasma, that is also a source of highly energetic neutrons able to easily induce modifications on materials. Moreover, the additional shielding needed for the coils and the large fraction of the vacuum chamber occupied by the divertor affects the size of the machine and consequently the investment cost: with equal power generated they will both increase.

- alternative PFCs, among which liquid metal divertors (LMD) are the most promising: this kind of technology takes advantage of latent heat and in principle it would be able to exhaust much higher power with respect to solid ones. This constitutes the specific framework of this thesis work and it is hence discussed more in detail in *Section 2.4*.

Up to today, the integration and reactor relevance of these solution is still to be fully confirmed. To this purpose, since the extrapolation from the present devices (largely the medium-sized tokamaks) or ITER to DEMO based on modelling alone is considered too large, involvement of dedicated facilities is necessary [5]. In this respect, DTT (§1.5.3) is a tokamak that will be built in Frascati, Italy with the main purpose of investigate different solutions for the plasma exhaust problem in the conditions relevant for DEMO or future power plant.

A mean to study the very specific physics of PMI are the Linear Plasma Devices (LPDs): they can be used to simulate the divertor environment of fusion reactors but without the complexity of the toroidal geometry. Even if this means that they are by no way sufficient for the transition to DEMO and their results have to be evaluated sooner or later in an advanced tokamak environment (e.g. DTT), they can be of great help to better investigate PMI phenomena since they allow for easy diagnostic access and reproducible conditions [47]. This is particularly true for the comparison between solid and LMDs in terms of power handling capabilities [40].

### 2.3.4 Importance of linear plasma devices

Linear plasma devices have been recently used in order to reach ITER divertor-like conditions of density, temperature, particle and heat flux, which could not be done in current tokamaks. One of the most important LPDs in Europe is Magnum-PSI (Magnetized plasma Generator and NUMerical modeling for Plasma Surface Interactions), which is the main research facility in the DIFFER (Dutch Institute For Fundamental Energy Research) PMI lab. Plasma is produced by a cascaded arc source and it is then guided to the target by a superconducting magnet; a multitude of diagnostics is employed to analyse the plasma and the wall material during and after exposure [48]. This LPD is designed to study PMI physics in the strongly-coupled regime, meaning that the mean free path of eroded particles is

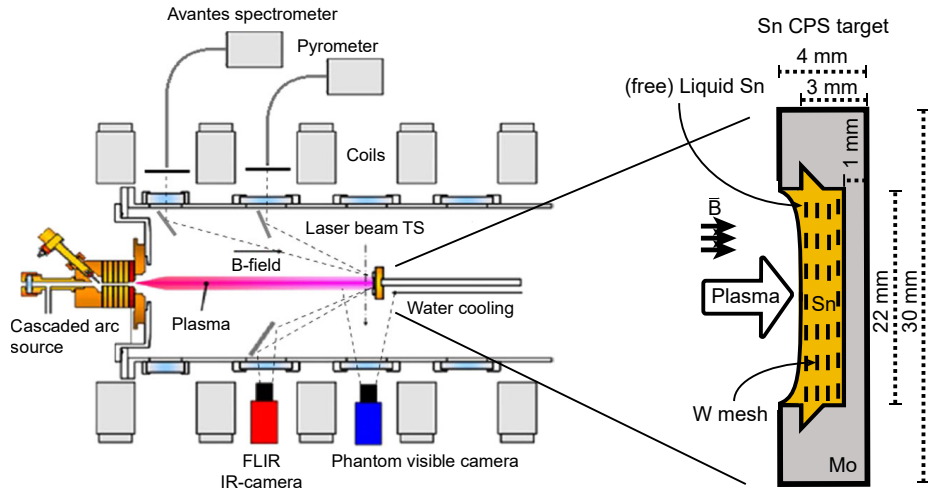


**Figure 2.10:** Schematic drawing of Pilot-PSI and of a LM sample design [49].

smaller than the plasma-beam size and hence they are trapped in the near-surface plasma [40].

The predecessor of Magnum-PSI is Pilot-PSI: it is a smaller device with a lower maximum magnetic field strength and with a higher neutral fraction at the target. Its schematic overview including the position of the main diagnostic is shown in *Figure 2.10*; together with it, a schematic drawing of a LM target is highlighted (§2.4). Of course, experiments performed in such devices can not answer questions concerning the behavior of the core plasma following the LM divertor exposure, but it is possible to retrieve significant information concerning the target point of view, what it undergoes when it has to face a reactor-relevant SOL plasma.

Both these devices have been used to investigate the phenomena involved when a LM target face the plasma at DEMO-relevant SOL plasma fluxes and the main experiments will be summarized in *Section 2.4*.

## 2.4 Liquid metal divertors

The employment of LMDs is the most promising technique to tackle the issue of power exhaust adopting alternative PFCs. When such a target is exposed to the SOL plasma, the power load will vaporize the metal and a vapor layer will be formed in front of the target: being it strongly irradiating and taking advantage of the latent heat of evaporation, it can resist much higher power fluxes. After having analyzed more in detail why it could be worth to exploit a LM technology for future fusion power plants with respect to the standard solid ones (§2.4.1), a brief introduction of the vapour shielding phenomenon is made (§2.4.2). *Sections*

2.4.3 and 2.4.4 will respectively analyze the possibilities regarding the choice of the specific metal to be used and of the concept of LMD to be adopted. Finally, Section 2.4.5 gives some conclusive remarks on the LM technology and its investigation through the employment of LPDs, which is the very specific framework of this thesis work and will serve as a motivation for the modelling work performed.

### 2.4.1 Solid vs LM divertors

The problem of the power exhaust is one of the main challenges toward nuclear fusion energy production and up to now it has been tackled at first with limiters and then with solid divertors. ITER will have as well a solid divertor made of tungsten, which can still be possible due to the limited power produced in the reactor with respect to a future fusion power plant. Though, when considering the jump between ITER and DEMO it must be taken into account that the fusion power generated and the wall neutron load will increase by roughly an order of magnitude [50], implying the need of strategies to limit the power fraction reaching the divertor (and with a much smaller margin of error as well) and a stronger resistance against neutron damage.

Tungsten is the material chosen for ITER divertor because of several advantageous properties, such as a high thermal conductivity and melting point, a low tritium retention and solubility, a low sputtering rate and high strength [51]. However, solid materials (like tungsten) suffer of two main problems:

- they are susceptible to thermal shocks and to fatigue which could lead to macroscopic cracking;
- they suffer of erosion issue (even in the case of low sputtering yield) since the erosion rate and the expected lifetime set a minimum thickness, that has to be compliant with the heat load that can be conducted through the material. If this heat load threshold is overcome, the solid will start melting.

These consequences get even worse when transient or off-normal events are considered: any large edge-localised mode (ELM) or disruption (which are transient instabilities of the plasma that increase a lot the heat flux on PFCs) that are not mitigated could lead to component failure. The main concern is that, in the case a replacement is needed, it could require several months, preventing the tokamak from operating in that period which causes a loss of money and the delay of the results needed that in turn reduce the competitiveness and reliability of eventual power plants.

Divertors made of liquid metals are very attractive to ameliorate these issues and this is why their investigation has been pursued. LM are already molten and so

they cannot suffer from melting problems; not only, but thanks to this they are also self-replenishing, meaning that they can resupply by themselves the eroded areas of the component without having a net material loss over time, giving the possibility to make the divertor thinner, thus leading to an improved power handling due to the lower thermal resistance, and eliminating the problem of the lifetime of the divertor. Exploiting LMs it is also possible to decouple the PMI issue from the neutronic one: since the LM suffers less from neutronic damage (no defect creation), it will deal with the heat flux and it has some advantages in doing so since it is already molten and it can not crack; in this way, since the structural material that hosts the LM is protected by it, it can be designed to better withstand the neutron flux, possibly even selecting a different material with respect to the solid option. Moreover, not only there are already LMD designs that have been estimated to be able to exhaust steady-state power levels up to 20-25 MW/m<sup>2</sup> [52], but they are more resilient to transient and off-normal events with respect to a solid divertor. These last advantages related to power dissipation can be explained thanks to the exploitation of latent heat and considering the physical phenomenon of vapour shielding, discussed more in detail in the following (§2.4.2).

### 2.4.2 Vapour shielding

Because of the heat flux reaching the target it is possible to change its state as a consequence: solid divertors may melt locally, while LM can evaporate. Due to evaporation and other phenomena like sputtering, the metal vapour density in front of the target increases (up to a critical density), forming the so-called vapour cloud, and therefore the interactions described in *Section 2.1.5* become more and more numerous. Indeed, the neutral cloud “absorbs” a fraction of the plasma power by ionization and excitation of LM atoms, by radiation processes (that reducing the heat flux at the target since it is almost isotropic), by charge-exchange processes and mass transport loss. At this point, the plasma is strongly cooled and it undergoes a significant recombination of ions and electrons into neutral plasma particles, which in turn enhance the above-mentioned atomic processes (the density of neutral particles is increasing), starting a positive feedback loop. These are the first four steps of the vapour shielding loop, fully depicted in *Figure 2.11*.

Exploiting the vapour shielding principle, off-normal loads could lead to a stronger LM evaporation that in turn would provide a better shielding to the target surface for what regards the heat load while, on the other hand, there will not be an erosion problem from the target point of view, since the LM can be self-replenished. Therefore, in these accidental cases, a LM PFC can exploit a self-protecting negative feedback mechanism with respect to the heat load coming from the plasma: the larger the heat flux, the more LM will evaporate from the surface and the stronger the shielding effect of the vapour cloud.

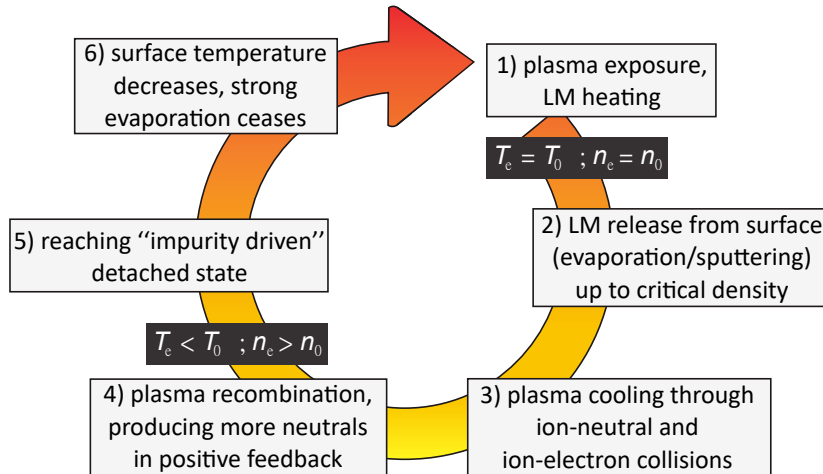


**Figure 2.11:** Time-cycle of dynamical vapour shielding: the boxes indicate the different phases during each cycle [40].

These theoretical reasoning have been experimentally demonstrated in several studies (e.g. [53], [54], [49]). Specifically, [54] showed how the vapour shielding is able to reduce the steady-state temperature of the LM (Sn in this case) compared to a conduction-based model that does not account for it (*Figure 2.12*). This experiment was performed in Pilot-PSI, exploiting as a target the one depicted schematically in *Figure 2.10*: a 3-mm-deep molybdenum cup contains the tin that is held secured by a tungsten mesh (this target design, together with other possibilities, is briefly discussed in *Section 2.4.4*). The comparison of the power handling capabilities is made against the solid molybdenum, exposed to similar plasma and target cooling conditions. *Figure 2.12* compares the temperature evolution at the center of the target of the liquid tin and the solid molybdenum when they are exposed to a heat flux of  $q_{\text{ref}} = 16 \text{ MW/m}^2$ . For both the materials there are two lines: the solid one represents the experiments, while the dashed one is the solution of a 3D finite-element simulation that takes into account only conduction-based cooling. From the graph it is possible to claim that LM steady-state temperature is reached in  $\sim 0.5 \text{ s}$  and that it does not follow a conduction-based cooling curve (according to which temperature increases following Newton's law of cooling until the conducted heat is equal to the received one from the plasma). Moreover, in the experimental results there is a reduction of  $\sim 700 \text{ K}$  in comparison with the model: this indicates the presence of additional heat dissipation channels for the liquid with respect to the solid, whose experimental and simulation curves are much closer. The same study [54] also collected the central surface temperature at the end of the plasma discharges (20 s) for both sample typologies for different values of  $q_{\text{ref}}$  (*Figure 2.13*). It is remarkable to acknowledge that the liquid tin

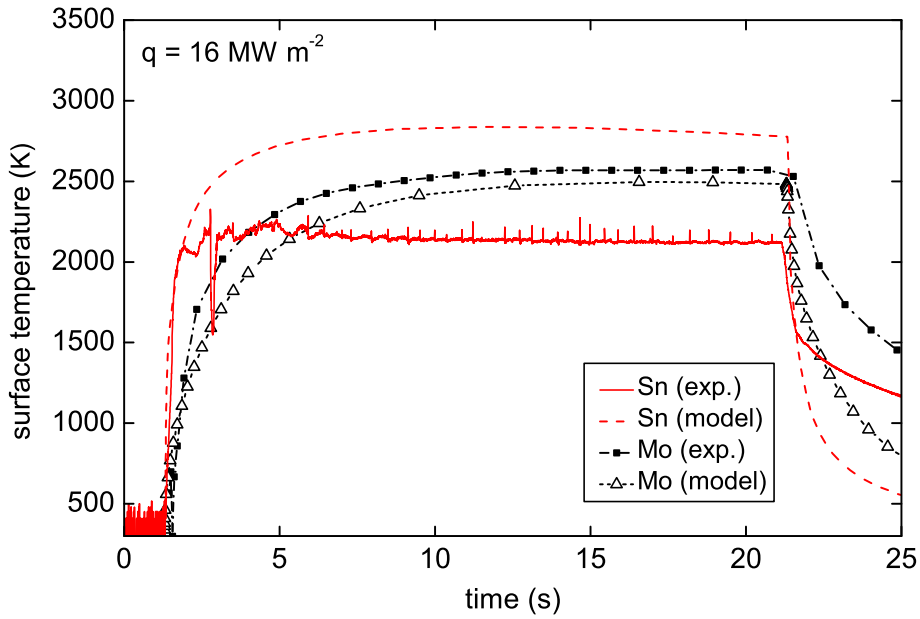


**Figure 2.12:** A comparison between experiment and ANSYS simulations of the central surface temperature evolution of liquid Sn and solid Mo for  $q_{\text{ref}} = 16 \text{ MW/m}^2$ . Due to vapour shielding, the steady-state Sn temperature reduces significantly compared to the conduction-based model that does not consider it. [54].

surface temperature is almost completely decoupled from the applied heat flux, while the solid molybdenum one grows almost linearly (the dashed lines are just to guide the eye, they are not fit curves of the experimental points). This is possible thanks to the above-mentioned feedback loop that establishes a self-regulated heat flux mitigation mechanism. Another very interesting insight is the fact that the data point for Mo at  $q_{\text{ref}} = 22 \text{ MW/m}^2$  represents the temperature after just 5 s (instead of 20 s), since the discharge has been stopped to avoid target melting. For what has been said so far, thanks to the vapour shielding phenomenon the superiority of LM against solid materials when it comes to facing a high plasma heat flux is self-explanatory.

An additional aspect to be analyzed is the intrinsic behavior of the vapour cloud, that has an oscillatory and cyclical nature. Indeed, when the vapour cloud is so dense that it can start a positive feedback of plasma recombinations, the plasma is very likely to be detached from the surface shortly after. When this occurs, the heat flux reaching the target suddenly drops and the surface temperature follows, implying a reduced (or even ceased) LM evaporation. Though, if this happens, the vapour cloud density starts to decrease as well, since its source is almost disappeared but particles are nevertheless lost (charged particles can diffuse

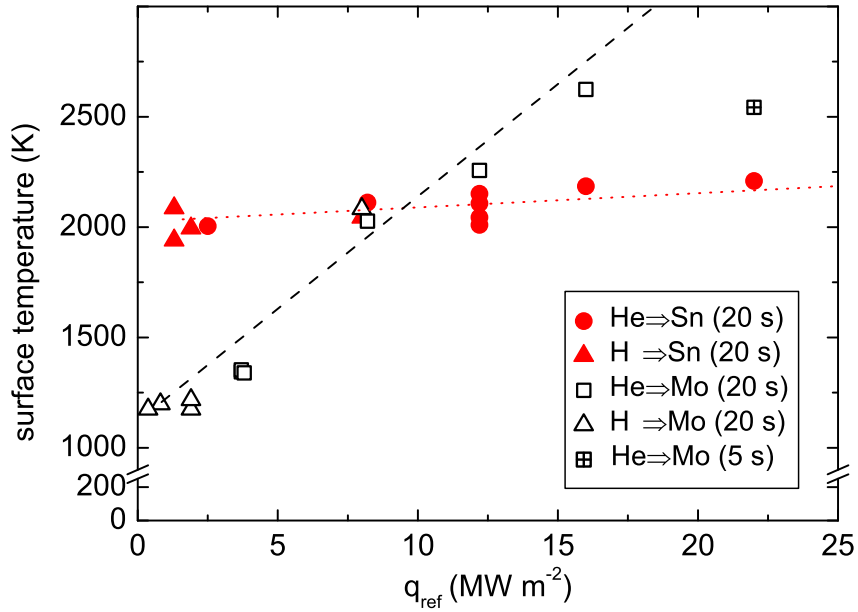


**Figure 2.13:** Temperature of the target surface center after 20 s of plasma exposure for liquid Sn and solid Mo. The lines are drawn to guide the eye. The surface temperature of liquid Sn is almost independent of  $q_{\text{ref}}$  in the given parameter space. The data point for Mo at 22 MW/m<sup>2</sup> had a 5 s shot duration to prevent melting the target. [54].

across the magnetic field, while neutral ones are not even confined). Once it reaches a very low density, the plasma re-attaches to the target surface, increasing the LM evaporation anew and starting the cycle from the beginning. The full vapour shielding cycle is shown in *Figure 2.11*.

This periodical behavior can be noticed in the “steady-state” part of the tin curve in *Figure 2.12*: the oscillations of surface temperature have an amplitude up to 200 K and a period on the order of hundreds of ms. A very specific study on the analysis of this oscillatory behavior was made by van Eden et al. in 2017 [49], exploiting the experimental setup depicted schematically in *Figure 2.10*. *Figure 2.14* highlights one of the periods in terms of different parameters, such as the surface temperature at the target center (a) and edge (b), the line-integrated intensity of neutral Sn emission  $\Sigma I_{\text{Sn}0}$  at 452.5 nm observed using a fast camera (c), suitable for qualitative investigation of the neutral Sn density, the typical axial penetration length of evaporated Sn neutrals  $d_{\text{ax}}$  (d) and the typical width of the vapour cloud  $d_{\text{width}}$  (e). Within a single period it is possible to qualitatively distinguish three phases. In the first phase all the parameters increase: the plasma is starting to heat the LM, which evaporates more and increases the density and the size of the vapour cloud in front of the target. During the second phase, the

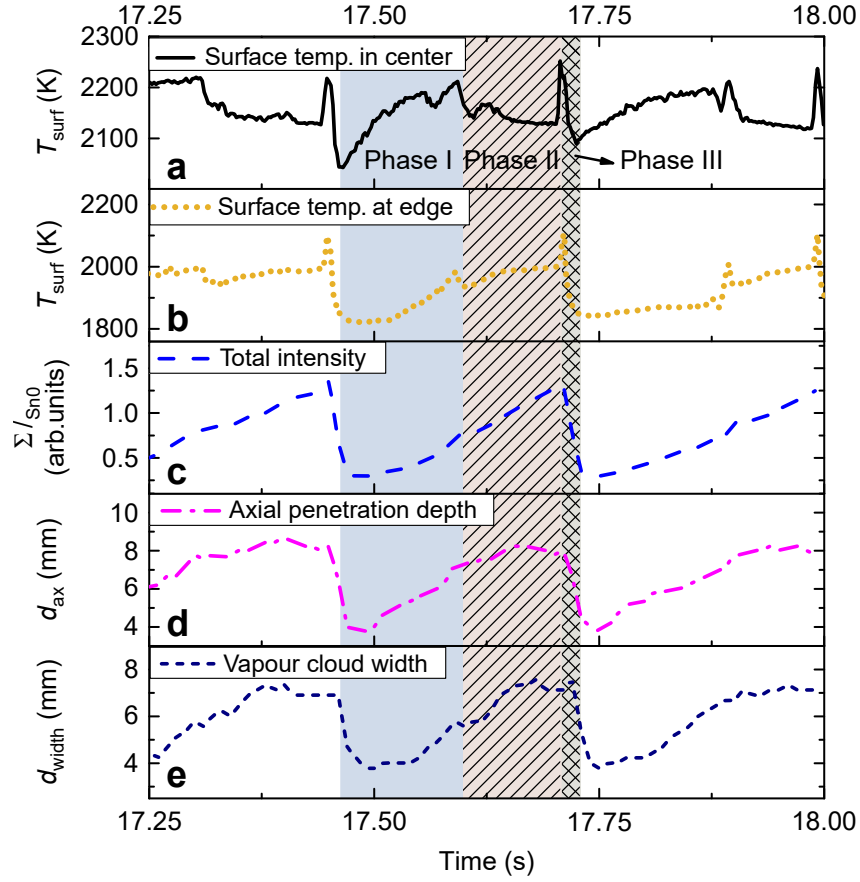


**Figure 2.14:** Vapour shielding dynamics. Value of the surface temperature at the target centre (a) and edge (b) and Sn emission (c–e) between 17.25 and 18 seconds after initiating a  $22.0 \text{ MW/m}^2$  He discharge. Three characteristic phases within a typical oscillation period are indicated by the roman numerals I–III and are highlighted by different motifs. (c), (d) and (e) show, respectively, the total line-integrated intensity at 425.5 nm, the penetration into the upstream plasma and the radial extent of the vapour cloud [49].

central surface temperature starts to decrease, while all the other parameters keep rising: this results in a flattened radial surface temperature distribution at the end of phase II with respect to phase I. Finally, in the third phase there is a sharp increase of the surface temperature that is followed by a sudden drop that defines the end of the cycle. The emission profile and vapour cloud size do not have an abrupt rise, but they nevertheless undergo a drop in phase III. Actually, since such a transient additional heat flux is highly unlikely and such rapid heating/cooling is unphysical, the sudden temperature rise is thought to be due to a change in emissivity of the surface that alters the reading of the IR camera.

To conclude, the oscillations are induced by a detachment-like phenomenon of the plasma and differences in timescales between thermal equilibria of the liquid metal and the atomic physics taking place (ms vs.  $\mu$ s) [49]. Because of this dynamical aspect of the vapour cloud, during the cycles there is a periodically varying shielding effectiveness, resulting in a dynamical equilibrium between plasma and liquid surface. The studies here mentioned considered LMD technologies employing Sn or Li and operating in a regime where the vapour pressure is of similar magnitude as the plasma pressure: if the vapour shielding is achieved, steady-state operation of a LMD in reactor-relevant condition is likely to be feasible [49].

### 2.4.3 Main LM possibilities

There are different possible metals that can be used in the liquid state to face the SOL plasma, but to discuss them it is important to have clear in mind what are the main parameters that can drive the choice. LM candidates should be evaluated according to the melting and boiling points, the thermal conductivity and chemical compatibility with substrate materials and plasma constituents and, last but not least, their abundance and cost [53]. The APEX studies [55] identified Li, Sn-Li alloy and a molten salt (FLIBE) as candidates, while more recently also Sn, Ga [56] and Al have been proposed [57]: among these FLIBE, Ga and Al have some issues that make them less attractive and so, for the moment, the most extensively analyzed ones in current experiments are Li and Sn [53].

Both of them have a relatively low melting point (180.5 °C for Li and 231.9 °C for Sn), but since Sn has a lower vapour pressure, its operational temperature window may be larger. Even if this last point is very important for what concerns the difference in the evaporation flux at a certain temperature, another very important difference lies in their atomic number  $Z$  (3 for Li and 50 for Sn) and it strongly affects the radiative power, as already discussed talking about *Figure 2.7*. Considering the same picture, it is also possible to make a parallel with the choice of the solid divertor for ITER: even if it is clear that elements like tungsten are much more effective in emitting radiation with respect to others like beryllium (which is very dangerous in the case atoms reach the plasma core), by taking into account also *Figure 2.4* the picture is not that clear anymore. Indeed, tungsten has a sputtering yield threshold more than one order of magnitude larger with respect to beryllium and in addition it sputters less up to impact energies around 5 keV. Thus, there is no easy way out of this problem, which becomes a matter of trade-offs such as the one between radiation properties and the resistance of the material to high heat flux and many others. In the specific case of ITER, tungsten was chosen as divertor material, paying the price of putting a lot of attention to guarantee that the impact energy of the majority of plasma particles will be lower than the threshold energy for tungsten, not to allow any significant sputtering of the divertor atoms. On the

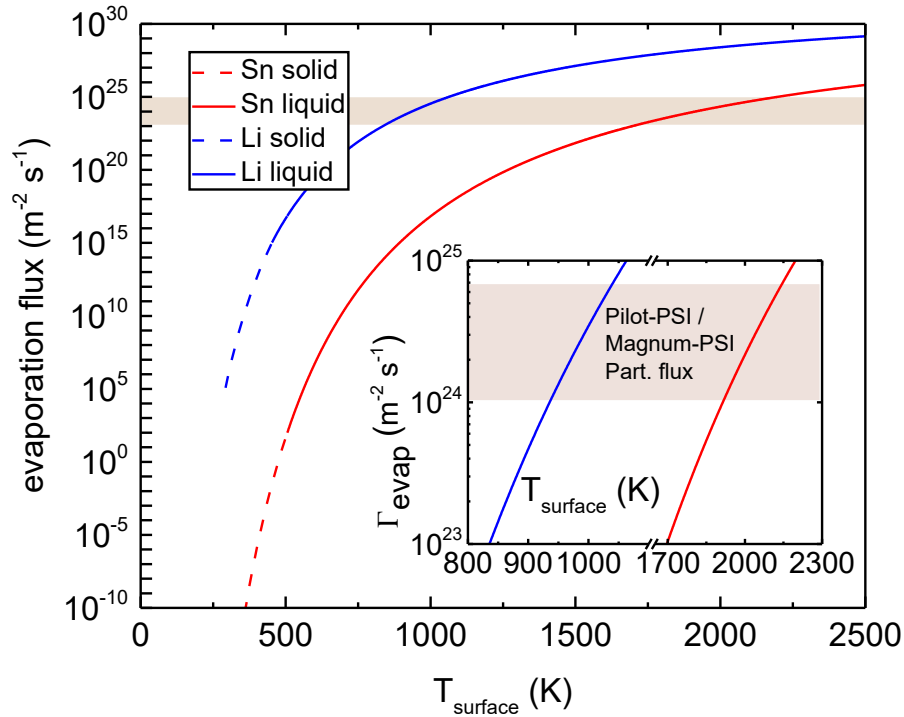


**Figure 2.15:** Evaporation rates of Sn and Li as a function of temperature. The inset highlights the typical particle flux at the target surface in Pilot-PSI and Magnum-PSI [40].

contrary, if Be would have been chosen, a larger fraction of its atoms could have been allowed since they can radiate much less.

Something similar can be said for what concerns the choice of the LM for the divertor: because of the significant difference in  $Z$  between Li and Sn, the latter will radiate much better and so a smaller concentration of tin atoms is allowed in the plasma core with respect to the corresponding lithium concentration. On the other hand, it is much easier to have significant quantities of Li inside the plasma core with respect to Sn, because of its relatively higher vapour pressure. *Figure 2.15* clearly shows the difference in evaporation flux between Sn and Li: they differ by many orders of magnitude at the same temperature. In reality, the evaporation flux is a double-edged sword: on one hand, as just said, if it increases too much it implies a larger impurity fraction in the plasma core, therefore requiring a better confinement near the surface, but on the other hand it is advantageous since it allows for additional power dissipation through the radiation channel. If the vapour pressure is counterbalanced by the plasma pressure, the impurity losses could be reduced and the steady-state vapour shielding could be more efficient [40]. In the inset of *Figure 2.15* it is highlighted the typical particle flux at the target surface

in Pilot-PSI and Magnum-PSI: to enter in this operational regime it is required a temperature  $>940$  K for Li and  $>1850$  K for Sn. Indeed, for the experiments reported in [54], the Sn targets were intentionally badly cooled to ensure the plasma and vapour pressures to be of similar magnitude. Because of this, vapour shielding is not expected to play a significant role for a Sn-based component under normal operating conditions due to the high temperature required to have a significant evaporation flux, while it can be highly protective in the case of off-normal heat loading [53]. On the other hand, lithium can exploit the vapor shielding already at relatively low temperature, but that is connected with an evaporation rate that could be too high and this problem can only be exacerbated in off-normal conditions. Thus, there is no clear winner if one stops at a superficial evaluation of the radiation and impurity concentration trade-off.

A very tricky point in the choice of the LM is the chemical compatibility with hydrogen and in particular with tritium, because of the very stringent requirements on the on-site tritium inventory (§2.1.4). In this respect, Li has a high affinity with hydrogen and it can form hydrides: this turns out to be a concern for tritium retention. Indeed, temperatures higher than  $\sim 500$  °C are required to avoid gas phase absorption in lithium, but since the temperature is not the same at the striking point and far from it, it is difficult to ensure that every point satisfies that condition [58]. Nonetheless, it must be considered that too high temperatures could enhance too much the lithium evaporation rate and thus this implies a relatively stringent operating window. For what concerns instead liquid Sn hydrogen retention, the situation is more complicated because of conflicting results in the literature. Even if some studies have reported a low deuterium retention [59][60], it has been measured in a relatively narrow range of energies and fluxes of impacting deuterium particles. Hence, further studies have been carried out: Ou et al. [61] showed that retention levels of tin constrained by a CPS (Capillary Porous Structure, §2.4.4) were around two orders of magnitude larger than for pure tungsten and the majority of the incident deuterium was retained in the Sn-wall interface. Mahnard et al. used a deuterium plasma to expose the liquid tin without exploiting a CPS (but inside a crucible): gas bubbles were formed deep inside liquid Sn layers and, based on the formation-decay equilibrium of metastable stannane ( $\text{SnD}_4$ ) molecules, the authors indicated that this could lead to an enhanced D retention [62]. To summarize, for what concerns tin tritium retention, further experiments are required to have more reliable answers, but considering the currently available knowledge, its use is not discouraged from this viewpoint [63]. Connected to this, hydrogen retention may also change the recycling regime in which the machine is operating: if a significant fraction of the plasma particles is held from the divertor, the recycling is reduced and the device moves towards a low-recycling regime. ITER will operate in a high-recycling regime and, since it will be the closest device to a future power plant,

it could be advisable to think of DEMO as a machine working in the same regime, even if for sure it is not the only approach.

Sn-Li alloys may be a very interesting option as well, since they could merge the best aspects of each metal, but for the moment more research is required on them.

#### 2.4.4 Main LMD concepts

The choice of the LM to be employed may also be done in accordance to the specific engineering choice that is made to build a divertor and for this reason it is fundamental to address in this section the engineering perspective of a LMD. In principle one could think of some conceptual designs to start addressing this point and they could be divided in those adopting an evaporation chamber or not. An evaporation chamber is a volume delimited by walls with just some void in order for the plasma to enter inside it: in such a way the evaporated LM can be better confined and, considering the same number of atoms escaped from the divertor, the metal vapour density will be higher and it will better protect the divertor from the plasma. Examples of such designs are shown schematically in *Figure 2.16*, where there are four types of evaporation chambers. Even if it represents a double-null configuration with a different design for each divertor leg, it is just for the sake of saving space and representing all the concepts in a single drawing; eventually only one design will be used for all the divertor legs (and probably in a single-null configuration). The option (a) is the simplest one: a liquid metal pool (in yellow) is directly exposed to the SOL plasma and it is at the bottom of an evaporation chamber. In this chamber the LM can evaporate, while next to it there is a differential evacuation chamber, where the vapor enters thanks to the differential pressure and it is then pumped away with the vacuum pump, which guarantees that the main plasma is not contaminated too much. This double chamber idea is common to all the four designs discussed in Nagayama's study. The walls are drawn with blue circles to emphasize that they are actively cooled: a significant fraction of the evaporated LM condensates on the wall and goes back to the pool in liquid state. Considering that this cycle occurring in the evaporation chamber is not closed, since there are losses to the differential evacuation chamber and to the plasma chamber, a lithium circulation system may be added to the LM pool (d): it is very useful to prevent the lithium pool from drying up and the reservoir allows a more flexible operation. The pool design has the advantage of being very simple, but it cannot be installed in the upper divertor (if necessary) and, more importantly, it lacks controllability since a large heat pulse coming from SOL plasma (occurring in off-normal conditions, for example) may cause LM splashes.

Both these problems could be solved adopting a porous medium (wick) (b): the

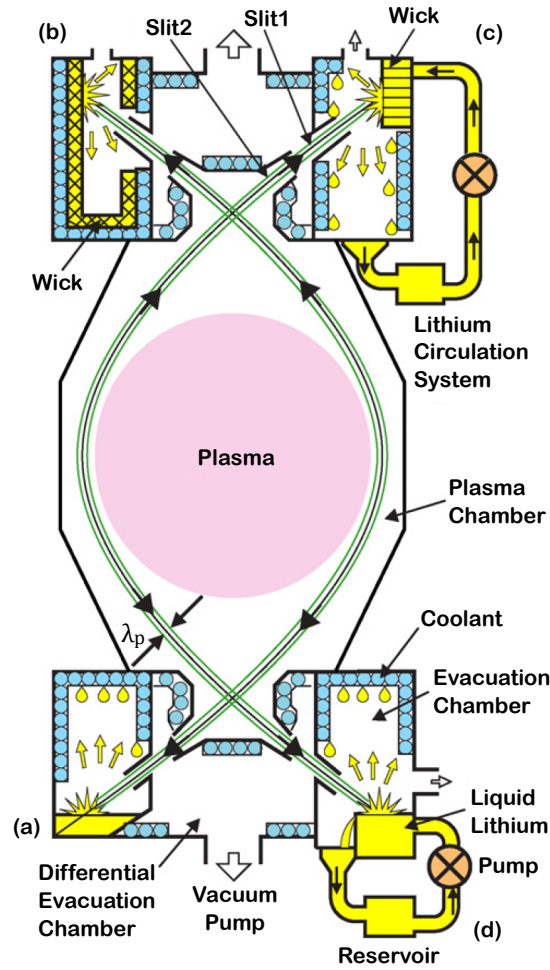


**Figure 2.16:** Schematic view of a liquid lithium divertor system. Four different evaporation chamber types are shown: (a) lithium pool; (b) wick; (c) wick and circulation pump; (d) lithium pool and circulation pump [64].

capillary forces keep the LM inside the meshes/capillaries, with a very thin layer facing the plasma: in the case it evaporates, the underlying liquid metal can readily substitute it thanks to the circulation by capillary action. This capillary porous structure (CPS) can be very helpful to suppress splashing of liquid metal and, in the case of lithium evaporation from the wick, it showed a cooling capability of more than  $30 \text{ MW/m}^2$  [66]. By adding an external LM circulation system (c), it is possible to enhance the cooling capabilities and to better repair the solid porous material that holds the liquid metal from the SOL plasma. This latter point is of paramount importance: if locally the LM is not able to quickly cover again the surface, the solid structure is exposed to the plasma and this is of concern since it

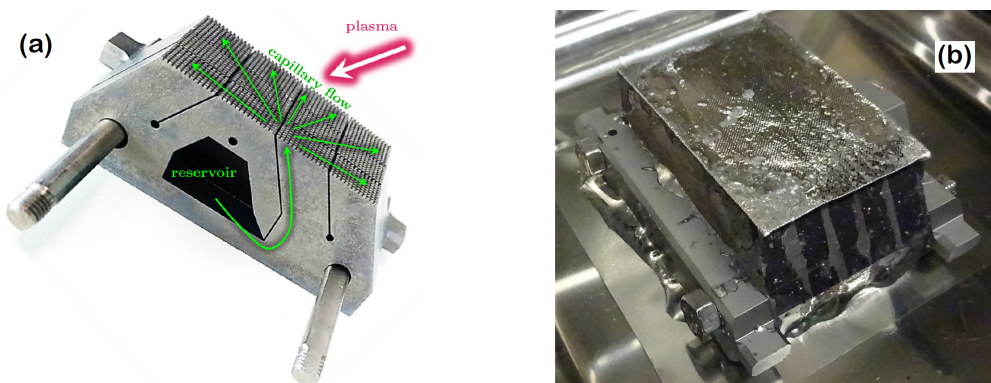


**Figure 2.17:** Partially disassembled titanium-zirconium-molybdenum (TZM) alloy target (a) to show how lithium is transported from the reservoir via the whicks across the surface, due to capillary forces. The TZM target is filled with lithium and it is covered by a mesh layer, clamped between the outer two layers of the target (b) [65].

may melt, eliminating the pores from the surface and, thus, preventing the liquid metal from covering it again. A schematic drawing of a CPS is the one reported in *Figure 2.10*, but it is possible to give a look to a real CPS structure in *Figure 2.17*: it has been used experimentally in the study performed by Rindt et al. in 2019 [65].

All the possible solutions presented by Nagayama in *Figure 2.16* could also be considered without evaporation chamber, losing its advantages but gaining simplicity: for examples there are ITER-like LMDs that adopt a CPS-based divertor without the chamber and this is considered the main solution at the moment (a possible example of it has been proposed by Vertkov et al. [67]).

In any case, there exist also other possibilities of engineering designs of a LMD. One of the main alternatives to CPSs is the vapor box divertor [68][69], depicted in *Figure 2.18*. It is constituted of different chambers, each one with decreasing metal vapour density starting from the bottom (it is represented by the green intensity in the picture). While the bottom chamber is where the liquid metal radiates the largest fraction of plasma power, exploiting the vapour shielding phenomenon, in the other ones the baffles help to condense the escaping impurities on their cold surfaces, also exploiting the differential pumping. Not only this prevents an excessive amount of LM to reach the plasma chamber and consequently its core, but the increasing vapour density along the field line helps to stabilize the detachment front. The disadvantage of this technology is the area of communication between the different chambers: the separatrix is not fixed and it is therefore needed to have a safe margin, since the solid material of the box cannot afford to face directly

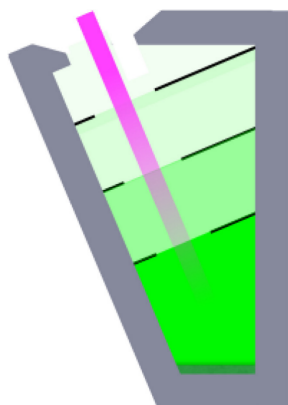


**Figure 2.18:** Schematic poloidal cross-section of a lithium vapor box divertor [69].

the plasma flux. Though, the size of the channel can not be too large, because otherwise the concentration of impurities in the plasma chamber could become excessive.

Finally, other possible LMD designs imply a movement of the liquid metal: either just flowing on a solid divertor with an ITER-like shape, or through LM jets [70]. Adopting these technologies could be more advantageous from the point of view of the protection of the solid structural material, but their engineering aspect is really complex. Indeed, liquid metals are subjected to the forces arising from the electromagnetic field ( $\mathbf{J} \times \mathbf{B}$ ) and that could deviate the flow, which has to be carefully controlled in order not to have LM droplets inside the plasma chamber. Because of this additional engineering complications, the designs that have been investigated the most are the CPS and the vapour box and they are likely to be those that will be further tested in DTT and employed in DEMO.

### 2.4.5 LM perspectives

Despite all the potential advantages of LM employment to solve the power exhaust problem, it is still needed care to choose them over a solid divertor. In principle, one could still think to use the latter also in DEMO exploiting the solutions mentioned in *Section 2.3.3* (such as impurity seeding and advanced divertor configuration) in order to reduce the heat flux coming to the solid surface. Notwithstanding the difficulties that such options imply, the solid divertor may be preferable for different reasons: its performance is characterized by a much greater body of knowledge, it is much simpler to operate and its technological maturity is much higher with respect to liquid metals [53]. Of course this last point translates also in a much greater potential of LMDs, but it is necessary to take into account all the potential

issues as well in order to make a choice. The main ones concern the engineering design and the operational issues, both in terms of the likelihood to turn-off the plasma and in safety terms (for example due to tritium retention, but not only).

In any case, if the results of ITER are unfavourable in extrapolating a W-based divertor to DEMO, it is imperative to develop at least one LM-based PFC design to a sufficiently advanced level in order for it to be considered as a viable alternative for DEMO design [53]. In this context, linear plasma devices play a role of paramount importance (§2.3.4): they are simpler to operate with respect to tokamaks, they allow a very good diagnostic access (and they are simpler to diagnose) and they offer a great flexibility in exchanging test samples [53]. Even if LPDs can not give any help in addressing the problem of how the impurities will travel in a tokamak environment and how many of them will reach the plasma core and how they affect it, they can be a powerful mean to study the physics from the LMD perspective rather than from the point of view of the plasma. Indeed they can help to better understand the physics of LM-plasma interaction and to design and test real LMD proposals under realistic loading conditions. Thus, studies performed in LPDs are complementary to the ones done in a tokamak environment, where it is possible to analyze the very complex interaction of the liquid metal with the edge and core plasma.



## Chapter 3

# Development of a 0D model including the LM

Now that the physical and engineering background has been better defined, it is time to introduce the core of this thesis. This chapter starts with the discussion of the motivations and the main goals of this work, discussing its potential usefulness and stressing once again its context (§3.1). *Section 3.2* describes the model developed by Tonello et al. [71], that is the basis upon which the new model erects. The theoretical way in which it has been expanded for the purpose of this thesis is addressed thereafter (§3.3) before analyzing the results in the following chapter.

### 3.1 Thesis' motivations and goals

#### 3.1.1 The importance of models

In the previous chapter it has been discussed how liquid metal divertors (LMDs) represent an opportunity to better deal with the plasma exhaust problem and why linear plasma devices (LPDs) are useful to test them and to analyze their operation under reactor-relevant plasma conditions. As in many engineering fields, the experiments are fundamental but it is often necessary to accompany them with suitable mathematical and computational models of the reality. This because experiments require time and funding to be carried out and in some instances it is not easy to extract reliable measurements (and thus results) from them or it is not practical to even perform them. For these reasons, it is important to have computational models that can solve problems of engineering relevance since they can be complementary to experiments: they can help to better understand phenomena occurring in a given experiment and they allow to obtain results in the cases in which experiments have not been performed (yet). Computational models,

in the case they are verified and validated, also have predictive capabilities within the development perimeter and this turns out to be very useful in order to design components or systems. For example, by simply changing the input parameters (always paying attention not to make extrapolations, or at least taking them into account in the results reliability), it is possible to extract results in a relatively short time if compared with building the whole system/component and testing it.

The edge plasma in tokamaks has a collisionality regime in between the fluid approximation and the kinetic description, implying the impossibility to perfectly describe it employing just one of the two models. The approaches developed to describe the plasma in regions include mean-field fluid models [72], turbulent fluid models [73][74], hybrid fluid-kinetic models for electronic population [75] and full gyrokinetic models [76]. Today, the most used approach for the interpretation of experiments and in the design phase is the mean-fluid approach: numerical codes exploiting this approach are, among others, SOLEDGE2D [77] and SOLPS-ITER, specifically used for the ITER divertor design [78][79]. These codes merge a 3D kinetic description for neutral particles with a 2D multi-fluid description for electron and main ion/impurity populations and they are able to exploit realistic divertor geometries and configurations. Once made some simplifying assumptions, such tools give the possibility to run simulations in a self-consistent way, paying the price of an onerous computational cost and, in some instances, of a not straightforward interpretation of the results [71]. Especially this last point could be tackled by supporting the utilization of such complex and long-running computational models with much simpler ones, that could help with the interpretation of the results. An approach to do so is the adoption of a model that takes into account only the average of relevant quantities over a specified space volume. These global (or zero-dimensional, 0D) models allow for great simplifications since the number of equations and of the contained terms will be significantly reduced; moreover, only the time dependence will be left, leading to a description based on ordinary differential equations (ODEs). By getting rid of spatial complexity the model turns out to be faster while still being able to reproduce the behavior of key quantities of the plasma edge such as temperature and density. Not only, but in principle it is possible to take into account more terms inside the governing equations, adding pieces of physics that may be important without having problems of high computational times. Another advantage of such modelling approach is that, because of its simplicity, the interpretation of the physics is more straightforward with respect to complex codes. Of course one must remember that simplicity is a double-edged sword: such simple models require to neglect many terms and dependences that can be of paramount importance especially for local phenomenon, whose development could end up to consequences to the whole domain. These are the reasons why 0D models can be tempting, especially if they are in

communication with more complete (and complex) codes like SOLPS-ITER.

### 3.1.2 Aim of the thesis

Having discussed the motivations that drive this work, it is now time to better outline what the concrete goals are and on which bases they erect. 0D models could, in principle, offer the opportunity to quickly interpret results of more complex codes or experiments and this connection could be much improved in the case of simple geometries, for which the global model could be more reliable with respect to the case of a very complex spatial configuration. As described in *Section 2.3.4*, LPDs offer a good environment where to test the interaction physics between a target and a plasma with parameters similar to the ones of the edge plasma in a fusion reactor. Because of their very simple cylindrical geometry and uniform magnetic field, they are a very suitable test-bed for a 0D model aimed at studying edge plasma physics and PMI.

In their paper [71], Tonello et al. developed a 0D model based on the equations obtained from the space integration of SOLPS-ITER model for GyM (Gyrotron Machine), a linear plasma device operating at ISTP-Milano [80]. Their aim was to build a model with a direct connection with the results of SOLPS-ITER: they investigated a weakly-ionized helium plasma in GyM and they compared the results of the 0D model with those of the 2D SOLPS-ITER simulations. Since this is the starting point of this thesis work, the work presented in [71] will be better described and analyzed, at least for what concerns the theory behind it, in *Section 3.2*. Indeed, thanks to the fact that this thesis work is the fruit of a collaboration between Politecnico di Torino and Politecnico di Milano, it was possible to obtain the source code implementing the model developed by Tonello et al., with the objective of improving it, making it applicable for the intended application of the present thesis: the analysis of the inclusion of LM populations in LPDs. Because of the importance that LMDs will likely have in the future fusion energy and because of the ease with which they can be tested in LPDs, it would be really attractive to expand the already developed global model in such a way to account for the liquid metal. As a consequence of its simplicity, in principle it could be even possible to computationally model the dynamics of the vapour shielding phenomenon. Since it is caused by the very different time-scales of atomic physics and conduction heat transfer (3 orders of magnitude apart), it is very difficult to catch it with a model that involves also the spatial dependence; if, instead, the focus is only on the time behaviour, the likelihood of having a suitable model for vapour shielding increases. To summarize, the final goal of this thesis work is to improve the model proposed in [71] in such a way to get closer to a model that could eventually reproduce the vapour shielding behavior and which could then be used to reproduce some of the

already-cited experiments regarding LPDs with LM targets.

In order to better discuss the changes that must be made to the starting model, it is necessary to analyze it in more detail: the next section will better outline its objectives and results and, more importantly, the employed equations together with the considered approximations.

## 3.2 Available model description

The model developed by Tonello et al. will be now discussed in greater detail and, consequently, their paper [71] will constitute the main reference throughout the whole section. The general context of the model is better defined in *Section 3.2.1* before discussing the exploited equation and stressing the assumptions made (§3.2.2). Afterwards, the main results reported in the paper are briefly summarized in order to understand the potentialities of this model (§3.2.3).

### 3.2.1 General context

First of all, their goal was to develop a 0D model (or point model) that could provide crucial interpretative keys in the investigation of the physics of edge plasmas in LPDs. To accomplish this, the employed equations were based on the space integration of the fluid equations present in SOLPS-ITER model for a LPD and they were then used to compare the results both with some experimental data of GyM and with 2D simulations of GyM performed with SOLPS-ITER.

GyM, as other LPDs, is made of a cylindrical vacuum chamber surrounded by coils that produce straight magnetic field lines parallel to the cylinder axis. Gas is injected inside the chamber through a puffing nozzle and it is pumped out by turbomolecular pumps, obtaining a stationary gas pressure. By supplying external power to the gas the plasma is generated and it follows the magnetic field lines, going towards the bases of the cylinder (targets). Though, while streaming along the magnetic field lines, the plasma undergoes also a process of slow cross-field diffusion, escaping the magnetic confinement. A 3D CAD image of GyM is displayed in *Figure 3.1a*, which also highlights its main components.

The model considered a weakly-ionized helium plasma: He will be present as a product of D-T fusion reactions and it will also constitute the main plasma species in the first phase of ITER operation, before employing deuterium and tritium [5]. Additionally, helium can be suitable for a newly developed model since it removes complexities related to molecular species and it reduces the number of unknowns. In any case, conceptually speaking it should be clear how to generalize the point model to other plasma species [71].

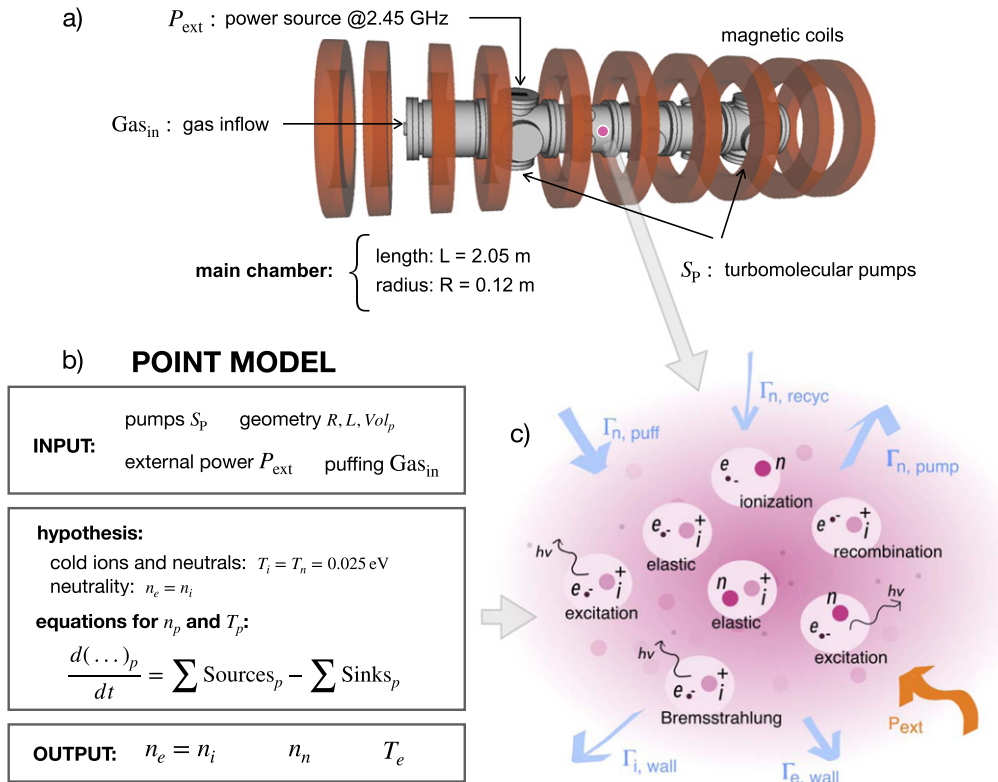


**Figure 3.1:** a) 3D CAD image of GyM, highlighting its main components; b) blocks summarizing the main elements of the 0D model; c) schematic representation of the global LPD domain, considering the sources and sinks in the plasma balance equations; fluxes through the point domain boundaries, atomic processes and the externally supplied power [71].

### 3.2.2 Principles of the point plasma model for LPDs

A 0D model for an LPD plasma is based on a set of space-independent balance equations describing the volume average densities and temperatures of each plasma population [71]. Their time evolution is assessed solving a system of ODEs in which the variations of the quantities of interest are expressed in terms of sources and sinks: their schematic summary is represented in *Figure 3.1c*. As a consequence of the equations simplicity, it is possible to easily examine the relative contributions of the different sink and source terms in determining a stationary situation. Even if, because of the objective of the model, most of the contributions in SOLPS-ITER model are included, there are a couple of exceptions: global ambipolarity is assumed (no plasma currents) and heat conduction contribution in the electron temperature balance is neglected. Both these assumptions are justified in the context of the sheath-limited plasma conditions expected in GyM [71].

The model developed by Tonello et al. takes into account three plasma populations: electrons (e), neutral atoms (n) and singly ionized ones (i) (consistently with the low ionization degree and expected electron temperature range [71]). Thus, in principle, the unknowns of the problems should be 6: the density and temperature values for each population. Though, considering some assumptions that could be valid for typical LPDs, the unknowns could be reduced to 3: plasma neutrality sets  $n_i = n_e$  and neutral and ion temperatures are assumed to be constant and equal to the room temperature ( $T_i = T_n = 0.025$  eV). Plasma neutrality and the hypothesis on  $T_n$  are usually verified in edge plasma models and in LPDs, respectively. The effect of ion temperature has instead been considered negligible *a posteriori* and explained considering that, since the electron-ion collision frequency is low, a small fraction of the electron energy is lost by thermal equilibration with ions. Thus, since the unknowns are just  $n_i$ ,  $n_n$  and  $T_e$ , their balance equations are:

$$\frac{dn_i}{dt} = R_{iz}n_en_n - R_{rc}n_en_i - \Gamma_{i,\text{wall}}n_i \quad (3.1)$$

$$\frac{dn_n}{dt} = -R_{iz}n_en_n + R_{rc}n_en_i + \Gamma_{n,\text{recyc}}n_i - \Gamma_{n,\text{pump}}n_n + \frac{\Gamma_{n,\text{puff}}}{\text{Vol}} \quad (3.2)$$

$$\begin{aligned} \frac{3}{2}n_e \frac{dT_e}{dt} = & + \frac{P_{\text{ext}}}{\text{Vol}_e} - E_{iz}R_{iz}n_en_n - E_{\text{rad},i}R_{\text{rad},i}n_en_i \\ & - E_{\text{rad},n}R_{\text{rad},n}n_en_n - \Gamma_{e,\text{wall}}T_en_e \\ & - \frac{3}{2} \frac{2m_e}{m_i} R_{\text{el},i}n_in_e(T_e - T_i) - \frac{3}{2} \frac{2m_e}{m_i} R_{\text{el},n}n_n n_e(T_e - T_n) \\ & - \frac{3}{2}(R_{iz}n_en_n - R_{rc}n_en_i - \Gamma_{i,\text{wall}}n_i)T_e \end{aligned} \quad (3.3)$$

where  $m_i$  and  $m_e$  are respectively the ion and electron masses and  $P_{\text{ext}}$  is the external power supplied to electrons. All the other terms are explained and made explicit hereafter.

Since in [71] the fluxes  $\Gamma$  are expressed in  $\text{s}^{-1}$  and cgs (centimeter–gram–second) system of units is used, it is needed to manipulate the mass inflow  $\text{Gas}_{\text{in}}$  and the total pumping speed  $S_{\text{P}}$ , which are respectively expressed in standard cubic centimeters per minute (sccm) and in liter/s, in order to have the wanted units:

$$\Gamma_{n,\text{puff}} = \text{Gas}_{\text{in}} \cdot 4.48 \cdot 10^{17} \quad (3.4)$$

$$\Gamma_{n,\text{pump}} = \frac{S_{\text{P}} \cdot 10^3}{\text{Vol}_n} \quad (3.5)$$

Atomic reactions are characterized by the already mentioned reaction rate coefficients  $R$  (§1.4.1): the rate and power coefficients for ionization ( $R_{iz}$ ), recombination ( $R_{rc}$ ) and excitation ( $E_{\text{rad},i,n}R_{\text{rad},i,n}$ ) are taken from the ADAS/adf11 database [39], which is the same that SOLPS-ITER uses. Bremsstrahlung radiation was considered

negligible in the conditions under analysis [71].  $R_{el,i} = \nu_{ei}/n_i$  is the electron-ion elastic rate coefficient and it is computed exploiting the classical Coulomb collision theory [81], while  $R_{el,n} = \sigma_{el,e}v_{th,e}$  is the electron-neutral elastic rate coefficient, where the cross section  $\sigma_{el,e}$  is taken from [82] and  $v_{e,th}$  is the electron thermal velocity. This last term is neglected in SOLPS-ITER.

$\Gamma_{i,wall}$  is the loss ion flux caused by the solid chamber and it is directly derived from the volume average of the corresponding SOLPS-ITER term and it can be divided in the transport parallel to magnetic field lines  $\Gamma_{i,wall\parallel}$  and that across it  $\Gamma_{i,wall\perp}$ :

$$\Gamma_{i,wall} = \Gamma_{i,wall\parallel} + \Gamma_{i,wall\perp} = \frac{\alpha u_B A_T}{Vol_i} + \frac{D_{\perp} A_{Lat}}{\lambda_n Vol_i} \quad (3.6)$$

To obtain the expression for parallel transport it has been assumed that the plasma velocity is null everywhere except on the targets, where particles enter the sheath and the velocity complies with the Bohm criterion, which is  $u_B \simeq \sqrt{T_e/m_i}$  under the assumption that  $T_e \gg T_i$ . In this point model, indeed, the Debye sheath (§2.1.1) is not inside the domain of interest but, on the contrary, the sheath edge provides a sort of boundary condition, since it allows to impose the velocity of particles exiting the domain and going to the targets. The formulation for  $\Gamma_{i,wall\perp}$  is obtained with the diffusive approximation for radial transport, where  $D_{\perp}$  is the coefficient for anomalous diffusion and  $\lambda_n$  is the already mentioned density decay length (§2.3.2).  $A_T$  and  $A_{Lat}$  are, respectively, the total target area (twice the area of the basis of the cylinder, since in GyM the plasma goes to both targets) and the lateral wall area, while  $Vol_i$  is the volume occupied by the ions, that in principle could be different from the one occupied by neutrals. In [71] they are assumed to be equal since in GyM the plasma extends up to the lateral boundary of the cylindrical device.  $\alpha$  is the effective coefficient for parallel transport and it is defined as the ratio of target plasma density over the 0D plasma density  $n_i$ . It can be expressed analytically integrating a 1D ion momentum equation along the ion transport length (in GyM, since the plasma flows toward both targets, it is half the length of the device:  $L_{i,tr} = L/2$ ) and assuming a null neutral fluid velocity:

$$\alpha = \frac{1}{2} \left[ 1 + \frac{m_i n_n L_{i,tr}}{2T_e} R_{el,in} u_B \right]^{-1} \quad (3.7)$$

The ion-neutral collision frequency  $\nu_{el,in}$  can be expressed through the ion thermal velocity  $v_{th,i}$  and the elastic collision cross section  $\sigma_{el,in}$  (which can be taken from the AMJUEL database [83]):  $\nu_{el,in} = R_{el,in} n_n = \sigma_{el,in} v_{th,i} n_n$ . In case ion-neutral friction is disregarded, the expression simply reduces to  $\alpha = 1/2$ .

In a 0D model, the flux of neutral particles coming back from the walls to the plasma can be related to the flux parallel to  $\mathbf{B}$  with a recycling coefficient that is between 0 and 1:  $\Gamma_{n,recyc} = \beta_{rec} \Gamma_{i,wall\parallel}$ . In [71] the walls are considered to be

saturated with helium and  $\beta_{\text{rec}}$  is set to be constant in time and equal to 1, even if in principle it is also possible to account for the surface saturation process with a monotonically increasing  $\beta_{\text{rec}}(t)$ , up to unity.

Neglecting secondary electron emission, assuming parallel ambipolarity and considering floating targets, the electron energy loss to the wall per unit time and volume is given by the following expression:

$$\Gamma_{e,\text{wall}}T_e = (2 + |eV_s| + |eV_{ps}|)T_e\Gamma_{i,\text{wall}\parallel} \quad (3.8)$$

The first term in the parenthesis is due to the one-way Maxwellian heat flux of electron distribution onto the wall. Since electrons lose energy in the sheath (before reaching the wall) but it is excluded from the model domain, the actual electron energy lost by the plasma must include also the sheath and pre-sheath potential drop contributions. In  $T_e$  units these two terms read:  $|eV_s| = 0.5 \ln [(2\pi m_e/m_i)(1 + T_i/T_e)]$  and  $|eV_{ps}| = \ln \alpha$ . Only the parallel electron energy losses are considered since the radial ones are neglected. In high-density regimes it is necessary to use a more sophisticated 0D electron energy equation and the ion energy balance equation may be needed as well because of the higher collisionality.

The above-reported equations are then written in dimensionless form and they are solved in MATLAB environment. The normalization constants are the initial values for density and temperature ( $n_{i0}$ ,  $n_{n0}$  and  $T_{e0}$ ) and the initial plasma transit time  $t_0 = L_{i,\text{tr}}/u_B(T_{e0})$ . The non-dimensional variables are indicated with a *tilde* and they are:  $\tilde{n}_i = n_i/n_{i0}$ ,  $\tilde{n}_n = n_n/n_{n0}$ ,  $\tilde{T}_e = T_e/T_{e0}$  and  $\tilde{t} = t/t_0$ . The dimensionless equations are then solved exploiting the *fsolve* function in MATLAB for what concerns the steady-state values of the three unknowns, while time dependent solutions are obtained through a forward Euler finite difference solver.

### 3.2.3 Summary of the results of the model

The comparison between the developed 0D model and the 2D simulations showed good agreement in this framework of weakly ionized helium plasmas in LPDs and a satisfactory agreement has been shown also against experimental data from GyM. The 0D model was able to highlight the relevance of some terms such as the electron excitation process of neutral atoms, which provides an efficient electron heat loss mechanism, and thermal equilibration due to elastic collisions between electrons and neutrals. Both these processes are neglected in the physical model implemented in the SOLPS-ITER code.

Another big advantage of a global point model is that, because of its simplicity and small running time, it can be used to quickly perform sensitivity studies on the effect of different model parameters.

Analyzing the time evolution of the solutions it was possible to identify two

characteristic timescales: the larger one is related to the neutral pumping speed, governing the dynamics of neutral atoms, while the shorter one is associated with the plasma confinement time.

To conclude, the model developed in [71] is a promising tool that is worth to be further developed in order to support the interpretation and the design of future LPD experiments.

### 3.3 Model advancement

In light of the motivations of this thesis work (§3.1.2), two substantial steps are necessary to go from the model presented in [71] to one able to describe the oscillatory nature of the vapour shielding phenomenon:

1. two new populations need to be added: singly-ionized ions and neutrals of the LM. In principle, for each additional level of ionization a new population must be included;
2. the considered domain must move from the whole LPD to the vapour cloud region right in front of the target, since assuming a uniform density of the LM particles over the entire device is not an acceptable approximation [49].

Of course, these are not the only changes, but the others are a consequence of these in different ways. For example, because of the change of domain in order to analyze the vapour cloud, the charge exchange processes may be fundamental and they must be taken into account: this leads to the disregard of the simplified assumption that neutral atoms and ions temperatures are equal and constant.

Because of the significance of the changes on the already available model, this thesis work will mainly focus on the first step: this section will theoretically describe how LM populations will be added to the point model and *Chapter 4* will report the results of such model advancement. The change of domain of the model will instead be analyzed theoretically in *Chapter 5*, in order to establish how the model advancement presented in this thesis can be further developed in the future, eventually leading to a model able to attain the ultimate goal, that is to describe the oscillatory nature of the vapour shielding.

#### 3.3.1 Choice of the LM

To include an additional element to the previous model it is necessary to add at least two populations: neutral atoms and ions with charge +1; for every further included ionization degree the corresponding population must be incorporated. In case the temperatures of ions and neutral atoms are assumed to be constant (as in [71]), it is sufficient to add one equation for each population (the density balance

equation), otherwise the respective energy balance equations must be considered as well.

In the model here developed, lithium has been chosen as liquid metal because it is one of the main candidates for LMD technologies together with tin (§2.4.3). Though, with respect to the latter, it is better characterized for what concerns atomic physics data and, moreover, the second ionization potential of Li (76 eV) is much higher with respect to Sn (15 eV) (and also higher than He, for which it is 54 eV) [84]. This last point does not mean that, since the second ionization potential of lithium is much higher than the expected plasma temperature, there will not be atoms with a larger ionization degree; though, the approximation of considering only a singly-ionized population is much more realistic for lithium than for tin. For this couple of reasons the choice of lithium seems a more suitable one for the development of this new model, since it can be convenient to start with as few equations as possible and avoiding too many uncertainties induced by the LM choice itself (lower reliability of atomic data and worse approximation if only ions with charge +1 are considered). Of course, if the needed atomic data are available and equations for higher ionization degrees populations are added (the actual number of populations to be included depends on the wanted degree of accuracy in this respect, having as a limit the atomic number of the species), it will be straightforward to change the model in order to take into account a different liquid metal.

### 3.3.2 Addition of the LM populations

In this first modification of the model introduced in *Section 3.2*, the main changes regard the number of equations describing the 0D LPD domain and the electron energy balance equation. Indeed, if only singly-ionized lithium ions are considered, two equations must be added to describe the densities of the neutral and ionized LM populations, while the electron energy balance equation must account for additional sink channels due to the different possible interactions with lithium atoms. Practically, *Equations (3.1)-(3.2)* are kept as they are (and of course they are referred to helium), while their lithium counterparts will be added to the system of equations:

$$\frac{dn_{\text{Li}^+}}{dt} = R_{\text{iz,Li}} n_e n_{\text{Li}^0} - R_{\text{rc,Li}} n_e n_{\text{Li}^+} - \left( \frac{\alpha_{\text{Li}} u_{\text{B,Li}^+} A_{\text{T}}}{\text{Vol}_i} + \frac{D_{\perp,\text{Li}} A_{\text{Lat}}}{\lambda_{n,\text{Li}} \text{Vol}_i} \right) n_{\text{Li}^+} \quad (3.9)$$

$$\begin{aligned} \frac{dn_{\text{Li}^0}}{dt} = & - R_{\text{iz,Li}} n_e n_{\text{Li}^0} + R_{\text{rc,Li}} n_e n_{\text{Li}^+} + \beta_{\text{rec,Li}} \frac{\alpha_{\text{Li}} u_{\text{B,Li}^+} A_{\text{T}}}{\text{Vol}_i} n_{\text{Li}^+} \\ & - \frac{S_{\text{P,Li}^0} \cdot 10^3}{\text{Vol}_n} n_{\text{Li}^0} + \frac{\text{Gas}_{\text{in,Li}^0} \cdot 4.48 \cdot 10^{17}}{\text{Vol}} \end{aligned} \quad (3.10)$$

where, as already discussed for helium,  $\text{Gas}_{\text{in,Li}^\circ}$  is expressed in sccm and  $S_{\text{P,Li}^\circ}$  in liter/s, while the unknowns are expressed using the cgs system of units.

The electron temperature balance equation (3.3) will be instead substituted by the following one:

$$\begin{aligned}
 \frac{3}{2}n_e \frac{dT_e}{dt} = & + \frac{P_{\text{ext}}}{\text{Vol}_e} - E_{\text{iz,He}}R_{\text{iz,He}}n_en_{\text{He}^\circ} - E_{\text{iz,Li}}R_{\text{iz,Li}}n_en_{\text{Li}^\circ} \\
 & - E_{\text{rad,He}^+}R_{\text{rad,He}^+}n_en_{\text{He}^+} - E_{\text{rad,Li}^+}R_{\text{rad,Li}^+}n_en_{\text{Li}^+} \\
 & - E_{\text{rad,He}^\circ}R_{\text{rad,He}^\circ}n_en_{\text{He}^\circ} - E_{\text{rad,Li}^\circ}R_{\text{rad,Li}^\circ}n_en_{\text{Li}^\circ} \\
 & - (2 + |eV_s| + |eV_{ps}|)(\alpha_{\text{Li}}u_{\text{B,Li}^+} + \alpha_{\text{He}}u_{\text{B,He}^+}) \frac{A_{\text{T}}}{\text{Vol}_i} T_e n_e \\
 & - \frac{3m_e}{m_{\text{He}}} R_{\text{el,He}^+} n_{\text{He}^+} n_e (T_e - T_{\text{He}^+}) - \frac{3m_e}{m_{\text{Li}}} R_{\text{el,Li}^+} n_{\text{Li}^+} n_e (T_e - T_{\text{Li}^+}) \\
 & - \frac{3m_e}{m_{\text{He}}} R_{\text{el,He}^\circ} n_{\text{He}^\circ} n_e (T_e - T_{\text{He}^\circ}) - \frac{3m_e}{m_{\text{Li}}} R_{\text{el,Li}^\circ} n_{\text{Li}^\circ} n_e (T_e - T_{\text{Li}^\circ}) \\
 & - \frac{3}{2} T_e \left( \frac{dn_{\text{He}^+}}{dt} + \frac{dn_{\text{Li}^+}}{dt} \right)
 \end{aligned} \tag{3.11}$$

where the flux terms have already been made explicit according to what said in [Section 3.2.2](#).

One of the main differences between this and the original model is the fact that the electron density is now dependent on two unknowns instead of one, indeed:  $n_e = n_{\text{Li}^+} + n_{\text{He}^+}$ . This complicates a little bit the equations to be solved, since the electron density is present in all terms regarding atomic processes and in the electron energy loss term to the wall. Another big difference simply lies in the different coefficients and reaction rates of lithium with respect to helium, so it is worth to point out their origin for lithium as well. The rate and power coefficients for ionization, recombination and excitation are taken from the ADAS/adf11 database [39] as for the helium, since they are both available. The electron-neutral elastic rate coefficient for lithium is taken from [85]: a linear extrapolation in 4 points is used and it can be expected to be a good approximation because of the relatively large uncertainty of the data. Instead, the rate coefficient for elastic collisions between electrons and lithium ions  $R_{\text{el,Li}^+}$  is computed, as for helium, exploiting the classical collision frequency from Coulomb collisions: this has to be considered as a very first approximation, since in principle the formula taken from [81] is valid for a simple two-component plasma made of electrons and charged ions. Though, this approximation may be supported from the fact that, since Coulomb collisions depend on the charges between the interacting particles, it is roughly the same to consider a singly-charge ion of different elements, on the condition that they will

stay sufficient far away from each other not to get too close to the nucleus. Also the cross-field diffusion parameters  $D_{\perp}$  and  $\lambda_n$  are assumed to roughly be of the same order of magnitude as helium, even if in the equations describing confinement (like *Equation (1.13)*, in a very simple case) depend on the particle mass, that is different in the two cases and in principle plays a role. Since in the simulations of this first model ion-neutral collisions are neglected,  $\alpha_{\text{Li}} = \alpha_{\text{He}} = 0.5$ , according to *Equation (3.7)*. This has an implication also on the electron energy loss term: since  $|eV_{ps}| = \ln \alpha$ , it will be the same for lithium under the previous assumption. For what concerns instead the potential drop across the sheath, it depends on different parameters such as ion masses and electron temperature, but since it does so logarithmically, it can be just considered similar to the case with just helium and in any case it is  $\approx 3$ , as reported in *Equation (2.2)* (paying attention that  $|eV_s|$  refers just to the coefficient that is then multiplied by the electron temperature in energy units).

Finally, for what concerns the neutral lithium sources in *Equation (3.10)*, the pumping and puffing are set through a variable in such a way to be proportional to the helium one (even if they can be expressed without this dependence as well, depending on what is most convenient), while the equations are assumed to be solved starting from a time at which the walls are already saturated with lithium (as it is done for helium), implying that  $\beta_{\text{rec,Li}} = 1$ .

### 3.3.3 Initial conditions and model switches

The initial conditions of the neutral helium and lithium densities for the model are evaluated thanks to a MATLAB function that, starting from an arbitrary density inside the LPD, computes the densities of neutral atoms considering a 4 seconds transient due to puffing (inserted through a step function after 0.2 s) and pumping. The latter is multiplied times the density and, hence, entails the attainment of an asymptote for time going to infinity: practically, the previously-mentioned 4 seconds are enough to be very close to a stationary situation with all the input values used. The initial total ion density is instead set to  $10^{10} \text{ cm}^{-3}$  as in [71] and the division between helium and lithium ions is done through an arbitrary percentage coefficient. The initial condition for the electron temperature is set to 5 eV as in [71].

The model presents two switches: one to choose whether to include the liquid metal into account and the other to select the LPD under consideration. Through the former (LM switch), it is possible to set the lithium pumping and puffing parameters to zero, together with the electron-ion elastic collision frequency  $\nu_{ei} = R_{\text{el,Li}^+} n_{\text{Li}^+}$ . In principle, also the initial conditions of lithium ions and neutrals densities should follow the same fate, but they need more care: because of computational concerns,

it is not possible to set them exactly to zero and, thus, they are set to 1 particle/cm<sup>3</sup>. Such a switch readily enables a confrontation with the original model and this will be discussed in *Section 4.1*.

The LPD switch is instead due to the fact that in some LPDs (such as GyM) the plasma flows toward both targets, while in others it only goes toward one: this introduces a factor 2 in the terms that contain the total target area (e.g. the transport parallel to the magnetic field lines, *Equation (3.6)*). The purpose of this second switch is, again, to provide a very easy and fast way to change the LPD configuration without having to directly modify all the needed terms in the equations.

### 3.3.4 Limitations and expectations

To conclude, in this first model advancement the liquid metal is supposed to be injected from the outside and it is not coming self-consistently from the liquid metal target; moreover, it is averaged over the whole LPD even if the density is expected to be much greater near the LM target(s). Thus, the model now developed has no presumption of describing a real LPD plasma interacting with a liquid metal target, but it is a necessary step to move toward that direction: pieces of physics will be introduced step by step while checking that the outcomes are physically realistic and corresponding to the expectations. Because of what just said, lithium is expected to have a very limited impact on the original model because of its low density (since it is averaged over the whole LPD): the results of this first new model will be evaluated in *Sections 4.1*.



# Chapter 4

## Overview of the results

This chapter will deal in detail with what regards the employment of the model previously introduced (§3.3): after discussing the rationale of its utilization, the outcomes are reported together with the associated interpretations. *Section 4.1* reports a sanity check of the advanced model, exploiting the original one as a benchmark, while the following one (§4.2) summarizes the results obtained “switching on” the lithium presence, but still maintaining it at low levels if compared to helium: this is physically closer to what happens if the physics of plasma-LM interactions is considered making averages over the whole LPD chamber. Though, since it is expected that this will lead to very small changes with respect to the original model, it has been thought to tune lithium input parameters, trying to simulate with the same model the change of domain, but without touching the equations: the results of this approach are reported in *Section 4.3*. All the results will be contextualized and the limits of each employment of the model will be underlined in the respective sections.

The reference input data that will be used throughout the first two sections (§4.1-4.2) (unless differently specified) for both the advanced and the original model are:  $P_{\text{ext}} = 540 \text{ W}$ ,  $S_{\text{P,He}} = 760 \text{ Ls}^{-1}$ ,  $\text{Gas}_{\text{in,He}} = 20 \text{ sccm}$  and  $n_{e0} = 10^{10} \text{ cm}^{-3}$ . The lithium inflow, pumping speed and initial ion density are specified as a percentage of their helium counterparts through some coefficients  $a$ :  $\text{Gas}_{\text{in,Li}} = a_{\text{puff}} \text{Gas}_{\text{in,He}}$ ,  $S_{\text{P,Li}} = a_{\text{pump}} S_{\text{P,He}}$  and  $n_{\text{Li}^+0} = a_n n_{e0}$ . The numerical values of these coefficients are reported in the following, since they will be different depending on the model employment. Of course it is not compulsory to add such a dependence on helium parameters, but this simplifies the process of choosing lithium input variables in relation to helium ones; if, instead, one wants to define their absolute value, it is straightforward to define them as independent variables. The LPD switch has been set in order to account for GyM unless differently specified: this will be necessary for a better comparison with the original model.

## 4.1 Benchmark against original model

One of the first things to be done when a new model is developed is to benchmark it against an already existing model that has been proven to be reliable. Since the model here considered is an advancement of a previous one, it is obvious that the original one represents a good basis for comparison. Specifically, thanks to the LM switch introduced in the model (§3.3.1), it is possible to disregard the LM atoms in the new model: if the LM is turned off and all the inputs common to the two models are equivalent, the outcomes of the advanced model must be expected to be very close with respect to those reported in [71], even if the actual equations to be solved are different. Of course there will not be a perfect match between the two models and this is due to the different equations and way of solving them numerically and to the fact that it is not possible to set the initial lithium densities exactly to zero because of computational issues.

Evaluating the trends over time of the three unknowns that are present in both models (the neutral atoms and ions helium densities and the electron temperature) it is impossible to spot any difference and thus, qualitatively, the expectations are fulfilled. From the quantitative point of view, instead, it is possible to focus on the difference of the steady-state values of the common unknowns, computing the

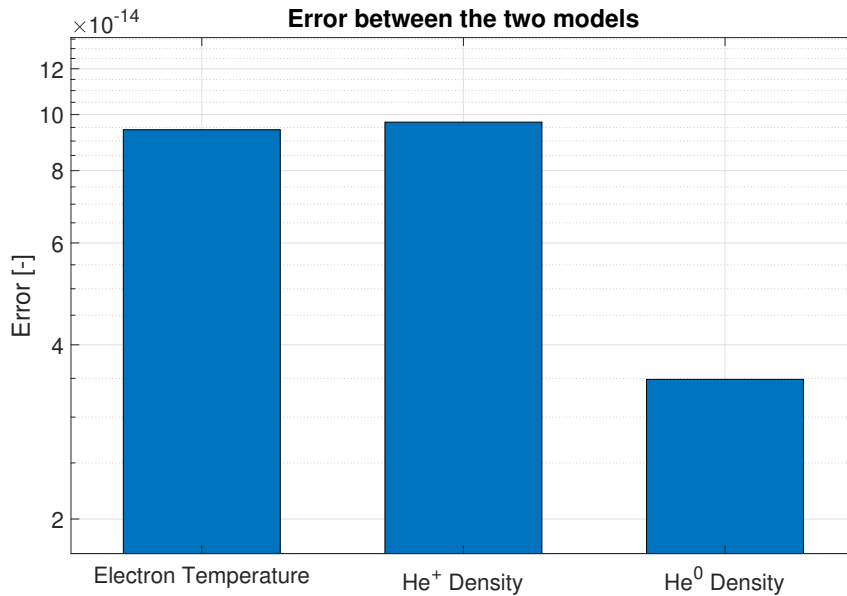


**Figure 4.1:** Magnitudes of the error for the three common unknowns (electron temperature, helium ions density and helium neutrals density) between the advanced and the original model.

error of the advanced model with respect to the original one. Such results are displayed in *Figure 4.1* and it is clear how the discrepancy between the two models is extremely small: all the errors of the different parameters are between  $10^{-14}$  and  $10^{-13}$ . Because of their proximity to the value of the machine epsilon, which is the upper bound of the relative error due to the intrinsic rounding operation in floating point arithmetic, such errors are presumed to be of computational nature only, perfectly in agreement with the expectations.

## 4.2 Lithium “switching on”

After the sanity check of the model, it is time to switch on the lithium presence in the model (still keeping it limited) in order to evaluate its impact. The reference coefficients used in this section for the lithium inflow, pumping and initial ion density (they have been introduced at the beginning of *Section 4.1*) are, respectively,  $a_{\text{puff}} = 10^{-4}$ ,  $a_{\text{pump}} = 0.5$  and  $a_n = 10^{-4}$ . Physically speaking, since the main plasma is made of helium only, the lithium puffing and initial ion density must be orders of magnitude smaller with respect to He, thus explaining the small coefficients; for what concerns instead the pumping speed, it can be thought to be on the same order of magnitude for the two elements (of course the outgoing flux will be much smaller for lithium, since it also depends on the density). In any case, in *Section 4.2.3* a sensitivity analysis will be presented (*Figure 4.4*) and it will take into account variations of  $a_{\text{puff}}$  and  $a_{\text{pump}}$ , always considering a limited lithium presence. For what concerns  $a_n$ , instead, since it is an initial condition it is not expected to have any impact on steady-state results and for this reason its variation are not taken into account in the sensitivity analysis (which revolves around the stationary values).

### 4.2.1 Transient evaluation

*Figure 4.2* shows the trends of the five normalized unknowns as a function of the normalized time, where the normalization constants have the same form as the ones introduced for the original model (§3.2.2). In order not to create confusion and to better contextualize the results, a recap of the initial conditions in the reference case is reported in *Table 4.1*. Because of the several orders of magnitude of difference between helium and lithium respective densities, the comparison between dimensionless results only is almost meaningless and these initial conditions must be taken into account.

Nevertheless, it was chosen to show the normalized results in order to better appreciate all the trends in a single graph; for this purpose, it was also necessary to divide by 100 the transient of the normalized lithium ions (the green curve), which indeed at time  $\tilde{t} = 0$  it is 0.01 instead of 1. The motivation for which the

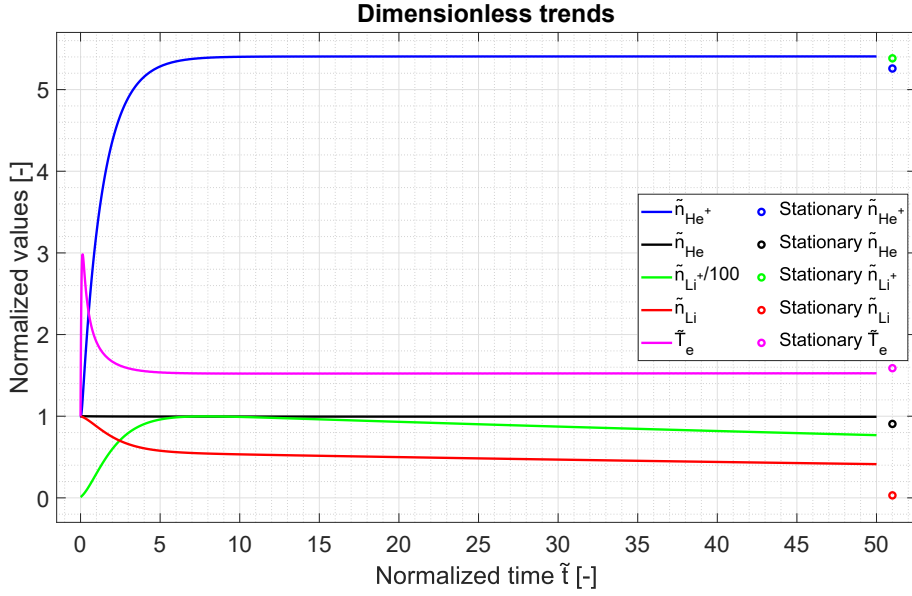


**Figure 4.2:** Transients of the normalized unknowns as a function of the dimensionless time (the normalized lithium ion density is further divided by 100 for illustration purposes). The circles are the stationary values of the respective transients.

$n_{He^0} [\text{cm}^{-3}]$	$1.176 \cdot 10^{13}$
$n_{He^+0} [\text{cm}^{-3}]$	$9.99 \cdot 10^9$
$n_{Li^0} [\text{cm}^{-3}]$	$2.353 \cdot 10^9$
$n_{Li^+0} [\text{cm}^{-3}]$	$1 \cdot 10^7$
$T_{e0} [\text{eV}]$	5
$t_0 [\text{s}]$	$1.867 \cdot 10^{-4}$

**Table 4.1:** Summary of the initial conditions of all the five unknowns plus the time: they are fundamental in order to understand the normalized results.

normalized lithium and helium densities (blue and green curves, respectively) are those with the largest growth lies in their initial conditions themselves. Indeed, both the initial electron density and the percentage of lithium ion density were chosen arbitrarily and, evidently, they were smaller with respect to the steady-state. Additionally, the energy of first ionization for helium is almost five times that of lithium and, consequently, it is much easier to ionize the latter.

The electron temperature is significantly affected by the starting of the LPD operation and the resulting external power injection, but since that energy is spent in ionizing neutral atoms (whose densities decreases, increasing the ion densities), it immediately falls to a level that will be more or less maintained up to steady-state. Connected to this, both the neutral atoms densities decrease with respect to their initial state, since, because of the electron temperature rise, the ionization reaction rates increase and there are more neutrals undergoing ionization processes.

### 4.2.2 Electron heat losses mechanisms

Another very interesting information that can be extracted from a model of this kind is a more detailed evaluation of the dissipation mechanisms of the injected external power. Considering the steady-state situation, there are four main channels that counterbalance  $P_{\text{ext}}$  in order to have a null left-hand side in *Equation (3.11)*: ionization, radiation, wall sink and thermal equilibration. These channels can be further subdivided for the two elements in the LPD, helium and lithium, for a total of eight channels. *Figure 4.3* displays the importance of each channel corresponding to an external power  $P_{\text{ext}} = 540$  W. Taking into account that the y-axis of the graph is logarithmic, it is already evident at first glance how helium and lithium have a strongly different impact on the energy loss: the sum of the helium channels dissipates 99.94% of the total power injected (539.7 W). The motivation behind this disparity mainly lies in the diversity of lithium and helium densities, which is evident multiplying the normalized steady-state values in *Figure 4.2* times the respective initial conditions reported in *Table 4.1*. Nevertheless, one must also take into account the different reaction rates between helium and lithium: analyzing the four dissipation channels it is possible to draw the following conclusions:

- ionization: since the term  $E_{\text{iz}}R_{\text{iz},n}$  for lithium is one order of magnitude larger than for helium, the difference between the two ionization channels (4 orders of magnitude) is mainly due to the neutral helium density being  $10^5$  times the neutral lithium one;
- radiation: the majority of it comes from the radiation of neutral particles (and not from ions). In this case the term  $E_{\text{rad},n}R_{\text{rad},n}$  is two orders of magnitude larger for lithium in comparison to helium; hence the difference in the two dissipation channels is  $\approx 3$  orders of magnitude;

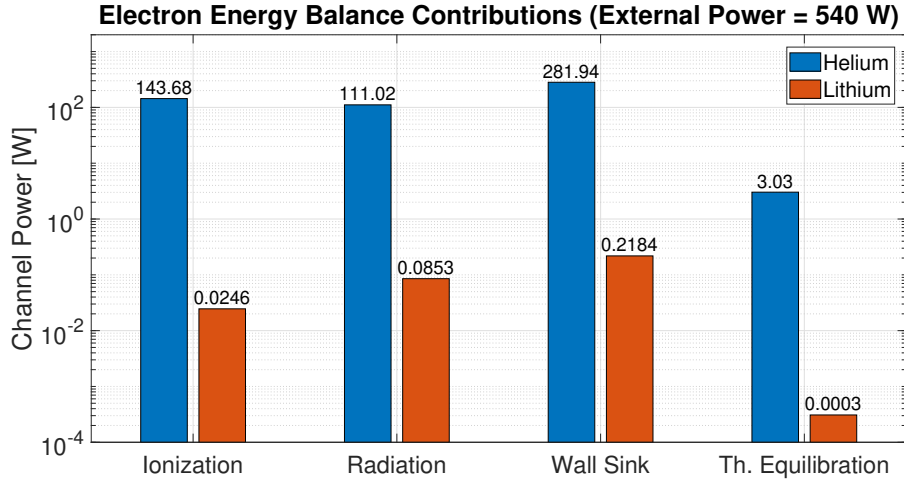


**Figure 4.3:** External power dissipation channels at steady-state: ionization, radiation, wall sink and thermal equilibration for both helium and lithium. Naturally the sum of all channels must give back the total injected power from external, that is 540 W in this case.

- wall sink: this term is related to the transport of ions to the targets and thus it does not depend on neutral densities. Indeed, the difference of 3 orders of magnitude between the helium and lithium ion densities (in favor of the former) reflects in the diversity of the two channels;
- thermal equilibration: because of the higher neutral densities with respect to the ion ones, the leading term in this case is the electron-neutral collision one. As for ionization, the 5 orders of magnitude of difference between helium and lithium neutral densities are decreased by 1 because of the higher reaction rate  $R_{el,n}$  for lithium.

In all four cases, the main reason for the different magnitude of helium and lithium channels lies in the diversity of the densities of the two elements. In some instances this discrepancy is attenuated by the larger ionization, radiation and collision rates of lithium with respect to helium: for this reason it is expected that, if the densities were similar, the majority of electron energy losses would be due to the liquid metal.

### 4.2.3 Sensitivity analysis

Such a 0D model is suitable for a sensitivity analysis to input parameters because of its fast-running nature. For the advancement of the model presented in [71], it can be more interesting to study how the outputs vary when the inputs related

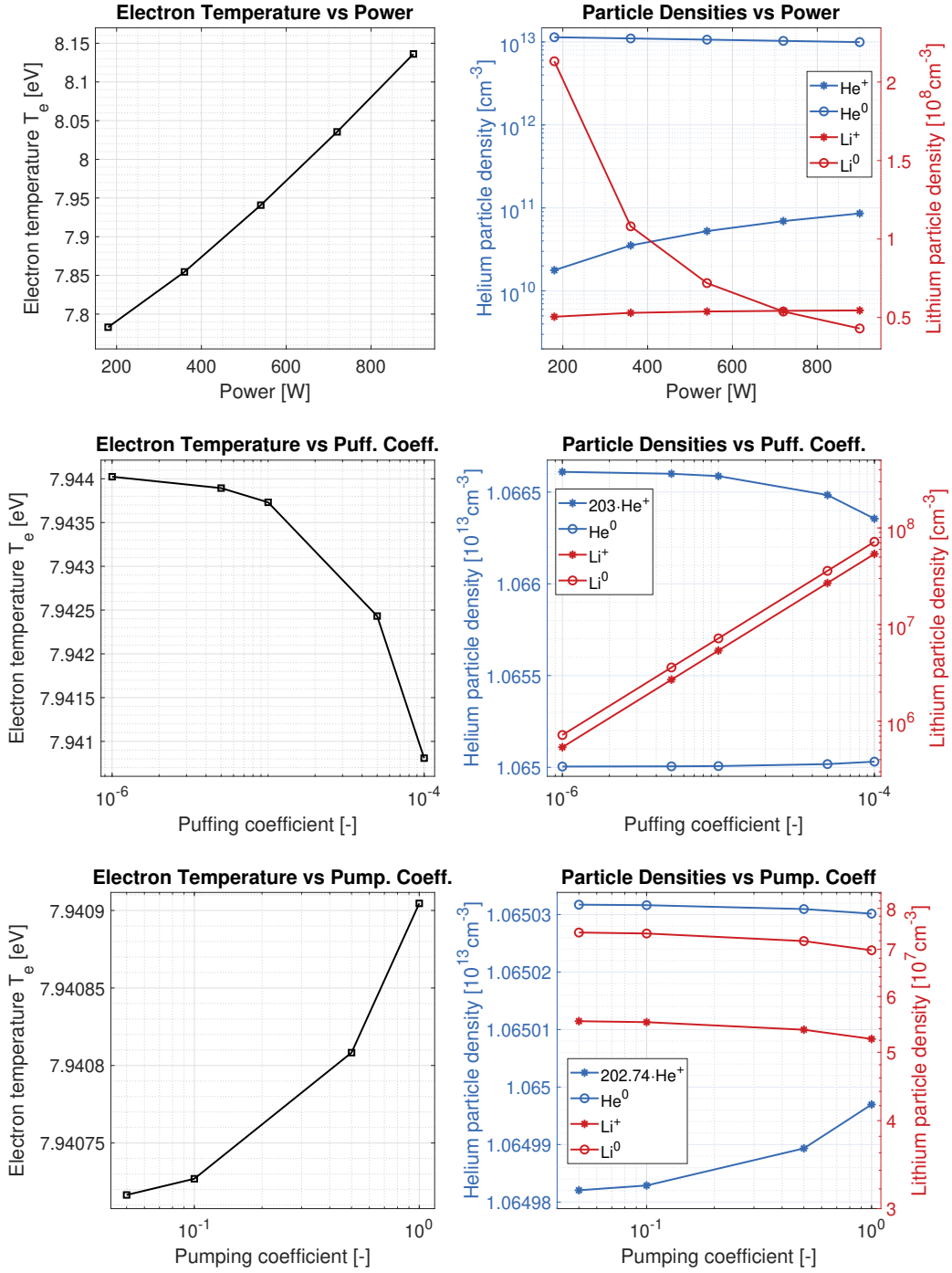


**Figure 4.4:** Sensitivity analysis with respect to external power  $P_{\text{ext}}$ , lithium puffing coefficient  $a_{\text{puff}}$  and lithium pumping coefficient  $a_{\text{pump}}$  (ordered by row). Helium ion density curves in the 2<sup>nd</sup> and 3<sup>rd</sup> rows have a tailored normalization in order to be able to make all the trends clear employing just one graph.

to lithium are changed or when the external power is altered. Specifically, it is possible to vary the coefficients that relate the lithium input parameters (such as its inflow and its pumping speed) to the reference helium ones and the total external power inserted, evaluating how the steady-state values are affected: the summary of this sensitivity study is displayed in *Figure 4.4*.

The two graphs in the first row consider an external power variation.  $P_{\text{ext}}$  directly affects the electron energy balance equation: if it is increased, the steady-state electron temperature will consequently be higher and, in turn, it affects all the reaction rates of the different atomic processes and the speed of the ions going toward the targets (for both species). More precisely, the ionization rates will increase while the recombination ones will decrease and this translates in higher ion densities at the expenses of neutral atoms densities, that will be reduced.

In the second row of *Figure 4.4* the input parameter that is changed is the puffing coefficient  $a_{\text{puff}}$ , while in the third one it is the pumping coefficient  $a_{\text{pump}}$ . Since they are directly acting on the amount of lithium that is, respectively, injected to or taken away from the LPD, the interpretation of the results is somewhat straightforward. When the puffing coefficient is increased, the lithium neutral density follows: because of the increased number of particles, the electron temperature decreases and this implies a reduced number of helium ions, while the neutral helium atom density increases. On the contrary, both lithium densities increases, because the addition of more neutral lithium atoms which can undergo ionization has a stronger effect than the reduction of the ionization reaction rate coefficient. The situation is diametrically opposite when the pumping coefficient is increased: if the particles inside the LPD are reduced (the neutral lithium sink is enhanced), the electron temperature will grow and, correspondingly, helium ions have a larger density at the expenses of the helium neutral atoms. Also the lithium ion density decreases, because the reduction in neutral lithium atoms is more effective than the rise of ionization reaction rate.

For both puffing and pumping coefficient variations, even if by orders of magnitude, the impact on electron temperature and helium densities is extremely limited. In these two cases, to be able to show the trends of helium curves, it was necessary to multiply the helium ion density curves by ad-hoc coefficients in order for helium curves to be sufficiently close, enabling them to show their tiny variations. This is due to the small importance that lithium has in such a model where it is averaged over the whole volume of the LPD. On the contrary, the impact on lithium density is significant and this is because of the direct consequences of the input parameters on lithium populations.

The low impact of lithium in GyM behavior is mainly due to its very low density if compared to helium. The reported outcomes make perfectly sense and they are in line with the expectations stated in *Section 3.3.1*. Indeed, in reality, the liquid

metal atoms have a very non-uniform density inside the LPD, being it much higher close to the LM targets with respect to the center of the device. Because of this, taking a 0D average of the whole volume is not at all relevant to evaluate the LM impact and, as a consequence, the main plasma parameters are only slightly affected by the presence of lithium. This is the main reason that drives toward a change of the domain of the model: by selecting accurately the volume over which parameters are averaged, it is possible to have results which are more physically meaningful.

## 4.3 Increase of Li source

### 4.3.1 Motivations

The studies of lithium impact on the model presented so far have a common root: the lithium input parameters have been kept very small if compared to helium ones. This was done on purpose, since it is physically expected that, averaging over the whole LPD, lithium presence will be extremely small if compared to the main plasma. Indeed, the region where the LM density is the highest in the LPD is in the vapour cloud, right in front of the target: this is also the volume in which the most interesting pieces of physics occur. While the results presented in the previous sections are almost unaffected with respect to the original model, which did not even take lithium into account, it is expected that for higher lithium densities (getting closer to helium ones) it is possible to notice a significant interaction between the plasma and the liquid metal atoms.

The best way to approach this kind of problem would be to change the equations in order to virtually change the average domain under consideration: this procedure will be theoretically described in *Chapter 5* and it will lay the foundations for future developments of this thesis work. An alternative idea is to accurately tune the input parameters of the model already developed in order to simulate the change of domain, but without actually changing the equations. Even if this second method undoubtedly presents many limitations with respect to the former (e.g. ion and neutral temperatures are still assumed constant and equal, charge exchange phenomena are not considered, lack of self-consistency between plasma flux and LM density) it can still be useful to start approaching the physics of plasma-LM interaction from a computational point of view, keeping it simple and exploiting an already developed model.

### 4.3.2 Choice of the input parameters

The input parameters used in this section are summarized in *Table 4.2*. The main change with respect to the reference input variables introduced at the beginning of

$P_{\text{ext}}$ [W]	900
$S_{\text{P,He}}$ [ $\text{Ls}^{-1}$ ]	760
$a_{\text{pump}}$ [-]	1
$\text{Gas}_{\text{in,He}}$ [sccm]	10
$a_{\text{puff}}$ [-]	0.5

**Table 4.2:** Summary of the input parameters used to analyze the impact on the model of a larger lithium concentration.

*Chapter 4* and *Section 4.2* is the increase of the puffing coefficient  $a_{\text{puff}}$  by more than 3 orders of magnitude: from  $10^{-4}$  to 0.5. At the same time, the pumping coefficient and the external power have been increased as well, while the helium inflow has been decreased. The numerical values of these parameters were chosen in order to have a solution reaching a physically meaningful steady-state: following the model equations (§3.3.2), if the particle density is too high, the input external power (which is the only explicit source of the electron energy balance equation) is not sufficient to counterbalance it and the electron temperature will go down abruptly. This will translate in much smaller ionization reaction rates and thus only neutral populations will be present and they will be regulated according to the puffing and pumping fluxes. This is the motivation for which the power and the pumping coefficient have been increased, while the helium gas inflow has been decreased accordingly with the increase of the lithium one and considering that the lithium radiates more than helium (as seen in *Section 4.2.2*).

For what concerns instead the initial conditions, those for the electron temperature and ions densities are kept equal to the previous model (reported in *Table 4.1*), while the He and Li neutral atoms densities have been computed accordingly to what said in *Section 3.3.3*, considering of course the new values for the pumping speed and gas inflow detailed in *Table 4.2*.

### 4.3.3 Transient study

The transients of the model run employing the just-mentioned input parameters are shown in *Figure 4.5*. In order to give an interpretation of the results, it has been chosen to show both the dimensionless and dimensional trends: the former is able to clearly show the general behavior of the functions, while the latter gives a perspective of the orders of magnitude at play. The normalized lithium ion

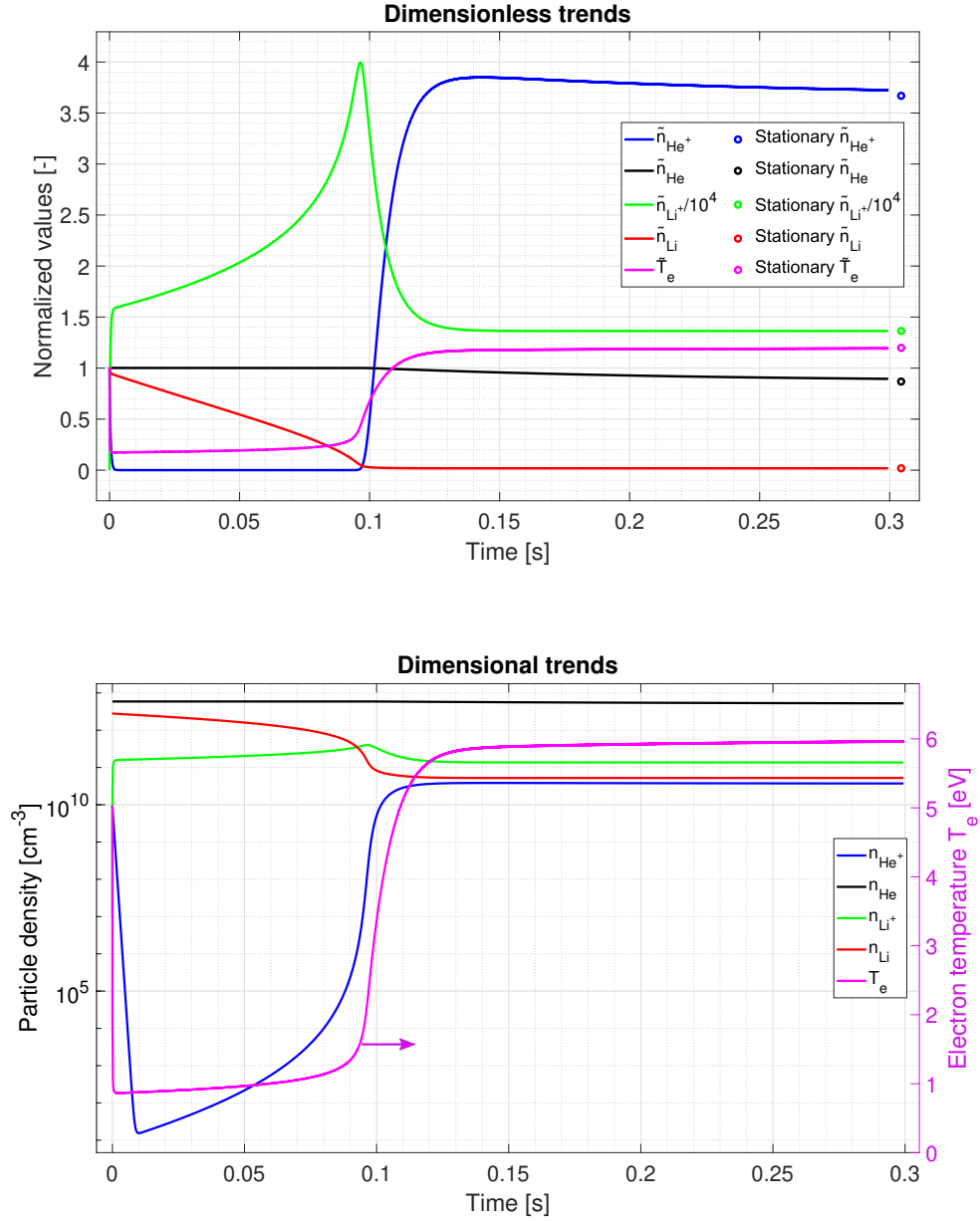


**Figure 4.5:** Transients of the normalized (above) and dimensional (below) unknowns as a function of time [s]. In the dimensionless plot, the normalized lithium ion density has been divided by  $10^4$  for illustration purposes. The circles are the stationary dimensionless values of the respective variables. The magenta curve in the dimensional plot refers to the electron temperature and the arrows highlights that its values must be read on the y-axis on the right.

density has been divided by  $10^4$  for clarity purposes: this arbitrary normalization constant is larger than the one employed in *Figure 4.2*, since, due to the increased puffing coefficient, the lithium is expected to reach much larger densities in this case, notwithstanding the initial conditions (which, for ions, are the same as the previous application of the model in *Section 4.2*).

In the first instants, even if not visible from the picture, the electron temperature has a very small increase because of the appearance of the external power; though, in contrast with what happened before (*Figure 4.2*), in this case the initial neutral lithium density is much higher than before ( $2.94 \cdot 10^{12}$  vs.  $2.35 \cdot 10^9$ ). This means that there are 1000 times more lithium neutral atoms available to become ions and, indeed, lithium ions density increases abruptly. Not only, but the neutral lithium density has also an energy times reaction rate ( $E_{\text{rad},n} R_{\text{rad},n}$ ) much larger than helium and than lithium ions: a such high concentration of neutral Li causes the electron temperature to fall below 1 eV. This kind of temperature drop implies a reduction of the ionization reaction rates (and an increase of recombinations) for both Li and He, but with a crucial difference: while for helium the recombination rate becomes bigger than the ionization one (that becomes almost null), at those electron temperatures the ionization rate for lithium is nevertheless bigger than its recombination counterpart. Thus, before 0.01 s, He ions density falls to  $\approx 10 \text{ cm}^{-3}$ , while Li ions density keeps increasing, even if at a much diminished pace because of the reduced difference between  $R_{\text{iz,Li}}$  and  $R_{\text{rc,Li}}$ .

Following its lowermost value, the electron temperature starts rising, taking advantage of the conversion of neutral lithium atoms into ions: because of the additional electron, neutral atoms can lose more energy via line radiation with respect to the ions. For helium ions density this means that it is reached a point where the ionization reaction rates is again noticeable and this allows it to rise again, also considering the relatively huge helium neutral atoms density. Instead, for what concerns lithium, the increase of electron temperature translates in an escalation of the difference between the ionization and recombination reaction rates, and thus the rate at which lithium neutral atoms become ions is more and more enhanced, as can be seen from the dimensionless plot.

Between 0.09 and 0.1 s, as clearly visible from the dimensional plot, it is reached a point where the lithium ions density overcomes the neutral atoms one and the derivative of lithium ion density with respect to time keeps rising. This growth stops when there is a significant difference between the lithium ions and neutral atoms densities: because of the much smaller number of neutral atoms available to be ionized, the source of *Equation 3.9* decreases as well. At the same time, the electron temperature rises because of the reduced losses caused by neutral lithium particles and, consequently, the helium ions density follows. Even if  $T_e$  reaches values close to the initial conditions, for which the lithium ionization reaction rate is much larger than the recombination one, the situation is very different because

of the disparity in the neutral and charged particles densities, in favor of the latter. In this case, because of the high  $n_{\text{Li}^+}$ , an increment of the temperature influences more the losses due to the transport parallel to the magnetic field lines (depending on  $u_B \simeq \sqrt{T_e/m_i}$ ) than the reaction rates.

As displayed in the dimensionless plot, the curves after 0.3 have basically already reached their steady-state values and their order of magnitude can be directly appreciated from the dimensional graph.

#### 4.3.4 Re-evaluation of the electron heat losses

Exploiting the stationary results from the simulation just run (*Figure 4.5*), it is possible to evaluate once again the importance of the different channels that contribute to dissipate the electron energy, as already reported in *Figure 4.3* (§4.2.2). It is possible to appreciate immediately the differences between the two graphs: not only the lithium contribution is now on the same order of magnitude as the helium one for all the four dissipation channels, but for what concerns radiation and the wall sink it is even larger. With this input parameters, lithium is the species contributing the most in dissipating the external power at steady-state: its channels make up for  $\approx 602$  W out of the injected 900 W (66.88%). Considering all four dissipation channels, the two species can be compared term by term, in a

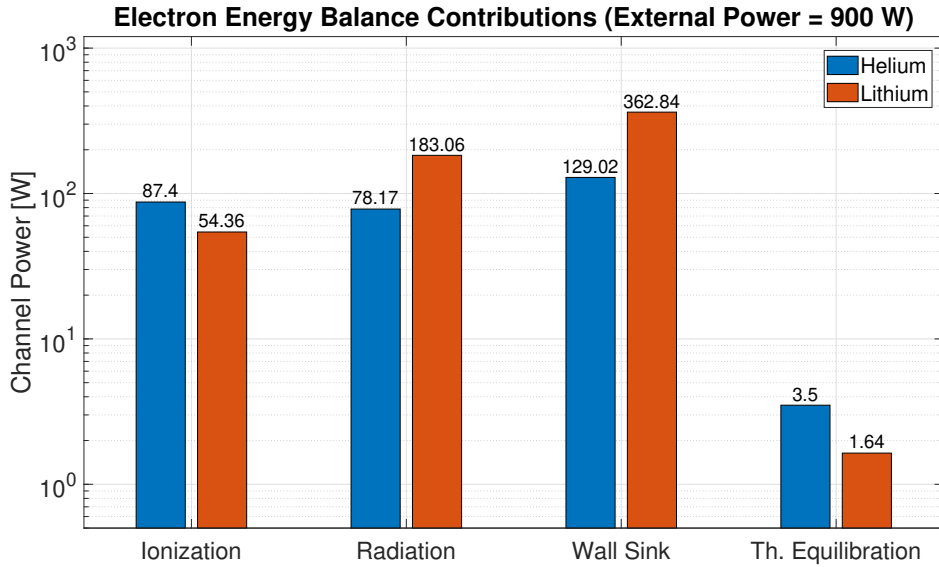


**Figure 4.6:** External power dissipation channels at steady-state for an external power of 900 W, showing the increased impact of lithium following the change of the input parameters.

similar fashion as what has been done in *Section 4.2.2*. Taking into consideration the steady-state values of the five unknowns (whose order of magnitude can be immediately determined from the dimensional plot of *Figure 4.5*), the four channels read:

- ionization: this term depends linearly on the neutral atoms densities of the two species, which is two orders of magnitude bigger for helium. Nevertheless, the term  $E_{iz}R_{iz,n}$  for lithium is almost two orders of magnitude larger than for helium: this implies that the two ionization channels are very close, with the lithium being only slightly smaller;
- radiation: for both species the leading term of this channel is the radiation of neutral particles, but for different reasons: while for lithium the ion and neutral atoms densities are not so different, but the term  $E_{rad,n}R_{rad,n}$  is almost 5 orders of magnitude bigger than the ion counterpart, for helium the main difference lies in the fact that neutral atoms density is more than 100 times the ions one. In this case, the lithium neutral density is  $\approx 100$  times smaller than the helium one, but its radiation term  $E_{rad,Li^0}R_{rad,Li^0}$  is more than two orders of magnitude bigger, leading to a higher contribution with respect to lithium;
- wall sink: this term mainly depends on the ion density and, since the lithium one is around 4 times the helium one (but with a slightly smaller sound speed, due to the higher mass), the lithium wall sink channel is almost 3 times bigger than the helium one;
- thermal equilibration: the leading term for helium is the electron-neutral collision one, while for lithium is the electron-ion one. Because of the disparity in densities and electron-neutral reaction rates  $R_{el,n}$ , the terms are more or less comparable and thus these lithium and helium channels dissipate a similar amount of power (which in any case is much smaller than the other channels mentioned previously).

To summarize, the channels that are lead by neutral particles terms, such as the ionization and radiation ones, are made comparable between the two species because of lithium high reaction rates. Instead, the wall sink accounts only for the ions and thus the lithium prevails because of its larger steady-state ions density. The thermal equilibration process is instead a slightly more complex phenomenon which involves different comparable terms, so no easy answer can be given and each specific case must be evaluated; though, in the range of parameters explored in these sections, it has always been the channel contributing the least.

# Chapter 5

## Future development of the model

After having discussed in the previous chapter the main results considering the 0D LM model introduced in *Section 3.3*, it will be given here a brief theoretical introduction on how the above-mentioned model can be further developed in order to virtually change the domain over which the quantities are averaged.

After describing the theoretical implication of the domain modification (§*5.1*), *Section 5.2* will explain how to change the terms in the already existing equations, while in *Section 5.3* the required additional equations will be added, namely those for the energy balance of neutral and ionic populations of both He and Li. The steps illustrated in this chapter take inspiration from the paper of Marenkov and Pshenov [86], who developed a similar 0D model to evaluate the vapor shielding capabilities of LMs. To conclude, *Section 5.4* will put this model into perspective, highlighting the main criticalities but also stressing its potential usefulness.

### 5.1 Domain modification

In this section it will be analyzed in more detail what the above-mentioned “change of domain” means in relation to the 0D model introduced in the previous chapters and considering the objective one can have in mind. The models introduced in *Chapter 3* referred to global averages of the quantities of interest over the whole volume of the LPD device: while this can be convenient from the viewpoint of the incoming and outgoing particle fluxes, it is almost useless if the objective is to accurately describe the physics of the interaction between the main plasma and the LM vapour cloud. This is because it is expected that the LM density will not be uniform at all inside the LPD: it will be much higher closer to the LM target, while away from it the presence of the liquid metal can be considered negligible. This is

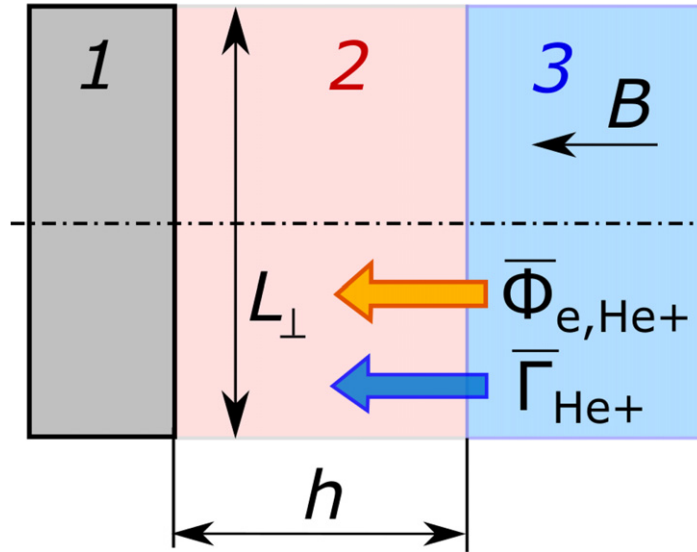


**Figure 5.1:** Schematic representation of the geometry of the new model. The quantities are averaged over the volume of the vapour cloud (2), which is in between the main plasma (3) and the target (1). The impact of the upstream plasma is characterized by an ion flux and the heat fluxes carried by electrons and ions [87].

what motivates a change of the model domain: instead of averaging over the whole LPD, implying the loss of different pieces of physics, it is tempting to take as a domain exactly the vapour cloud volume, or at least to be closer to it. *Figure 5.1* depicts a sketch of the model geometry one can have in mind: the vapour cloud region (2) is the new domain over which quantities are averaged and on one side there is the target (1), while on the opposite there is the main plasma, entering the vapour cloud with certain ion and heat fluxes.  $h$  and  $L_{\perp}$  are the dimensions that define the volume of the vapour cloud. As already discussed while considering *Figure 2.14* in *Section 2.4.2*, the vapour cloud has an oscillatory nature also for what concerns its size: even if, in principle, it is possible to take into account this variation, in the model that will be presented here these two parameters will be taken as fixed for simplicity. Indeed, their values will not influence the physical and qualitative nature of the terms that will be introduced and, in any case, it is possible to make sensitivity studies with different values of the parameters, to understand which fit better with experimental results.

Another important difference with respect to the previous model is that in this case the Debye sheath is not considered anymore as a boundary, but it is included inside the volume over which the average is made (inside 2, considering *Figure 5.1*). Even if the difference between including it or not inside the volume is almost negligible from the spatial point of view, it is absolutely not from the physical

point of view because of its paramount importance in PMI physics, as discussed in *Section 2.1.1*. This will be even clearer when the change of parallel transport terms will be analyzed in the following section.

## 5.2 Adjustments of flux terms

### 5.2.1 Changes on the number of sources and sinks

Because of the change of domain, the terms that will undergo the most changes will be those regarding the incoming and outgoing fluxes:

- the incoming flux of particles will not be anymore the gas injected through a puffing nozzle, but directly the flux of ions from the main plasma;
- there will not be anymore a power coming from the external of the machine, but it will directly come from the main plasma as electron and ion heat fluxes;
- the pumping of neutral atoms can not be taken into account anymore since it happens at the walls, far from the domain considered now: the atom losses will be only due to transport to the target and to cross-field diffusion.

The particle balance equations that are needed have more or less the same form as the previous ones, but they are reported again for the sake of clarity:

$$\frac{dn_{\text{He}^+}}{dt} = R_{\text{iz,He}}n_en_{\text{He}^0} - R_{\text{rc,He}}n_en_{\text{He}^+} + S_{\text{ext}} - L_{\text{tar,He}^+} - L_{\text{CF,He}^+} \quad (5.1)$$

$$\frac{dn_{\text{Li}^+}}{dt} = R_{\text{iz,Li}}n_en_{\text{Li}^0} - R_{\text{rc,Li}}n_en_{\text{Li}^+} - L_{\text{tar,Li}^+} - L_{\text{CF,Li}^+} \quad (5.2)$$

$$\frac{dn_{\text{He}^0}}{dt} = -R_{\text{iz,He}}n_en_{\text{He}^0} + R_{\text{rc,He}}n_en_{\text{He}^+} + S_{\text{rec}} - L_{\text{tar,He}^0} - L_{\text{CF,He}^0} \quad (5.3)$$

$$\frac{dn_{\text{Li}^0}}{dt} = -R_{\text{iz,Li}}n_en_{\text{Li}^0} + R_{\text{rc,Li}}n_en_{\text{Li}^+} + S_{\text{Li}^0} - L_{\text{tar,Li}^0} - L_{\text{CF,Li}^0} \quad (5.4)$$

$$n_e = n_{\text{He}^+} + n_{\text{Li}^+} \quad (5.5)$$

The black terms are those that were already present in the previous model and that are unchanged, since they do not refer to fluxes at the boundaries but to volumetric processes (ionization and recombination). The red terms are particle sources coming from the boundaries of the volume:  $S_{\text{ext}}$  is the external source of plasma ions from the main plasma,  $S_{\text{rec}}$  is the source of neutral helium atoms from the wall due to the recycling phenomenon and  $S_{\text{Li}^0}$  is the source of neutral LM atoms as a result of evaporation and sputtering processes occurring at the target surface. The blue and green terms represent instead particle sinks:  $L_{\text{tar}}$  refers to the losses because of the transport to the target, while  $L_{\text{CF}}$  is due to the cross-field diffusion process. In the

previous model they corresponded, respectively, to  $\Gamma_{i,\text{wall}\parallel} n_i$  and  $\Gamma_{i,\text{wall}\perp} n_i$ , since they were present only for ions. Each of the coloured terms will be now evaluated separately, making comparison with respect to the advanced model introduced in *Section 3.3*.

## 5.2.2 Parallel transport

The term describing the parallel transport to the flux has been previously introduced only for the ions, while the term describing outgoing fluxes of neutral atoms was considering only the action of the pumps. For what concerns ions,  $L_{\text{tar},i}^{\text{old}}$  (proportional the first term in *Equation (3.6)*) can be modified as follows:

$$L_{\text{tar},i}^{\text{old}} = \frac{\alpha u_B A_T}{\text{Vol}_i} n_i \quad \longrightarrow \quad L_{\text{tar},i} = \frac{n_i C_{s,i}}{h}$$

where, hereafter, the right-pointing arrow identifies the process of moving from the model introduced in *Section 3.3* to the one that focuses on the vapor cloud in front of the target and whose volume includes the sheath region. If only one target is considered (and not two, as in GyM), it is easy to see that  $\text{Vol}_i/A_T = h$ , where  $h$  is the thickness of the vapour cloud in the direction parallel to the magnetic field lines (*Figure 5.1*). Additionally, since  $\alpha$  is the ratio of the target plasma density over the point plasma one (referred to the entire LPD), if the point plasma density is now evaluated in the vapour cloud volume the two coincide, implying that  $\alpha \rightarrow 1$ . For what concerns the velocity, it must be considered that the assumption  $T_i = T_n = 0.025$  eV of the previous model is removed here and that the boundary of the domain is not anymore the Debye sheath entrance, but directly the wall. Thus, taking into account that, generalizing the Bohm criterion for two-component plasmas, each ion species has the bulk ion sound velocity at the sheath-presheath interface [88] and bearing in mind that crossing the sheath ions gain a potential energy  $\approx 3T_e$  (*Equation (2.2)*), the velocity of ions at the target is  $C_{s,i} \simeq \sqrt{(T_i + 3T_e)/m_i}$ .

The neutral atoms loss fluxes from the vapour cloud volume are not directly related to the turbomolecular pumps anymore and they can be treated in a similar fashion as ions. For what regards the losses to the target, it can be expressed as:

$$L_{\text{tar},n} = \frac{n_n u_n}{4h}$$

where  $u_n = \sqrt{8T_n/\pi m_n}$  is the neutral atoms thermal speed. This expression for  $L_{\text{tar},n}$  comes from the one-way particle flux density for an ordinary Maxwellian distribution [22].

### 5.2.3 Cross-field diffusion

In the light of the intrinsic differences between the two models, the cross-field diffusion term for the ions, which is the density times the second term in *Equation (3.6)*, is modified as follows:

$$L_{\text{CF},i}^{\text{old}} = \frac{D_{\perp} A_{\text{Lat}}}{\lambda_n \text{Vol}_i} n_i \quad \longrightarrow \quad L_{\text{CF},i} = \frac{n_i}{\tau_i} \approx \frac{D_{\perp}}{L_{\perp}^2} n_i$$

where  $\tau_i$  is the average confinement time of the ion and  $L_{\perp}$  is the transverse (perpendicular to the magnetic field) vapour cloud size. According to Marenkov and Pshenov [86] it can be assumed roughly equal to the characteristic SOL width:  $L_{\perp} \sim \lambda_n$ . The step between the two descriptions is less accurate here because of the uncertainties in the parameters that describe the process of cross-field diffusion; in any case it can be considered valid at least for what concerns a rough estimation. A very similar term can be written for the neutral population, namely:

$$L_{\text{CF},n} = \frac{n_n}{\tau_n} \approx \frac{n_n u_n}{L_{\perp}}$$

The only thing one can be sure of, is that the ions confinement time for ion will be much greater than the neutral one, because of the action of the magnetic field on charged particles.

### 5.2.4 Source terms

Differently with respect to the previous model, there is now a supplier of helium ions into the volume ( $S_{\text{ext}}$ ): while before the particles entering the LPD were neutral and they were ionized at a later time, there is now the possibility that particles get ionized upstream, before entering the vapour cloud volume and thus representing an external flux source. The fraction of ions entering the domain with respect to the total number of particles depends on the ionization degree that the LPD is able to supply and to the confinement that ions are subjected to.

For what regards instead the neutral atoms source terms, a distinction is needed between helium and lithium species: in the first case the source term is due to the recycling phenomena, while for the LM it originates from sputtering and evaporation.  $S_{\text{rec}}$  is treated in an identical way in both models: it is proportional to the number of plasma ions going to the target through a recycling coefficient  $0 < \beta_{\text{rec}} \leq 1$ , yielding:

$$S_{\text{rec}}^{\text{old}} = \beta \frac{\alpha u_{\text{B,He}^+} A_{\text{T}}}{\text{Vol}_i} n_{\text{He}^+} \quad \longrightarrow \quad S_{\text{rec}} = \beta \frac{n_{\text{He}^+} C_{s,\text{He}^+}}{h}$$

In order to describe self-consistently the vapour cloud physics, it is necessary to take into account the target surface temperature  $T_s$ : thanks to it, one can obtain a varying source of neutral LM atoms into the volume and, in principle, it is possible to describe the dynamics of the vapour shielding (depicted in *Figure 2.11*). In the temperature range foreseen for a lithium LMD, the thermal sputtering (§2.1.3) is much larger than the “traditional” physical one and for this reason the latter will be neglected here. Both evaporation and thermal sputtering strongly depend on the surface temperature: the former is usually expressed through the saturated vapour pressure, while the latter can be described through the thermal-model or the adatom evaporation/sublimation one: provided that the target temperature remains below 500 °C (*Figure 2.5*), both models are able to describe the phenomenon since they are fitted to the experimental data. Considering the explicit formulation of both terms as in the work by Abrams et al. [38], it is possible to write:

$$S_{\text{Li}^0} = (L_{\text{tar,He}^+} + L_{\text{tar,Li}^+}) Y_{\text{th}}(T_s) + \frac{J_{\text{ev}}(T_s)}{h}$$

where  $Y_{\text{th}}$  is the thermal sputtering yield and  $J_{\text{ev}}$  is the evaporation flux, both depending on the target temperature  $T_s$  and whose explicit expressions read:

$$Y_{\text{th}}(T_s) = \frac{A}{\sqrt{k_B(T_s + B)}} \exp\left[-\frac{E_{\text{evap}}}{k_B(T_s + B)}\right]$$

$$J_{\text{ev}}(T_s) = \frac{p_{\text{Li}}}{\sqrt{2\pi m_{\text{Li}} k_B T_s}}$$

where  $E_{\text{evap}}$  is the lithium sublimation energy at the melting point (1.59 eV),  $k_B$  is the Boltzmann’s constant, and  $A \approx 0.016$  and  $B \approx 350$  are empirical fitting parameters. The temperature in these formulas is of course expressed in Kelvin. The inclusion of this source term for the LM neutral population is of paramount importance in order to evaluate the physics of the vapour shielding and, especially, its oscillatory nature. As explained in *Section 2.4.2*, a target surface temperature rise implies an increase of the LM source in the vapour cloud region: these additional neutral atoms will provide a good dissipation mechanism mainly through radiation (§4.3.4) and charge exchange processes. Thus, the surface temperature will decrease and this implies a reduction of the neutral lithium source in the domain: at the end this self-consistent process may be able to provide a suitable protection to the target, preventing the high heat flux coming from the main plasma to damage it.

### 5.2.5 Electron energy balance equation

The electron energy balance equation was already present in the previous model and, for what concerns its general form, it does not present differences with respect

to *Equation (3.11)*:

$$\frac{3}{2}n_e \frac{dT_e}{dt} = C_{\text{el},e} - Q_e + Q_{\text{ext},e} - Q_{\text{tar},e} - \frac{3}{2}T_e \frac{dn_e}{dt} \quad (5.6)$$

where  $C_{\text{el},e}$  describes the elastic collisions with the two atomic species,  $Q_e$  is the volumetric electron energy loss function due to ionization, recombination and radiation,  $Q_{\text{ext},e}$  is the external electron energy supplied by the main plasma outside the shielding volume and  $Q_{\text{tar},e}$  is the electron energy lost to the target.

The electron elastic collision term comprehends all the terms already present in *Equation (3.11)*, which can be summarized as:

$$C_{\text{el},e} = \sum_{\alpha} \frac{3m_e}{m_{\alpha}} R_{\text{el},\alpha} n_{\alpha} n_e (T_{\alpha} - T_e)$$

where  $\alpha$  denotes all the 4 possible options: helium and lithium ions or neutral atoms. The same goes for the volumetric electron energy loss term, which is the same as the one that appears in *Equation (3.11)*:

$$\begin{aligned} Q_e = & + E_{\text{iz,He}} R_{\text{iz,He}} n_e n_{\text{He}^{\circ}} + E_{\text{iz,Li}} R_{\text{iz,Li}} n_e n_{\text{Li}^{\circ}} + E_{\text{rad,He}^+} R_{\text{rad,He}^+} n_e n_{\text{He}^+} \\ & + E_{\text{rad,Li}^+} R_{\text{rad,Li}^+} n_e n_{\text{Li}^+} + E_{\text{rad,He}^{\circ}} R_{\text{rad,He}^{\circ}} n_e n_{\text{He}^{\circ}} + E_{\text{rad,Li}^{\circ}} R_{\text{rad,Li}^{\circ}} n_e n_{\text{Li}^{\circ}} \end{aligned}$$

The external source terms are instead different in the two models: while previously it referred to the whole machine, now it is the external flux of energy coming from the main plasma, with the same rationale used to explain the main plasma ions source in *Section 5.2.4*. This term now reads:  $Q_{\text{ext},e} = \Phi_{\text{ext},e}/h$ , where  $\Phi_{\text{ext},e}$  is the energy flux expressed in energy per unit surface.

Also the electron flux to the target is changed because of the inclusion of the Debye sheath inside the domain: the electrostatic potential drop through the sheath and the pre-sheath now occurs inside the volume and, consequently, it is not considered anymore when evaluating the flux at the volume boundary. Thanks to the ambipolarity hypothesis, it is possible to describe  $\Gamma_e$ , the total electron flux at the plasma-sheath interface, as the sum of the fluxes of the two kinds of ions:

$$\Gamma_{e,\text{wall}_{\parallel}} = \Gamma_{\text{He}^+,\text{wall}_{\parallel}} + \Gamma_{\text{Li}^+,\text{wall}_{\parallel}}$$

Thus, it is possible to write:

$$Q_{\text{tar},e} = \gamma_e \Gamma_{e,\text{wall}_{\parallel}} T_e n_e \simeq 2 \Gamma_{e,\text{wall}_{\parallel}} T_e n_e$$

where  $\gamma_e$  is the sheath heat transmission coefficient at the wall, due to the one-way Maxwellian heat flux of electron distribution onto the wall [22]. It is clear how the coefficients  $|eV_s|$  and  $|eV_{ps}|$ , that were previously summed to  $\gamma_e \simeq 2$ , are not present anymore because of the inclusion of the sheath inside the domain.

## 5.3 Additional equations

### 5.3.1 Energy equations

With the objective of studying in detail the vapour shielding phenomenon, it is of fundamental importance to take into account also the charge exchange processes, since they provide an excellent mean to take away the energy from the main plasma ions, which could eventually lead to plasma detachment from the target and to much smaller stresses on it. This is one of the reasons why it is necessary to consider also varying neutral atoms and ions temperatures for both species and it is unrealistic to take them as fixed in time and equal to each other. The equations that must be added to the system of the equations with the already introduced ones are:

$$\frac{3}{2}n_{\text{He}}^+ \frac{dT_{\text{He}}^+}{dt} = C_{\text{el,He}^+} + Q_{\text{at,He}} + Q_{\text{ext,He}^+} - Q_{\text{tar,He}^+} - Q_{\text{CF,He}^+} - \frac{3}{2}T_{\text{He}}^+ \frac{dn_{\text{He}}^+}{dt} \quad (5.7)$$

$$\frac{3}{2}n_{\text{Li}}^+ \frac{dT_{\text{Li}}^+}{dt} = C_{\text{el,Li}^+} + Q_{\text{at,Li}} - Q_{\text{tar,Li}^+} - Q_{\text{CF,Li}^+} - \frac{3}{2}T_{\text{Li}}^+ \frac{dn_{\text{Li}}^+}{dt} \quad (5.8)$$

$$\frac{3}{2}n_{\text{He}}^0 \frac{dT_{\text{He}}^0}{dt} = C_{\text{el,He}^0} - Q_{\text{at,He}} - Q_{\text{tar,He}^0} - Q_{\text{CF,He}^0} - \frac{3}{2}T_{\text{He}}^0 \frac{dn_{\text{He}}^0}{dt} \quad (5.9)$$

$$\frac{3}{2}n_{\text{Li}}^0 \frac{dT_{\text{Li}}^0}{dt} = C_{\text{el,Li}^0} - Q_{\text{at,Li}} - Q_{\text{tar,Li}^0} - Q_{\text{CF,Li}^0} - \frac{3}{2}T_{\text{Li}}^0 \frac{dn_{\text{Li}}^0}{dt} \quad (5.10)$$

where almost all the terms have been introduced previously (for electrons) apart from  $Q_{\text{CF}}$ , which is the energy lost because of cross-field diffusion, and  $Q_{\text{at}}$ , that accounts for the energy exchange between ions and neutral atoms of the same species because of ionization and recombination processes. This last term appears indeed in both the equation of the same species, but with an opposite sign in front: atoms that get ionized are a source for the ion population and at the same time a loss for the neutral one (the opposite holds for recombinations). This term can be easily made explicit:

$$Q_{\text{at},\alpha} = \frac{3}{2}R_{\text{iz},k}n_e n_{\alpha^0} T_{\alpha^0} - \frac{3}{2}R_{\text{rc},\alpha}n_e n_{\alpha^+} T_{\alpha^+}$$

where  $\alpha$  can represent either helium or lithium. This term appears with a positive sign in ions equations, while with a negative sign for neutral atoms equations: it represents the effective energy gain related to the appearance of an additional ion or, on the contrary, the loss associated to the removal of a recombining one.

The elastic collision term for the generic particle  $\alpha$ , which can be either an ion or a neutral atom of both species, reads:

$$C_{\text{el},\alpha} = \sum_{\beta} \frac{3}{2} \frac{\gamma_{\alpha\beta}}{2} R_{\text{el},\alpha\beta} n_{\alpha} n_{\beta} (T_{\beta} - T_{\alpha})$$

where  $\beta$  spans among all the five kinds of particle in the model (of course,  $C_{\text{el},\alpha}$  will go to zero for  $\alpha = \beta$ , since the temperatures are the same).  $\gamma_{\alpha\beta}$  is the fraction of kinetic energy that can be transferred between two colliding particles in an elastic collision (it is between 0 and 1) and it reads:

$$\gamma_{\alpha\beta} = \frac{4m_{\alpha}m_{\beta}}{(m_{\alpha} + m_{\beta})^2}$$

Depending on the combination of  $\alpha$  and  $\beta$ , the reaction rate  $R_{\text{el},\alpha\beta}$  can be related to Coulomb collisions or to ion-neutral collisions. According to [86], the ion-neutral energy transfer between particles of different species (i.e.  $\text{He}^+ - \text{Li}^{\circ}$  or  $\text{He}^{\circ} - \text{Li}^+$ ) are dominated by induced dipole attraction, while by charge exchange processes are dominant if the species is the same, namely  $\text{He}^{\circ} - \text{He}^+$  or  $\text{Li}^{\circ} - \text{Li}^+$  interactions. As a good first approximation, neutral-neutral collisions can be neglected, since they are expected to have a much smaller reaction rate with respect to these processes.

The particle loss terms evaluated previously (i.e.  $L_{\text{tar}}$  and  $L_{\text{CF}}$ ) contribute to the loss of the energy stored in the vapour cloud as well. The term related to cross-field diffusion is very similar to  $L_{\text{CF}}$  and it reads:

$$Q_{\text{CF},\alpha} = \frac{3}{2} \frac{n_{\alpha}}{\tau_{\alpha}} T_{\alpha}$$

where  $\alpha$  stands once again for all the possible ions or neutral atoms of both species and  $\tau_{\alpha}$  can be expressed using the expressions seen previously for  $L_{\text{CF}}$  (§5.2.3), depending on whether a neutral atom or an ion is being evaluated.

For what concerns the particle flux to the target, it is needed a distinction between ions and neutrals because of the presence of the Debye sheath inside the domain, which is able to accelerate ions that will consequently leave the model domain with a higher energy with respect to the case in which the sheath entrance is treated as a boundary. According to [22] the ion heat fluxes at the wall are:

$$Q_{\text{tar},i} = (2T_i + 3T_e)L_{\text{tar},i}$$

where the first term in the parentheses represents the power flux impacting the sheath edge (which is the same as for neutral atoms), while the second one denotes the amplification due to the acceleration of the ions inside the sheath, which occurs at the expense of the electron energy. The factors “2” and “3” are approximated and they are assumed equal to the ones used in the one-species case [86]. Since the neutrals are not accelerated, their expression simply reads:

$$Q_{\text{tar},n} = 2T_n L_{\text{tar},i}$$

Even if, in principle, eroded atoms from the target should be considered as an energy source in the LM equations, their surface temperature is much smaller than that of the plasma particles and so it can be a good approximation to neglect it.

### 5.3.2 Target surface temperature equation

The link that allows a self-consistent description of the vapor shielding phenomenon is the addition of an equation describing the target surface temperature evolution over time to the system of equations composed by *Equations* from (5.1) to (5.10). Such connection could be a 1D thermal conductivity equation for the temperature inside the solid target beyond the LM layer:

$$\frac{\partial T_s}{\partial t} = \chi \frac{\partial^2 T_s}{\partial x^2} \quad (5.11)$$

Of course, apart from an initial condition, this equation needs two boundary conditions. While on the coolant side of the target it could be thought to apply a Dirichlet or a Robin boundary condition, on the surface that faces the plasma a Neumann one could be used, exploiting the heat flux at the interface with the plasma ( $\Phi_s$ ):

$$k \frac{\partial T_s}{\partial x} \Big|_{x=0} = \Phi_s = \left[ \sum_{\beta} Q_{\text{tar},\beta} + L_{\text{tar},\text{Li}^+} (E_{\text{iz},\text{Li}} + E_{\text{evap}}) + L_{\text{tar},\text{He}^+} E_{\text{iz},\text{He}} \right. \\ \left. + L_{\text{tar},\text{Li}^0} E_{\text{evap}} - S_{\text{Li}^0} E_{\text{evap}} \right] \cdot h - \Phi_{\text{rad},s} + \gamma_{\text{rad}} \Phi_{\text{rad},\text{Vol}}$$

where  $x = 0$  corresponds to the plasma-target interface and  $\beta$  is in turn  $e$ ,  $\text{He}^+$ ,  $\text{Li}^+$ ,  $\text{He}^0$  or  $\text{Li}^0$ .  $\Phi_s$  accounts for the energy delivered to the target by the impinging particles, the potential energy released due to recombinations occurring at the target, the latent heat freed to the target due to the sticking of the vaporized ions and the loss terms due to the evaporation of target atoms and radiation phenomena. The formulation inside the parentheses is correct only under the assumption that recombination phenomena release exactly  $E_{\text{iz}}$  to the surface, therefore neglecting phenomena such as secondary electron emission and the formation of excited atoms or photon emission following a recombination.  $\Phi_{\text{rad},s}$  and  $\Phi_{\text{rad},\text{Vol}}$  refer, respectively, to the gray-body radiation of the target itself and to the volumetric radiation that occur inside the domain (it comprehends all the radiation terms that were present inside  $Q_e$  in *Equation* (5.6)). Of course, not all the plasma radiation returns to the target and for this reason  $\Phi_{\text{rad},\text{Vol}}$  is multiplied times  $\gamma_{\text{rad}}$ , which is the radiation fraction that contributes to heat the target surface. In most cases, the gray-body radiation term can be neglected, since it is an order of magnitude smaller than evaporative cooling.

## 5.4 Main issues and potentialities

Even if, how explained in *Section* 5.1, a model of this kind may be suitable to describe the oscillatory nature of the vapour shielding phenomenon, it presents

some issues that derive from the increased complexity with respect to the one introduced in *Section 3.3*. Apart from the obvious increment in the number of equations and the addition of some terms, which contribute to make this model heavier from the computational perspective than the previous one, one must also consider the modification of the terms which were already present. For instance, the uncertainty in the source and sink terms is now much greater: while before it was much easier to measure the number of neutral plasma particles injected inside the chamber using a puffing nozzle, now it is very difficult to evaluate terms such as  $S_{\text{ext}}$ ,  $Q_{\text{ext},e}$  or  $Q_{\text{ext,He}^+}$ . The same is true for the neutral atoms losses, which previously were mainly due to pumping (and ionizations) while in this model it is needed to accurately estimate their confinement time for cross-field diffusion process. An additional source of uncertainty is the size itself of the domain, as explained in *Section 5.1*.

Because of these reason it may be needed to have more precise and reliable experimental data on the vapour cloud that develops in front of the target, in order to be able to better characterize the source and sink terms in the model. Alternatively, one could proceed making sensitivity studies, evaluating how much certain parameters can impact the model and how: this is crucial in order to better understand the underlying physical processes that drive the vapour shielding mechanism.

In any case, it is normal that a more physically complete model has larger uncertainties, because of the intrinsic addition of new terms or equations that could better explain some phenomena. This is no exception since, thanks to this model, it is theoretically possible to better describe and characterize the oscillatory nature of such an important physical phenomenon as the vapour shielding, that will be one of the keys in determining the success of LMD technologies for future fusion power plants.



## Chapter 6

# Conclusions and perspectives

Despite all its issues and criticalities, nuclear fusion energy represents an extremely important opportunity for a more sustainable future and thus it is worth to keep pursuing it. In order to do so, one of the problems to be solved regards the dissipation of the high heat fluxes on the divertor plates, which becomes prohibitive for current technologies if considering future fusion power plants or the European DEMO. Arguably the most promising way to tackle this problem is to adopt divertors made of liquid metals, which have a self-healing nature and are able to produce a vapour cloud in front of the target that is able to dissipate a relevant fraction of the energy before it can reach the surface. A very convenient way to study this phenomenon is to exploit linear plasma devices, which allow for easy diagnostic access and reproducibility of the experiments. In this respect, studies conducted in Pilot-PSI showed that the vapour shielding phenomenon has the intrinsic characteristic of being oscillatory in time [49].

In the framework of this thesis, it was exploited a preexisting 0D model developed by Tonello et al. [71] to study helium plasmas inside the linear plasma device GyM. The objective was to improve it in order to take into consideration also the presence of the liquid metal (lithium) and to study its interaction with the main plasma. Such refined model, once proven to be coherent with the original model, was then used to study the impact of lithium on the plasma behaviour. The simulation run with input parameters closer to the physical situation (small amounts of liquid metal inside the LPD, since the 0D averages are made over the whole device) lead to very small variations with respect to the original model, but it was nevertheless useful to confirm the correct implementation of the equations since it yielded physically meaningful results.

Successively the lithium input parameters have been modified in order to increase its density inside the plasma chamber up to levels comparable with the helium ones. Even if this may not be physically representative, it was useful to make a first computational study on the interaction between the main plasma and the liquid metal populations, in order to understand which terms in the equations play the most important roles and which do not.

Apart from the main issues related to the intrinsic employment of a 0D model (e.g. the disregard of all the phenomena that are strongly dependent on space), another point in which it could be improved in the future is in the evaluation of the reaction rates. For instance, for the ion-electron reaction rates it was used a formulation similar to the one exploited in [71], but with the addition of the LM the plasma has become multicomponent and so the term may need a better characterization.

To conclude this thesis work, it was analyzed in some detail how the domain of the 0D model could be changed in order to focus only on the vapour cloud volume. By doing so, the focus would be right on the portion of the linear plasma device that is important to study the vapor shielding phenomenon, so it goes without saying that in this case the volumetric average would be much more physically meaningful. The theoretical step to reach this kind of model is to remove the assumption on the constant neutral atoms and ions temperatures for both species and to consider the target surface as an unknown that varies in time: in this way it is possible to include crucial processes inherent to the vapor shielding and to describe the self-consistent nature of the phenomenon.

A natural and reasonable future development of this work is the employment of the system of equations developed for a 0D model that takes into consideration only the vapour cloud volume. By doing so it is possible, in principle, to computationally model the oscillatory nature of the vapor shielding: this would open up the possibility of investigating it exploiting a fast-running 0D computational model, which allows to easily make sensitivity studies and to quickly establish the most significant terms that drive the phenomenon. A deep understanding in this respect will in turn be useful to better evaluate how liquid metal divertors could be implemented in future tokamaks, hopefully solving the power exhaust issue.

# List of Figures

1.1	Total primary energy supply by fuel, 1971 and 2019 [1]. . . . .	2
1.2	U.S. capacity factors by energy production technology in 2017 [3]. . .	3
1.3	Mortality rate (deaths per TWh) for different technologies [4]. . . .	4
1.4	Average binding energy per unit nucleon versus the mass number. . .	7
1.5	Cross-section of different kinds fusion reactions as a function of the energy of one of the two reactants (left). Cross section for various processes induced by neutrons as a function of neutron energy in the thermal spectrum (right). . . . .	8
1.6	Different kinds of plasmas that can be found in the universe as a function of particle density $n$ and temperature $T$ [8]. . . . .	12
1.7	Triple products of fusion experiments up to now in comparison to curves needed to reach, from top to bottom, ignition conditions, $Q=1$ or $Q=0.1$ (in red) [11]. . . . .	15
1.8	Magnetic confinement of a plasma in a tokamak [12]. . . . .	18
1.9	Schematic representation of the tokamak (left) and stellarator (right) devices, with a focus on their magnetic coils configurations [14]. . .	19
1.10	The European roadmap in a nutshell [5]. . . . .	21
2.1	Schematic illustration of the complex, synergistic and inherently multiscale surface interactions occurring at the material surface in a realistic magnetic fusion plasma environment [20]. . . . .	24
2.2	Simplified view of the presheath and sheath regions when the magnetic field is not perpendicular to the wall [23]. . . . .	26
2.3	Schematic illustration of the re-direction momentum from an incident ion to the backward direction, resulting in sputtering [24]. . . . .	28
2.4	Normal incidence physical sputtering yields for deuterium ions impinging on Be, C and W surfaces, calculated with the TRIM.SP code [22]. . . . .	29

2.5	Measured thermal sputtering yields for 50 eV D→Li bombardment in PISCES-B device as a function of the lithium temperature (triangles) and the correspondingly fitted curves for the thermal-spike and adatom evaporation/sublimation models (red and blue curves, respectively) [28]. . . . .	32
2.6	ADAS library [39] data of ionization and recombination rates of hydrogen and helium for an electron densities $n_e = 10^{20} \text{ m}^{-3}$ [40]. . . . .	35
2.7	Loss function data from the ADAS data base (solid lines) [39]. Dashed lines show instead the Bremsstrahlung radiation. Legend ordering (from top to bottom and then from left to right) corresponds to increasing atomic charges $Z$ . Colours have been used twice in order not to use too similar ones, improving legibility. Elements are recognizable in the graph considering the dashed lines, since the Bremsstrahlung radiation increases with $Z$ . Thus, for example, the hydrogen is the first red curve starting from the bottom while the silicon is the second one [41]. . . . .	36
2.8	A JET-size plasma in the limiter configuration. The LCFS is defined by the leading edge of the limiter [22]. . . . .	40
2.9	Sketch of the tokamak divertor configuration with a single X-point (which has been the most used one up to now). Field lines in the scrape-off layer (in orange) are directed downward to the divertor plates thanks to an external magnetic field [42]. . . . .	41
2.10	Schematic drawing of Pilot-PSI and of a LM sample design [49]. . . . .	45
2.11	Time-cycle of dynamical vapour shielding: the boxes indicate the different phases during each cycle [40]. . . . .	48
2.12	A comparison between experiment and ANSYS simulations of the central surface temperature evolution of liquid Sn and solid Mo for $q_{\text{ref}} = 16 \text{ MW/m}^2$ . Due to vapour shielding, the steady-state Sn temperature reduces significantly compared to the conduction-based model that does not consider it. [54]. . . . .	49
2.13	Temperature of the target surface center after 20 s of plasma exposure for liquid Sn and solid Mo. The lines are drawn to guide the eye. The surface temperature of liquid Sn is almost independent of $q_{\text{ref}}$ in the given parameter space. The data point for Mo at 22 MW/m <sup>2</sup> had a 5 s shot duration to prevent melting the target. [54]. . . . .	50

2.14	Vapour shielding dynamics. Value of the surface temperature at the target centre (a) and edge (b) and Sn emission (c–e) between 17.25 and 18 seconds after initiating a 22.0 MW/m <sup>2</sup> He discharge. Three characteristic phases within a typical oscillation period are indicated by the roman numerals I–III and are highlighted by different motifs. (c), (d) and (e) show, respectively, the total line-integrated intensity at 425.5 nm, the penetration into the upstream plasma and the radial extent of the vapour cloud [49]. . . . .	51
2.15	Evaporation rates of Sn and Li as a function of temperature. The inset highlights the typical particle flux at the target surface in Pilot-PSI and Magnum-PSI [40]. . . . .	53
2.16	Schematic view of a liquid lithium divertor system. Four different evaporation chamber types are shown: (a) lithium pool; (b) wick; (c) wick and circulation pump; (d) lithium pool and circulation pump [64].	56
2.17	Partially disassembled titanium-zirconium-molybdenum (TZM) alloy target (a) to show how lithium is transported from the reservoir via the whicks across the surface, due to capillary forces. The TZM target is filled with lithium and it is covered by a mesh layer, clamped between the outer two layers of the target (b) [65]. . . . .	57
2.18	Schematic poloidal cross-section of a lithium vapor box divertor [69].	58
3.1	a) 3D CAD image of GyM, highlighting its main components; b) blocks summarizing the main elements of the 0D model; c) schematic representation of the global LPD domain, considering the sources and sinks in the plasma balance equations; fluxes through the point domain boundaries, atomic processes and the externally supplied power [71]. . . . .	65
4.1	Magnitudes of the error for the three common unknowns (electron temperature, helium ions density and helium neutrals density) between the advanced and the original model. . . . .	76
4.2	Transients of the normalized unknowns as a function of the dimensionless time (the normalized lithium ion density is further divided by 100 for illustration purposes). The circles are the stationary values of the respective transients. . . . .	78
4.3	External power dissipation channels at steady-state: ionization, radiation, wall sink and thermal equilibration for both helium and lithium. Naturally the sum of all channels must give back the total injected power from external, that is 540 W in this case. . . . .	80

4.4	Sensitivity analysis with respect to external power $P_{\text{ext}}$ , lithium puffing coefficient $a_{\text{puff}}$ and lithium pumping coefficient $a_{\text{pump}}$ (ordered by row). Helium ion density curves in the 2 <sup>nd</sup> and 3 <sup>rd</sup> rows have a tailored normalization in order to be able to make all the trends clear employing just one graph. . . . .	81
4.5	Transients of the normalized (above) and dimensional (below) unknowns as a function of time [s]. In the dimensionless plot, the normalized lithium ion density has been divided by $10^4$ for illustration purposes. The circles are the stationary dimensionless values of the respective variables. The magenta curve in the dimensional plot refers to the electron temperature and the arrows highlights that its values must be read on the y-axis on the right. . . . .	85
4.6	External power dissipation channels at steady-state for an external power of 900 W, showing the increased impact of lithium following the change of the input parameters. . . . .	87
5.1	Schematic representation of the geometry of the new model. The quantities are averaged over the volume of the vapour cloud (2), which is in between the main plasma (3) and the target (1). The impact of the upstream plasma is characterized by a an ion flux and the heat fluxes carried by electrons and ions [87]. . . . .	90

# List of Tables

4.1	Summary of the initial conditions of all the five unknowns plus the time: they are fundamental in order to understand the normalized results. . . . .	78
4.2	Summary of the input parameters used to analyze the impact on the model of a larger lithium concentration. . . . .	84



# Bibliography

- [1] IEA. *Total Primary Energy Supply by Fuel, 1971 and 2019*. <https://www.iea.org/data-and-statistics/charts/total-primary-energy-supply-by-fuel-1971-and-2019> (cit. on p. 2).
- [2] N. Adger et al. *Climate Change 2007: Impacts, Adaptation and Vulnerability*. Intergovernmental Panel on Climate Change, 2007. ISBN: 978-0-521-88009-1 (cit. on p. 2).
- [3] U. S. Energy Information Administration. *Capacity Factors by Fuel Type, 2017*. <https://www.eia.doe.gov/resources/statistics/capacity-factors-by-fuel-type> (cit. on p. 3).
- [4] B. W. Brook et al. «Why Nuclear Energy is Sustainable and has to be Part of the Energy Mix». In: *Sustainable Materials and Technologies* 1-2 (Dec. 2014), pp. 8–16. DOI: [10.1016/j.susmat.2014.11.001](https://doi.org/10.1016/j.susmat.2014.11.001) (cit. on p. 4).
- [5] EUROfusion. *European Research Roadmap to the Realisation of Fusion Energy*. 2018. ISBN: 978-3-00-061152-0 (cit. on pp. 5, 17, 20–22, 33, 42, 44, 64).
- [6] ITER website. <https://www.iter.org> (cit. on pp. 5, 20).
- [7] R. J. Pearson et al. «Tritium Supply and Use: a Key Issue for the Development of Nuclear Fusion Energy». In: *Fusion Engineering and Design* 136 (2018), pp. 1140–1148. DOI: [10.1016/j.fusengdes.2018.04.090](https://doi.org/10.1016/j.fusengdes.2018.04.090) (cit. on p. 8).
- [8] Z. Donkó et al. *Strongly Coupled Plasma Liquids*. 2007. URL: [https://www.researchgate.net/publication/2215721\\_Strongly\\_Coupled\\_Plasma\\_Liquids](https://www.researchgate.net/publication/2215721_Strongly_Coupled_Plasma_Liquids) (cit. on p. 12).
- [9] H. Cohen. «Table of Temperatures, Power Densities, Luminosities by Radius in the Sun». In: *Contemporary Physics Education Project* (1998). URL: [http://webarchive.loc.gov/all/20011129122524/http://fusedweb.llnl.gov/cpep/chart\\_pages/5.plasmas/sunlayers.html](http://webarchive.loc.gov/all/20011129122524/http://fusedweb.llnl.gov/cpep/chart_pages/5.plasmas/sunlayers.html) (cit. on p. 13).
- [10] J. D. Lawson. «Some Criteria for a Power Producing Thermonuclear Reactor». In: *Proceedings of the Physical Society. Section B* 70.1 (Jan. 1957), pp. 6–10. DOI: [10.1088/0370-1301/70/1/303](https://doi.org/10.1088/0370-1301/70/1/303) (cit. on p. 14).

- 
- [11] P. Norajitra. «Divertor Development for a Future Fusion Power Plant». In: *KIT Scientific Publishing* (2011). DOI: [10.5445/KSP/1000024270](https://doi.org/10.5445/KSP/1000024270) (cit. on p. 15).
- [12] G. Goué. «Nuclear Fusion Reactors: Safety and Radiation Protection Considerations for Demonstration Reactors that Follow the ITER Facility». In: *Institut de Radioprotection et de sûreté nucléaire* (2017). ISSN: 2117-7791. URL: [https://www.irsn.fr/EN/Research/publications-documentation/Scientific-books/Documents/ITER-VA\\_web\\_non\\_imprimable.pdf](https://www.irsn.fr/EN/Research/publications-documentation/Scientific-books/Documents/ITER-VA_web_non_imprimable.pdf) (cit. on p. 18).
- [13] J. P. Freidberg. *Plasma Physics and Fusion Energy*. Cambridge University Press, 2007. ISBN: 978-0521851077 (cit. on p. 18).
- [14] C. Brandt - Max-Planck Institut für Plasmaphysik. URL: <https://www.ipp.mpg.de/en> (cit. on p. 19).
- [15] I. E. Tamm. «Theory of the Magnetic Thermonuclear Reactor, Part I». In: *Plasma Physics and the Problem of Controlled Thermonuclear Reactions* (1951), pp. 3–19. DOI: [10.1007/978-3-642-74626-0\\_16](https://doi.org/10.1007/978-3-642-74626-0_16) (cit. on p. 19).
- [16] A. D. Sakharov. «Theory of the Magnetic Thermonuclear Reactor, Part II». In: *Soviet Physics Uspekhi* 34 (1991), pp. 378–382. DOI: [10.1070/pu1991v034n05abeh002493](https://doi.org/10.1070/pu1991v034n05abeh002493) (cit. on p. 19).
- [17] I. E. Tamm. «Theory of the Magnetic Thermonuclear Reactor, Part III». In: *Plasma Physics and the Problem of Controlled Thermonuclear Reactions (translated)* (1951), pp. 31–41. DOI: [10.1007/978-3-642-74626-0\\_16](https://doi.org/10.1007/978-3-642-74626-0_16) (cit. on p. 19).
- [18] L. Spitzer. «The Stellarator Concept». In: *The Physics of Fluids* 1.4 (July 1958), pp. 253–264. DOI: [10.1063/1.1705883](https://doi.org/10.1063/1.1705883) (cit. on p. 19).
- [19] P. H. Rebut. «The Joint European Torus (JET)». In: *The European Physical Journal H* 43 (Dec. 2018), pp. 459–497. DOI: [10.1140/epjh/e2017-70068-y](https://doi.org/10.1140/epjh/e2017-70068-y) (cit. on p. 20).
- [20] B. D. Wirth et al. «Fusion materials modeling: Challenges and opportunities». In: *MRS Bulletin* 36.3 (2011), pp. 216–222. DOI: [10.1557/mrs.2011.37](https://doi.org/10.1557/mrs.2011.37) (cit. on p. 24).
- [21] F. F. Chen. *Introduction to Plasma Physics and Controlled Fusion*. Third Edition. Springer, 2015. ISBN: 978-3-319-22309-4 (cit. on p. 25).
- [22] P. C. Stangeby. *The Plasma Boundary of Magnetic Fusion Devices*. en. Plasma Physics Series. Bristol ; Philadelphia: Institute of Physics Pub, 2000. ISBN: 978-0-7503-0559-4 (cit. on pp. 26–29, 40, 42, 92, 95, 97).

- [23] R. Chodura. «Plasma Flow in the Sheath and the Presheath of a Scrape-off Layer». In: *Physics of Plasma - Wall Interactions in Controlled Fusion*. Ed. by D. E. Post and R. Behrisch. Boston, MA: Springer US, 1986, pp. 99–134. ISBN: 978-1-4757-0067-1. DOI: [10.1007/978-1-4757-0067-1\\_4](https://doi.org/10.1007/978-1-4757-0067-1_4) (cit. on p. 26).
- [24] G. S. Was. *Fundamentals of Radiation Materials Science: Metals and Alloys*. Springer, 2007. ISBN: 978-3-540-49471-3 (cit. on pp. 27, 28, 30).
- [25] W. Eckstein. «Physical Sputtering and Reflection Processes in Plasma-Wall Interactions». In: *Journal of Nuclear Materials* 248 (Sept. 1997), pp. 1–8. DOI: [10.1016/S0022-3115\(97\)00109-8](https://doi.org/10.1016/S0022-3115(97)00109-8) (cit. on p. 28).
- [26] J. Bohdansky. «A Universal Relation for the Sputtering Yield of Monatomic Solids at Normal Ion Incidence». In: *Nuclear Instruments and Methods in Physics Research Section B: Beam Interactions with Materials and Atoms* 2.1 (1984), pp. 587–591. DOI: [10.1016/0168-583X\(84\)90271-4](https://doi.org/10.1016/0168-583X(84)90271-4) (cit. on p. 28).
- [27] W. Eckstein et al. *Sputtering Data*. Garching: Max-Planck-Institut für Plasma-physik: (IPP 9/82), 1993 (cit. on p. 29).
- [28] T. W. Abrams. «Erosion and Re-Deposition of Lithium and Boron Coatings under High-Flux Plasma Bombardment». Ph.D. dissertation. Princeton University, 2015. URL: <https://dataspace.princeton.edu/handle/88435/dsp01jm214r372> (cit. on pp. 30–32).
- [29] J. P. Allain et al. «Collisional and Thermal Effects on Liquid Lithium Sputtering». In: *Physical review. B, Condensed matter and materials physics* 76.20 (2007). DOI: [10.1103/PhysRevB.76.205434](https://doi.org/10.1103/PhysRevB.76.205434) (cit. on pp. 30, 31).
- [30] R. P. Doerner et al. «Particle-Induced Erosion of Materials at Elevated Temperature». In: *Journal of applied physics* 95.8 (2004), pp. 4471–4475. DOI: [10.1063/1.1687038](https://doi.org/10.1063/1.1687038) (cit. on p. 30).
- [31] T. W. Morgan et al. «Interaction of a Tin-Based Capillary Porous Structure with ITER/DEMO Relevant Plasma Conditions». In: *Journal of nuclear materials* 463 (2015), pp. 1256–1259. DOI: [10.1016/j.jnucmat.2014.11.085](https://doi.org/10.1016/j.jnucmat.2014.11.085) (cit. on p. 30).
- [32] H. Maier et al. «Tungsten Erosion under Combined Hydrogen/Helium High Heat Flux Loading». In: *Physica scripta* T159.1 (2014), p. 14019. DOI: [10.1088/0031-8949/2014/T159/014019](https://doi.org/10.1088/0031-8949/2014/T159/014019) (cit. on p. 30).
- [33] P. Sigmund. «Energy density and time constant of heavy-ion-induced elastic-collision spikes in solids». In: *Applied Physics Letters* 25.3 (1974), pp. 169–171. DOI: [10.1063/1.1655425](https://doi.org/10.1063/1.1655425) (cit. on p. 30).
- [34] P. Sigmund. «Theory of Sputtering. I. Sputtering Yield of Amorphous and Polycrystalline Targets». In: *Physical review* 184.2 (1969), pp. 383–416. DOI: [10.1103/PhysRev.184.383](https://doi.org/10.1103/PhysRev.184.383) (cit. on p. 31).

- [35] S. Arrhenius. «Über Die Dissociationswärme Und Den Einfluss Der Temperatur Auf Den Dissociationsgrad Der Elektrolyte». In: *Zeitschrift für Physikalische Chemie* 4U.1 (1889), pp. 96–116. DOI: [10.1515/zipch-1889-0408](https://doi.org/10.1515/zipch-1889-0408) (cit. on p. 31).
- [36] D. E. Post and R. Behrisch. *Physics of Plasma - Wall Interactions in Controlled Fusion*. Boston, MA: Springer US, 1986. ISBN: 978-1-4757-0067-1 (cit. on p. 32).
- [37] J. Rothet et al. «Recent Analysis of Key Plasma Wall Interactions Issues for ITER». In: *Journal of nuclear materials* 390 (2009), pp. 1–9. DOI: [10.1016/j.jnucmat.2009.01.037](https://doi.org/10.1016/j.jnucmat.2009.01.037) (cit. on p. 33).
- [38] T. Abrams et al. «Erosion of Lithium Coatings on TZM Molybdenum and Graphite during High-Flux Plasma Bombardment». In: *Fusion Engineering and Design* 89.12 (Dec. 2014), pp. 2857–2863. DOI: [10.1016/j.fusengdes.2014.06.005](https://doi.org/10.1016/j.fusengdes.2014.06.005) (cit. on pp. 33, 94).
- [39] H. P. Summers. *The ADAS User Manual, Version 2.6*. 2004. URL: <http://www.adas.ac.uk/> (cit. on pp. 35, 36, 66, 71).
- [40] G. G. van Eden. «Vapour Shielding of Liquid Metal Walls in Nuclear Fusion Devices». Ph.D. dissertation. Technische Universiteit Eindhoven, 2018. URL: [https://pure.tue.nl/ws/files/109907254/PhD\\_thesis\\_vanEden.pdf](https://pure.tue.nl/ws/files/109907254/PhD_thesis_vanEden.pdf) (cit. on pp. 35, 44, 45, 48, 53).
- [41] H. Lux et al. «Impurity Radiation in DEMO systems modelling». In: *Fusion Engineering and Design* 101 (Dec. 2015), pp. 42–51. DOI: [10.1016/j.fusengdes.2015.10.002](https://doi.org/10.1016/j.fusengdes.2015.10.002) (cit. on p. 36).
- [42] C. Theiler. «Basic Investigation of Turbulent Structures and Blobs of Relevance for Magnetic Fusion Plasmas». Ph.D. dissertation. Dec. 2011. DOI: [10.5075/epfl-thesis-5228](https://doi.org/10.5075/epfl-thesis-5228) (cit. on p. 41).
- [43] R. J. Goldston. «Heuristic Drift-Based Model of the Power Scrape-off Width in Low-Gas-Puff H-Mode Tokamaks». In: 52.1 (Dec. 2011), p. 013009. DOI: [10.1088/0029-5515/52/1/013009](https://doi.org/10.1088/0029-5515/52/1/013009) (cit. on p. 43).
- [44] T. Eich et al. «Scaling of the Tokamak near the Scrape-off Layer H-Mode Power Width and Implications for ITER». In: *Nuclear Fusion* 53.9 (Aug. 2013), p. 093031. DOI: [10.1088/0029-5515/53/9/093031](https://doi.org/10.1088/0029-5515/53/9/093031) (cit. on p. 43).
- [45] D. Maisonnier et al. «Power Plant Conceptual Studies in Europe». In: *Nuclear Fusion* 47.11 (Oct. 2007), pp. 1524–1532. DOI: [10.1088/0029-5515/47/11/014](https://doi.org/10.1088/0029-5515/47/11/014) (cit. on p. 43).
- [46] H. Tran et al. «Qualification of the forebody heatshield of the Stardust’s Sample Return Capsule». In: *32nd Thermophysics Conference*. DOI: [10.2514/6.1997-2482](https://doi.org/10.2514/6.1997-2482) (cit. on p. 43).

- [47] H. J. N. van Eck et al. «A Differentially Pumped Argon Plasma in the Linear Plasma Generator Magnum-PSI: Gas Flow and Dynamics of the Ionized Fraction». In: *Plasma sources science & technology* 20.4 (2011), p. 045016. DOI: [10.1088/0963-0252/20/4/045016](https://doi.org/10.1088/0963-0252/20/4/045016) (cit. on p. 44).
- [48] DIFFER website. <https://www.differ.nl/research/fusion-facilities-and-instrumentation/magnum-psi> (cit. on p. 44).
- [49] G. G. van Eden et al. «Oscillatory Vapour Shielding of Liquid Metal Walls in Nuclear Fusion Devices». en. In: *Nature Communications* 8.1 (Dec. 2017), p. 192. DOI: [10.1038/s41467-017-00288-y](https://doi.org/10.1038/s41467-017-00288-y) (cit. on pp. 45, 48, 50–52, 69, 101).
- [50] M. R. Gilbert et al. «Comparative Assessment of Material Performance in DEMO Fusion Reactors». In: *Fusion Science and Technology* 66.1 (Aug. 2014), pp. 9–17. DOI: [10.13182/FST13-751](https://doi.org/10.13182/FST13-751) (cit. on p. 46).
- [51] G. Pintsuk. «Tungsten as a Plasma-Facing Material». In: *Comprehensive Nuclear Materials* 4 (Dec. 2012), pp. 551–581. DOI: [10.1016/B978-0-08-056033-5.00118-X](https://doi.org/10.1016/B978-0-08-056033-5.00118-X) (cit. on p. 46).
- [52] T. W. Morgan et al. «Power Handling of a Liquid-Metal Based CPS Structure under High Steady-State Heat and Particle Fluxes». In: *Proceedings of the 22nd International Conference on Plasma Surface Interactions 2016, 22nd PSI 12* (Aug. 2017), pp. 210–215. DOI: [10.1016/j.nme.2017.01.017](https://doi.org/10.1016/j.nme.2017.01.017) (cit. on p. 47).
- [53] T. W. Morgan et al. «Liquid Metals as a Divertor Plasma-Facing Material Explored Using the Pilot-PSI and Magnum-PSI Linear Devices». In: *Plasma Physics and Controlled Fusion* 60.1 (Oct. 2017), p. 014025. DOI: [10.1088/1361-6587/aa86cd](https://doi.org/10.1088/1361-6587/aa86cd) (cit. on pp. 48, 52, 54, 58, 59).
- [54] G. G. van Eden et al. «Self-Regulated Plasma Heat Flux Mitigation Due to Liquid Sn Vapor Shielding». en. In: *Physical Review Letters* 116.13 (Apr. 2016), p. 135002. DOI: [10.1103/PhysRevLett.116.135002](https://doi.org/10.1103/PhysRevLett.116.135002) (cit. on pp. 48–50, 54).
- [55] M. A. Abdou et al. «On the Exploration of Innovative Concepts for Fusion Chamber Technology». In: *Fusion Engineering and Design* 54.2 (Feb. 2001), pp. 181–247. DOI: [10.1016/S0920-3796\(00\)00433-6](https://doi.org/10.1016/S0920-3796(00)00433-6) (cit. on p. 52).
- [56] M. Iafrati. «Phenomenology of Plasma-Wall Interaction Using Liquid Metals in Tokamak Devices». Ph.D. dissertation. Università degli Studi di Padova, 2019. URL: <http://paduaresearch.cab.unipd.it/11904/> (cit. on p. 52).

- [57] J. W. Coenen et al. «Liquid Metals as Alternative Solution for the Power Exhaust of Future Fusion Devices: Status and Perspective». In: *Physica Scripta* T159 (Apr. 2014), p. 014037. DOI: [10.1088/0031-8949/2014/t159/014037](https://doi.org/10.1088/0031-8949/2014/t159/014037) (cit. on p. 52).
- [58] F. J. Smith et al. «The Solubility and Isotopic Exchange Equilibrium for Hydrogen Isotopes in Lithium». In: *Journal of Inorganic and Nuclear Chemistry* 41.7 (Jan. 1979), pp. 1001–1009. DOI: [10.1016/0022-1902\(79\)80077-9](https://doi.org/10.1016/0022-1902(79)80077-9) (cit. on p. 54).
- [59] A Cremona et al. «Deuterium Retention and Erosion in Liquid Sn Samples Exposed to D2 and Ar Plasmas in GyM Device». In: *Nuclear Materials and Energy* 17 (Dec. 2018), pp. 253–258. DOI: [10.1016/j.nme.2018.11.010](https://doi.org/10.1016/j.nme.2018.11.010) (cit. on p. 54).
- [60] J. P. S. Loureiro et al. «Deuterium Retention in Tin (Sn) and Lithium–Tin (Li–Sn) Samples Exposed to ISTTOK Plasmas». In: *Proceedings of the 22nd International Conference on Plasma Surface Interactions 2016, 22nd PSI 12* (Aug. 2017), pp. 709–713. DOI: [10.1016/j.nme.2016.12.026](https://doi.org/10.1016/j.nme.2016.12.026) (cit. on p. 54).
- [61] W. Ou et al. «Deuterium Retention in Sn-Filled Samples Exposed to Fusion-Relevant Flux Plasmas». In: 60.2 (Jan. 2020), p. 026008. DOI: [10.1088/1741-4326/ab5cd4](https://doi.org/10.1088/1741-4326/ab5cd4) (cit. on p. 54).
- [62] A. Manhard. «Deuterium Retention in Solid and Liquid Tin after Low-Temperature Plasma Exposure». In: 60.10 (Aug. 2020), p. 106007. DOI: [10.1088/1741-4326/aba801](https://doi.org/10.1088/1741-4326/aba801) (cit. on p. 54).
- [63] S. Roccella et al. «CPS Based Liquid Metal Divertor Target for EU-DEMO». In: *Journal of Fusion Energy* 39.6 (Dec. 2020), pp. 462–468. DOI: [10.1007/s10894-020-00263-4](https://doi.org/10.1007/s10894-020-00263-4) (cit. on p. 54).
- [64] Y. Nagayama. «Liquid Lithium Divertor System for Fusion Reactor». In: *Proceeding of the 25th Symposium on Fusion Technology* 84.7 (June 2009), pp. 1380–1383. DOI: [10.1016/j.fusengdes.2009.02.002](https://doi.org/10.1016/j.fusengdes.2009.02.002) (cit. on p. 56).
- [65] P. Rindt et al. «Power handling and vapor shielding of pre-filled lithium divertor targets in Magnum-PSI». In: *Nuclear Fusion* 59.5 (Mar. 2019). DOI: [10.1088/1741-4326/ab0560](https://doi.org/10.1088/1741-4326/ab0560) (cit. on p. 57).
- [66] V. A. Evtikhin et al. «Energy Removal and MHD Performance of Lithium Capillary-Pore Systems for Divertor Target Application». In: *Fusion engineering and design* 49 (2000), pp. 195–199. DOI: [10.1016/S0920-3796\(00\)00423-3](https://doi.org/10.1016/S0920-3796(00)00423-3) (cit. on p. 56).

- [67] I. Vertkov et al. at IAEA 28th FEC. *The concept of lithium based plasma facing elements for steady state fusion tokamak-reactor and its experimental validation*. [https://nucleus.iaea.org/sites/fusionportal/SharedDocuments/FEC2018/FEC2018\\_ConfMat\\_Online.pdf](https://nucleus.iaea.org/sites/fusionportal/SharedDocuments/FEC2018/FEC2018_ConfMat_Online.pdf). 2018 (cit. on p. 57).
- [68] R. J. Goldston et al. «The Lithium Vapor Box Divertor». In: *Physica Scripta* T167 (Jan. 2016), p. 014017. DOI: [10.1088/0031-8949/t167/1/014017](https://doi.org/10.1088/0031-8949/t167/1/014017) (cit. on p. 57).
- [69] R. J. Goldston et al. «Recent Advances towards a Lithium Vapor Box Divertor». In: *Proceedings of the 22nd International Conference on Plasma Surface Interactions 2016, 22nd PSI* 12 (Aug. 2017), pp. 1118–1121. DOI: [10.1016/j.nme.2017.03.020](https://doi.org/10.1016/j.nme.2017.03.020) (cit. on pp. 57, 58).
- [70] C. E. Kessel et al. at IAEA DEMO Workshop in Korea (Daejeon). *Exploring Liquid Metal Plasma Facing Components*. <https://nucleus.iaea.org/sites/fusionportal/SharedDocuments/DEMO/2018/3/Kessel.pdf>. 2018 (cit. on p. 58).
- [71] E. Tonello et al. «A Point Plasma Model for Linear Plasma Devices Based on SOLPS-ITER Equations: Application to Helium Plasma». In: *Nuclear fusion* 61.6 (2021), p. 66036. DOI: [10.1088/1741-4326/abfbb3](https://doi.org/10.1088/1741-4326/abfbb3) (cit. on pp. 61–67, 69, 72, 76, 80, 101, 102).
- [72] B. J. Braams. «Radiative Divertor Modelling for ITER and TPX». In: *Contributions to Plasma Physics* 36.2-3 (Jan. 1996), pp. 276–281. DOI: [10.1002/ctpp.2150360233](https://doi.org/10.1002/ctpp.2150360233) (cit. on p. 62).
- [73] B. D. Dudson. «BOUT++: A Framework for Parallel Plasma Fluid Simulations». In: *Computer Physics Communications* 180.9 (Sept. 2009), pp. 1467–1480. DOI: [10.1016/j.cpc.2009.03.008](https://doi.org/10.1016/j.cpc.2009.03.008) (cit. on p. 62).
- [74] P. Ricci. «Simulation of Plasma Turbulence in Scrape-off Layer Conditions: The GBS Code, Simulation Results and Code Validation». In: *Plasma Physics and Controlled Fusion* 54.12 (Nov. 2012), p. 124047. DOI: [10.1088/0741-3335/54/12/124047](https://doi.org/10.1088/0741-3335/54/12/124047) (cit. on p. 62).
- [75] A. H. Hakim. «Continuum Electromagnetic Gyrokinetic Simulations of Turbulence in the Tokamak Scrape-off Layer and Laboratory Devices». In: *Physics of Plasmas* 27.4 (Apr. 2020), p. 042304. DOI: [10.1063/1.5141157](https://doi.org/10.1063/1.5141157) (cit. on p. 62).
- [76] P. Tamain. «The TOKAM3X Code for Edge Turbulence Fluid Simulations of Tokamak Plasmas in Versatile Magnetic Geometries». In: *Journal of Computational Physics* 321 (Sept. 2016), pp. 606–623. DOI: [10.1016/j.jcp.2016.05.038](https://doi.org/10.1016/j.jcp.2016.05.038) (cit. on p. 62).

- [77] H. Bufferand et al. «Numerical Modelling for Divertor Design of the WEST Device with a Focus on Plasma–Wall Interactions». In: 55.5 (2015), p. 053025. DOI: [10.1088/0029-5515/55/5/053025](https://doi.org/10.1088/0029-5515/55/5/053025) (cit. on p. 62).
- [78] S. Wiesen et al. «The New SOLPS-ITER Code Package». In: *Journal of Nuclear Materials* 463 (Aug. 2015), pp. 480–484. DOI: [10.1016/j.jnucmat.2014.10.012](https://doi.org/10.1016/j.jnucmat.2014.10.012) (cit. on p. 62).
- [79] X. Bonnin et al. «Presentation of the New SOLPS-ITER Code Package for Tokamak Plasma Edge Modelling». In: *Plasma and Fusion Research* 11 (2016). DOI: [10.1585/pfr.11.1403102](https://doi.org/10.1585/pfr.11.1403102) (cit. on p. 62).
- [80] *Istituto per la Scienza e Tecnologia dei Plasmi* website. URL: <https://www.istp.cnr.it> (cit. on p. 63).
- [81] A. S. Richardson. *2019 NRL Plasma Formulary*. <https://nucleus.iaea.org/sites/fusionportal/SharedDocuments/DEMO/2018/3/Kessel.pdf> (cit. on pp. 67, 71).
- [82] L. L. Alves. «The IST-LISBON Database on LXCat». In: *Journal of physics. Conference series* 565.1 (2014), pp. 12007–. DOI: [10.1088/1742-6596/565/1/012007](https://doi.org/10.1088/1742-6596/565/1/012007) (cit. on p. 67).
- [83] *EIRENE* website. <http://www.eirene.de> (cit. on p. 67).
- [84] D. R. Lide (Editor-in-Chief). *CRC Handbook of Chemistry and Physics, 87th Ed.* American Chemical Society, Jan. 2007. ISBN: 0-8493-0487-3. DOI: [10.1021/ja069813z](https://doi.org/10.1021/ja069813z) (cit. on p. 70).
- [85] I. Bray et al. «Calculation of Electron–Lithium Scattering Using the Coupled-Channel Optical Method». In: *Physical Review A* 47.2 (Feb. 1993), pp. 1101–1110. DOI: [10.1103/physreva.47.1101](https://doi.org/10.1103/physreva.47.1101) (cit. on p. 71).
- [86] E. D. Marenkov and A. A. Pshenov. «Vapor Shielding of Liquid Lithium Divertor Target during Steady State and Transient Events». In: *Nuclear Fusion* 60.2 (Feb. 2020), p. 026011. DOI: [10.1088/1741-4326/ab5eb5](https://doi.org/10.1088/1741-4326/ab5eb5) (cit. on pp. 89, 93, 97).
- [87] E. D. Marenkov et al. «Shielding of Liquid Metal Targets in Plasma of Linear Devices». In: *Physics of Plasmas* 27.6 (June 2020), p. 062514. DOI: [10.1063/5.0006509](https://doi.org/10.1063/5.0006509) (cit. on p. 90).
- [88] D. Lee et al. «Exact Solution for the Generalized Bohm Criterion in a Two-Ion-Species Plasma». In: *Physical Review Letters* 99.15 (Oct. 2007), p. 155004. DOI: [10.1103/PhysRevLett.99.155004](https://doi.org/10.1103/PhysRevLett.99.155004) (cit. on p. 92).